Study on Charge Trapping and Recombination of Small Molecule Organic Solar Cells

Xia Hao

June 2015

Study on Charge Trapping and Recombination of Small Molecule Organic Solar Cells

Xia Hao

Doctoral Program in *Applied Physics*

Submitted to the Graduate School of

Pure and Applied Sciences

in Partial Fulfillment of the Requirements

for the Degree of Doctor of Philosophy in

Engineering

at the

University of Tsukuba

Abstract

In a world of limited energy resources, organic solar cells (OSCs) are raising increasing attention and the power conversion efficiency of OSCs has increased from around 1% to over 11% in the past 3 decades. These improvements have been driven mainly by optimization in materials synthesis and device engineering. In spite of the great success in device efficiency, many fundamental issues concerning basic operational mechanisms of OSCs remain unknown or under debate, limiting further improvement of the device performance.

One of the most important properties of organic semiconductor is the structural disorder in nature, which leads to ubiquity of impurities in organic materials. These defects will act as traps or carrier scattering centers even if they do not trap carriers. The presence and distribution of carrier trapping sites will dominate the charge carriers transportation and extraction in OSCs either by charge trapping or trap mediated recombination. However, the investigation on charge trapping and recombination is still lacked to date.

This dissertation is aimed at clarifying the effect of charge trapping and recombination on OSCs by combining the traditional steady-state characteristics with the transient measurements (transient photovoltage and transient photocurrent). The correlation between device configuration and the actual performance was studied in three device structures.

The ITO cathode/C_{60} interface is of great importance in inverted planar devices because the power conversion efficiency is significantly improved by inserting an appropriate buffer of BCP. For BCP buffers, in spite of the effect of blocking excitons, it is also demonstrated in this work that the insertion of BCP buffer prohibited the charge trapping and suppressed the recombination of the carriers.

Constructing an inverted device with identical layers as that of the conventional one makes it possible to investigate the degradation mechanism of OSCs. This eliminates the interfacial and morphological changes induced by different buffers utilization. The energy loss in conventional device during the degradation process was originated from the fullerene-deterioration induced trap states. These trap states involved in the charge trapping, aggravated trap-mediated recombination and as a result, speeded up the degradation of conventional devices.

The greatly improved short circuit current is the main cause of the enhancement of the power conversion efficiency in conventional bulk device based on small molecules as compared with the bilayer one. While the attempt of extending the technology to the inverted device failed due to the sharply decreased open circuit voltage. The morphology of co-evaporated active layer in inverted device shows an extensive phase segregation while that of conventional device is interpenetrated with moderate phase segregation. Aggravated recombination was observed in the former case. It suggests that in small molecule bulk devices with identical layers, the open circuit voltage is largely determined by the morphology of the active layer which directly related to the charge recombination process.

This work clarifies the effects of charge trapping and recombination in small molecule based planar and bulk organic solar cells. Charge trapping in planar devices tends to be involved in the recombination and deteriorate the device performance. In contrast, for bulk devices, charge trapping is a more general phenomenon while the device performance shows a closer association with the morphological properties of active layer as compared with the charge trapping effects.

Tables of contents

Chapter 1 Introduction

Organic solar cells (OSCs) are important components of photovoltaic devices which convert the sun light into electricity directly. In a world of limited energy supply, due to the incomparable superiorities of flexibility, light weight and also transparency, the OSCs receive more and more attention and the best researched device has achieved a power conversion efficiency of 12%.[1-1] Fig. 1-1 shows some application examples of OSCs and also the image of the "hero" cell from Heliatek. In spite of the advantages mentioned above, the OSC could also be fabricated by quite simple procedures, among which the spin coating is the representative technology. Ease of fabrication, and also the high absorption coefficient of the organic absorbers, makes it possible to fabricate OSCs at a fairly low cost.

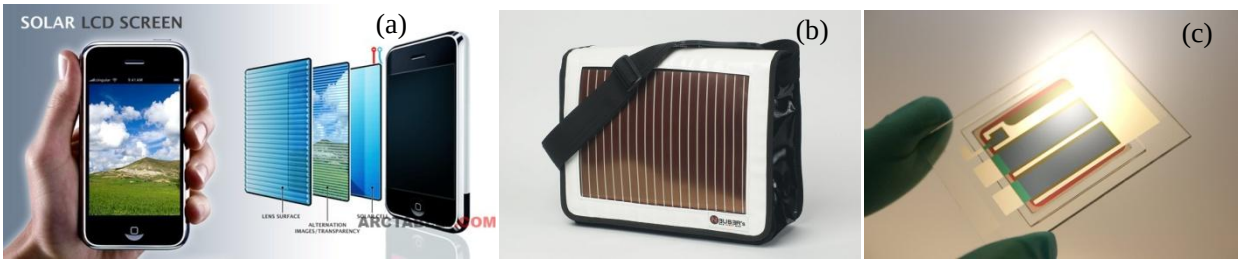

Fig. 1-1. (a) An organic solar LCD screen named Wysips@ Crystal, from Sun Partner Technologies. (b) Sun bag, designed and fabricated by Konarka Technologies. (c) OSC with world record efficiency of 12% from Heliatek.

The rapid development of OSCs is mainly relying on the discovery of conducting organic materials and optimization of synthesis technology of organic semiconductors. An organic semiconductor is a kind of organic material that with an electrical conductivity between that of insulators and that of metals. The process of energy and charge transport in an organic semiconductor is totally different from that in the traditional inorganic semiconductors. This process is directly related to the performance of organic photovoltaic devices, while there are still many problems, especially fundamental ones, have to be settled urgently and this thesis is focused on the aspect of charge trapping and recombination in OSCs.

In this chapter, the research background and a brief overview of organic semiconductors as well as organic photovoltaic devices are introduced.

1.1 World population and energy supply

1.1.1 The rapid growth of human population

The world population was estimated to be approximately 7.2 billion in 2013. During the past 300 years, the human population has grown about ten-fold and almost one fold in the last century.[1-2] As shown in Fig. 1-2, the fast increase in human population started from around 200 years ago, that is, with the advent of the industrial revolution. Although it is reported that the world population will come to the end of growth at around the end of this century,[1-3] the huge population quota brought about great impacts on the earth. We human societies are dependent on complex, interrelated physical chemical and biological processes, such as the energy produced by the sun, the circulation of the elements crucial for life, the factors regulating the climatic change and so on,[1-4] among which, the energy supply is the basis of the continuously and

sustainable development of the human society.

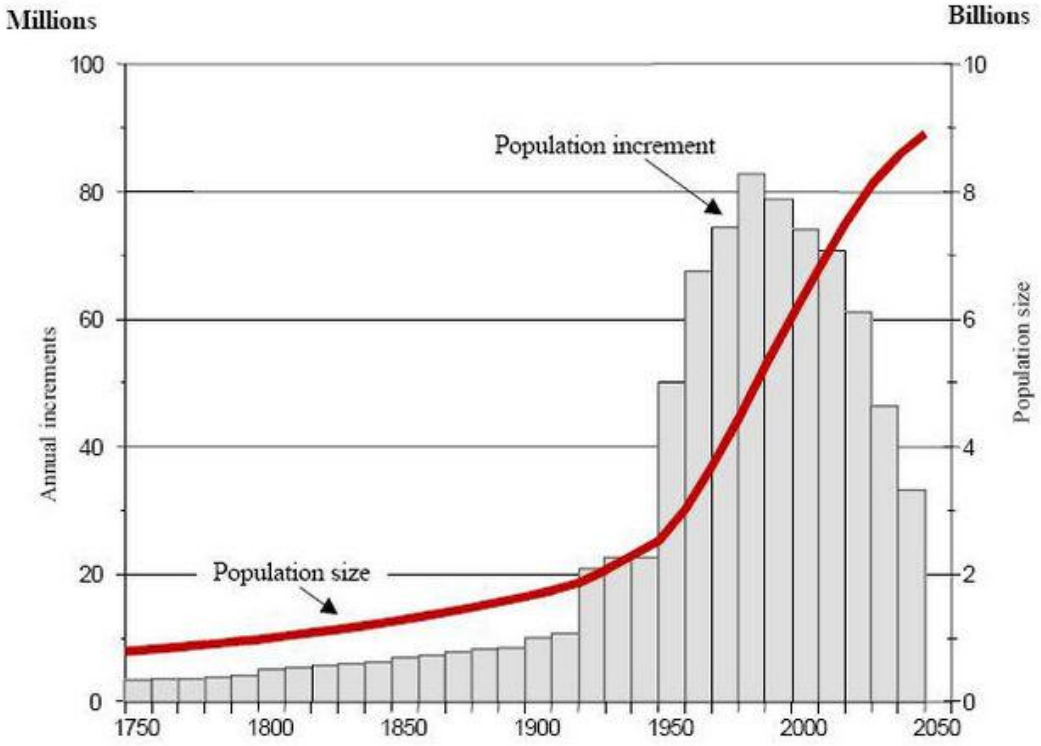

Fig. 1-2. World population growth, reprinted from *Ref.* [1-2].

1.1.2 Energy supply

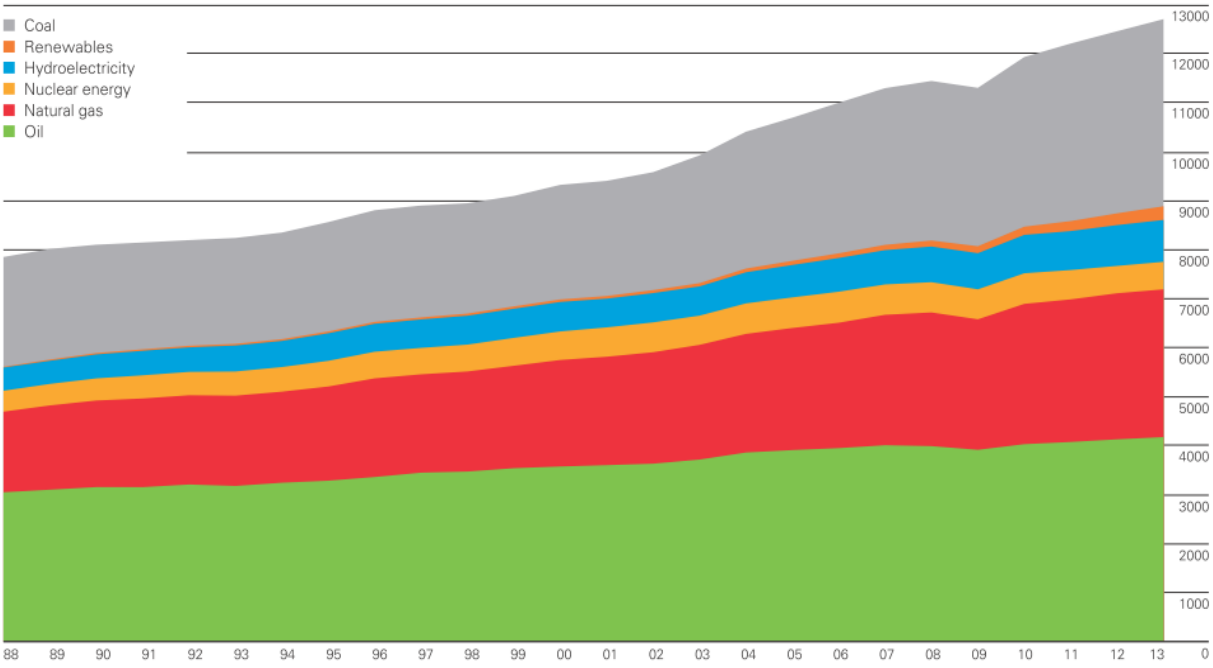

Fig. 1-3. World primary energy consumption from 1988 to 2013 (Mtoe[1]), reprinted from *Ref.*[1-5].

[1] Mtoe stands for million tonnes oil equivalent.

Energy is a crucial component for sustaining the diverse processes of nature. With the rapid increase of the human population as well as the astonishing development of the industry, the energy consumption keeps increasing, especially in the last three decades. Fig. 1-3 displays the world primary energy consumption at the time range of 1988 to 2013. Compared with the traditional fuel energies, the increase in the share of renewable energies is extremely slow. It is urgent and significant to further develop the clean and renewable energies. For one thing, the traditional fossil fuels are exhausting and for another, the consequences of fossil fuels burning such as air pollution and emission of green house gases are endangering people's lives.

1.2 Renewable energies

As aforementioned, our life is now powered mostly by the burning of non-renewable fossil fuels such as coal, oil and natural gas. And to date, the most commercially applied renewable energy is nuclear energy.[1-6] However, there are potential crisis of nuclear power stations and the disposal of the nuclear waste is a process of complexity.

As other alternatives, we can generate energy from photovoltaic, solar thermal, wind, geothermal and so on, without taking risks of nuclear irradiation and leak. Fig. 1-4 shows an overview on the renewable energy share in 2012. From the figure we can tell that in the year of 2012, the renewable energy occupied 19% of the total energy consumption, among which, the share of wind, solar, biomass and geothermal power is merely 1.2%. The renewable energy is a quite potential energy source and the further exploration is urgent needed. Compared with other renewable energy generation systems, solar cell has superiorities of directly converting sun light into electricity without heavy machinery and noise. Therefore, the maintenance of the solar cell is simple enough for the residential application.

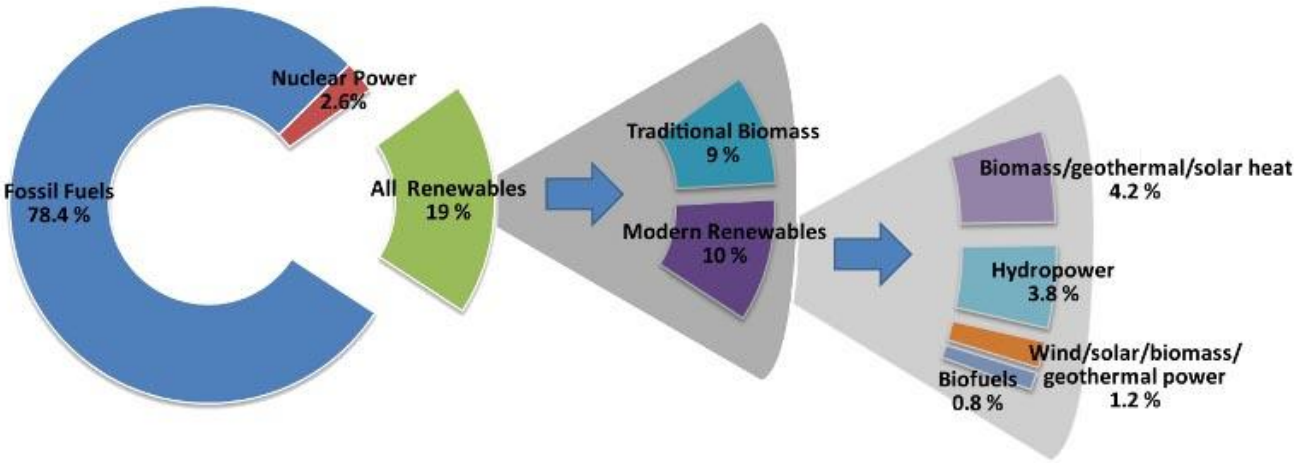

Fig. 1-4. World renewable energy consumption in 2012, reprinted from *Ref*.[1-7].

1.3 Photovoltaic solar technology

Many photovoltaic technologies exist with varying degrees of development, *i.e.* Si based bulk solar cells, representative thin film solar cells based on cadmium telluride (CdTe), copper indium gallium diselenide (CIGS) and so on. In order to generate cost-effective solar energy, either the efficiency of the solar cells should be improved or the fabrication cost must be lowered. Hence continuous research has been carried out in this direction and has led to four generations of photovoltaic technologies.

1.3.1 Silicon wafer based first generation photovoltaics

The first generation photovoltaic solar cells are the dominant technology in the commercial production of solar cells and account for nearly 80% of the solar cell market. They are typically fabricated by using a crystalline silicon (c-Si) wafer, in which a semiconductor junction is formed by doping phosphorus into the top surface of the silicon wafer. Screen-printed contacts are applied to the front and bottom of the cell. The typical efficiency of such silicon-based commercial photovoltaic energy system is in the order of 15%. In these cells, an efficiency up to 33% can be achieved theoretically, but the best researched cells in the laboratory only have a power conversion efficiency of around 25%. The main advantages of these solar cells are broad spectral absorption range, high carrier mobility and high efficiency. Nevertheless, the starting materials used to prepare c-Si must be refined to a purity of >99.9999%. This laborious, energy intensive process makes manufacturing plant capital cost is as high as 60% of manufacturing cost. However, the main disadvantages are, they require expensive manufacturing technologies. And the higher energy photons is wasted as heat, besides, the absorbance of light for the silicon is poor. The cost of generating electricity using silicon solar modules is typically almost 10 times higher than that from traditional fossil fuel so that their widespread application was greatly inhibited.

1.3.2 Thin film based second generation photovoltaics

Second generation solar cells are a kind of solar cells that were composed of thin-film semiconductors. This generation basically based on three types of materials: amorphous silicon (a-Si), CdTe and CIGS. These technologies are typically fabricated by depositing a thin layer of photo-active material onto the glass or a flexible substrate. The driving force of the rapid development of thin film solar cells is their potential for the reduction of manufacturing costs. Besides, these semiconductors have direct gap which leads to higher absorption coefficient. Therefore, less than 1 μm thin film is thick enough to absorb complete solar radiation, which is a 100~1000 times less than that of c-Si based solar cells.

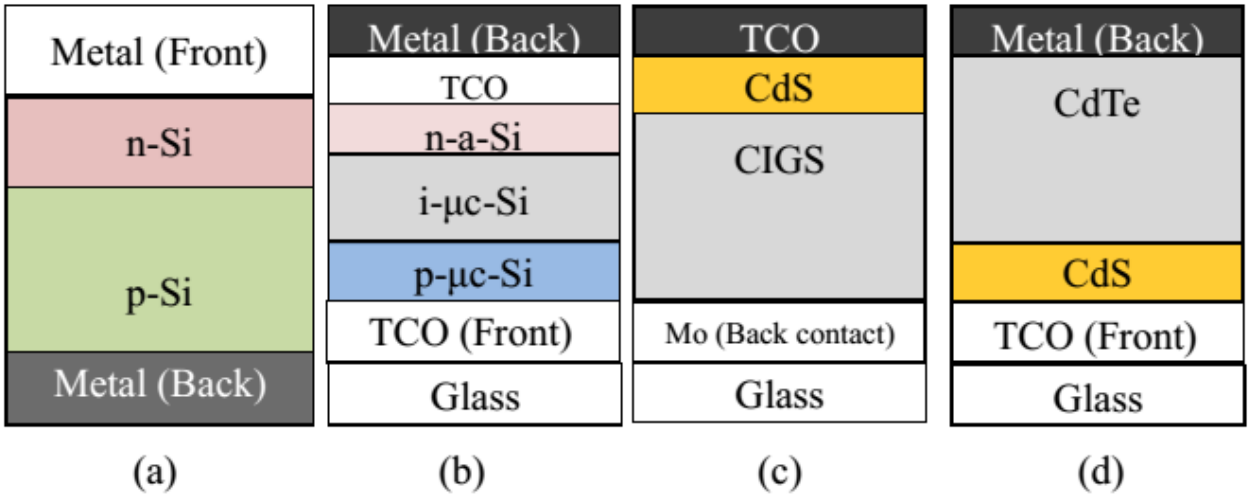

Fig. 1-5. The structures of second generation solar cells: (a) for c-Si, (b) for a-Si, (c) CIGS and (d) CdTe. TCO stands for transparent conductive oxide and Mo is molybdenum.

Amorphous silicon solar cell structure has a single sequence of p-i-n layers, as shown in Fig. 1-5(b). The a-Si devices utilize a stacked three-layer structure with stabilized efficiencies of 10.1%. However, the a-Si solar cells suffer from the degradation in the power output when exposed to light. Thinner layers can be

used to increase the electric field strength across the material as well as the power conversion efficiency. In case of CIGS solar cell, copper indium diselenide (CIS) is modified by adding gallium, and it exhibits the record laboratory efficiency of 20.5%. CIGS solar cell showed highest efficiency among the second generation thin film solar cells. When recently, CdTe has achieved a laboratory efficiency of 21%, the new record of thin film solar cells.[1-8] CdTe has a nearly optimal band gap and can be easily deposited with thin film techniques. This updated CdTe solar cell was deposited on cadmium sulfide (CdS) to form a p-n junction photovoltaic solar cell (Fig. 1-5(d)).

Although the thin film solar cells absorb incident radiation more efficiently compared to single crystalline silicon, the power conversion efficiencies of these devices are among 15-21%, which is less than that of the crystalline silicon ones (25.6%). The promise of the low cost power has not been realized yet by these technologies.

1.3.3 Third generation solar cells

Third generation technologies aim to enhance poor electrical performance of second generation thin film solar cells while maintaining low product costs. The third generation approaches now under investigation include nano-crystal solar cells,[1-9] photochemical cells (PEC), dye-sensitized hybride solar cells (DSSC),[1-10] tandem cells,[1-11] organic solar cells[1-12] and the cells based on the materials that generate multiple electron-hole pairs. Currently, most of the work on third generation solar cells is accomplished in laboratory and being developed by new companies and most part of it is still not commercially available.

1.3.4 Latest progress in photovoltaic cells

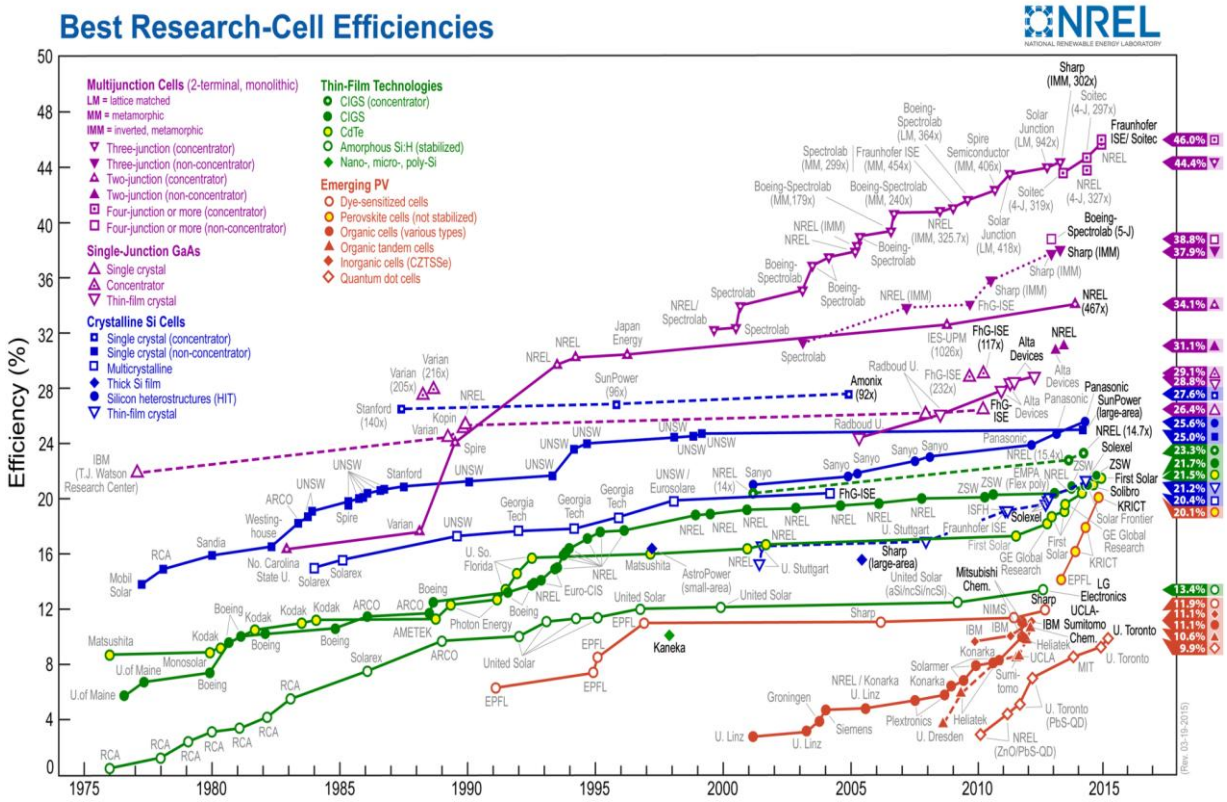

Fig. 1-6. Efficiency evolution of best research cells by technology type, reprinted from *Ref.* [1-13].

Fig. 1-6 and Table 1-1 summarize the best measurement for solar cells and submodules. Compared with the earlier version of the solar cell efficiency tables,[1-14~1-16] tremendous progress has been made over recent years in improving the power conversion efficiency, *i.e.* the CdTe solar cells have scaled the highest efficiency among the thin film devices of ~1 cm^2 size. The steady improvement in efficiencies of some other solar cells, *i.e.* crystalline and amorphous silicon cells, dye-sensitized thin-film minimodule and so on is also witnessed.

In the case of organic solar cells, the record efficiency was kept by Toshiba, who fabricated an organic solar cell with a confirmed power conversion efficiency of around 11%.[1-8] With demonstrated power conversion efficiency of 11%, the organic solar cells representa viable rout to realizing large area flexible plastic photovoltaic technology.

Table 1-1. Confirmed terrestrial cell and submodule efficiencies measured under AM 1.5 spectrum at 25 ℃.[1-8]

Classification	Efficiency (%)	Area (cm^2)	Voc (V)	Jsc (mA/cm^2)	Fill factor (%)	Test center
Si (crystalline)	25.6 ± 0.5	143.7 (da)	0.740	41.8	82.7	AIST
Si (multicrystalline)	20.8 ± 0.6	243.9 (ap)	0.6626	39.03	80.3	FhG-ISE
Si (thin film transfer)	21.2 ± 0.4	239.7 (ap)	0.687	38.50	80.3	NREL
Si(thin film minimodule)	10.5 ± 0.3	94.0 (ap)	0.492	29.7	72.1	FhG-ISE
GaAs (thin film)	28.8 ± 0.9	0.9927 (ap)	1.122	29.68	86.5	NREL
GaAs (multicrystalline)	18.4 ± 0.5	4.011 (t)	0.994	23.2	79.7	NREL
InP (crystalline)	22.1 ± 0.7	4.02 (t)	0.878	29.5	85.4	NREL
CIGS (cell)	20.5± 0.6	0.9882 (ap)	0.752	35.3	77.2	NREL
CIGS (minimodule)	18.7± 0.6	15.892 (da)	0.701	35.29	75.6	FhG-ISE
CdTe (cell)	21.0± 0.4	1.0623 (ap)	0.8759	30.25	79.4	Newport
Si (amorphous)	10.2± 0.3	1.001 (ap)	0.896	16.36	69.8	AIST
Si (microcrystalline)	11.4± 0.3	1.046 (da)	0.535	29.07	73.1	AIST
Dye sensitized	11.9± 0.4	1.005 (da)	0.744	22.47	71.2	AIST
Dye (minimodule)	10.0± 0.4	24.19 (ap)	0.718	20.46	67.7	AIST
Dye (submodule)	8.8± 0.3	398.8 (da)	0.697	18.42	68.7	AIST
Organic thin film	11.0± 0.3	0.993 (da)	0.793	19.40	71.4	AIST
Organic (minimodule)	9.5± 0.3	25.05 (da))	0.794	17.06	67.5	AIST
InGaP/GaAs/InGaAs	37.9 ± 1.2	1.047 (ap)	3.065	14.27	86.7	AIST
a-Si/nc-Si/nc-Si(thin film)	13.4 ± 0.4	1.006 (ap)	1.863	9.52	71.9	NREL
a-Si/nc-Si (thin film cell)	12.3 ± 0.3%	0.962 (ap)	1.365	12.93	69.4	AIST
a-Si/nc-Si (thin film minimodule)	11.8 ± 0.6	40.26 (ap)	1.428	12.27	67.5	FhG-ISE

1.4 Organic semiconductors

The presence of organic molecular semiconductor in organic photovoltaic devices is the main distinction as compared with the traditional inorganic solar cells. The organic molecules will maintain most of their characteristics in the related devices: the optical and electrical properties of organic semiconductors,

i.e., the absorption, luminescence, charge separation and transportation *et al*.

1.4.1 A brief introduction of organic semiconductor

The organic materials can be simply classified into conjugated molecules and unconjugated ones. Conjugated is defined as double bonds with one single bond in between. Being conjugated is the precondition for the delocalization. Considering that the basic requirement for electrical conductivity is the presence of delocalized electrons, which can receive energy from an applied field. Only the solid materials composed of conjugated molecules are the object of the research on organic semiconductors. However, the capability of electron transportation motivated from delocalization is much less pronounced in an organic material than the process in that of the inorganic semiconductors.

When two carbon atoms with sp^2 orbitals form a bond to each other using their sp^2 orbitals, a σ bond is formed between them. Moreover, the extra p orbitals that exist above and below each carbon atom also overlap with each other. This leads to the formation of a second bond in addition to the σ bond formed between the sp^2 orbitals. This later bond, which does not occur directly between the nuclei on the inernuclear axis, but rather above and below the internuclear axis, is called a π bond. Fig. 1-7 shows the σ bond and π bond in ethane, as an example for the simplest conjugated π-electron system. The delocalization is given by the π-system of molecular orbitals by assembling the molecules from single atoms.

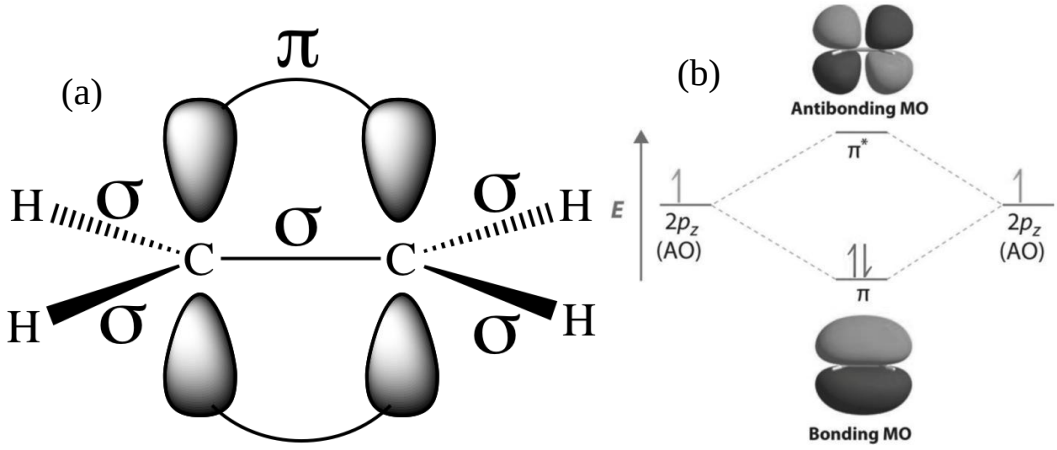

Fig. 1-7. (a) σ bond and π bond in ethane (C_2H_4) and (b) energy levels diagram of a bonding/antibonding pair of π-system.

In the process of assembling the single atoms into molecules, hybridization will occur. Take ethane as an example, as shown in Fig. 1-7. After hybridization, each carbon still has one unhybridized $2p_z$ orbital that is perpendicular to the hybridized lobes and contains a single electron. The two singly occupied $2p_z$ orbitals can overlap to form a π bonding and a π^* antibonding orbitals, which will produce an energy level diagram shown in Fig. 1-7(b). With the formation of a π bonding orbital, electron density increases in the plane between the carbon nuclei. The π^* orbital lies outside the internuclear region and has a nodal plane perpendicular to the internuclear axis. Because each $2p_z$ orbital has a single electron, there are only two electrons, enough to fill only the bonding level, leaving the antibonding orbital empty. As a result, the C-C bond in ethylene consisting of a σ bond and a π bond. [1-17]

The energy difference between the highest occupied molecular orbital (HOMO, π) and the lowest unoccupied molecular orbital (LUMO, π^*) of an organic molecule, is called E_g. Generally, the E_g of organic semiconductors lies in energy range of 1.5-3 eV, which can be tuned by modifying the chemical structure of the molecule, thereby allowing tuning of the optoelectronic properties.

In terms of molecular weight of the organic materials, they can be classified into polymers and small molecules. The small molecule is referred to small organic compound, approximately, with a molar mass less than around 1000 g/mol. The first organic solar cell fabricated by Tang, with a structure of active bilayers sandwiched between In_2O_3 and Ag, was based on small molecules: copper phthalocyanine (CuPc) and perylene tetracarboxylic derivative. [1-18]

In a traditional inorganic solar cell, current conduction occurs through the movement of free electrons and holes, generally known as charge carriers. The number of charge carriers will be greatly increased by doping effect. The so-called n-type and p-type refer to the type of dopant, and therefore the majority carrier. A semiconductor with majority of the free holes within it is p-type while that with mainly free electrons is n-type. Instead, in case of organic semiconductors, the charge transport typically follows a hopping mechanism and is governed by the class of transport models used to reproduce highly disordered system. It is believed that the organic molecules are ambipolar in nature. The "conductive type" is mainly determined by the relative ionization potential and electron affinity. For example, in a device based on CuPc and fullerene (C_{60}), the lower ionization potential and electron affinity of CuPc as compared with that of C_{60}, then in this system, CuPc can be regarded as donor (p-type) while C_{60} as acceptor (n-type). The chemical structures of common examples for donors and acceptors are listed in Fig. 1-8.

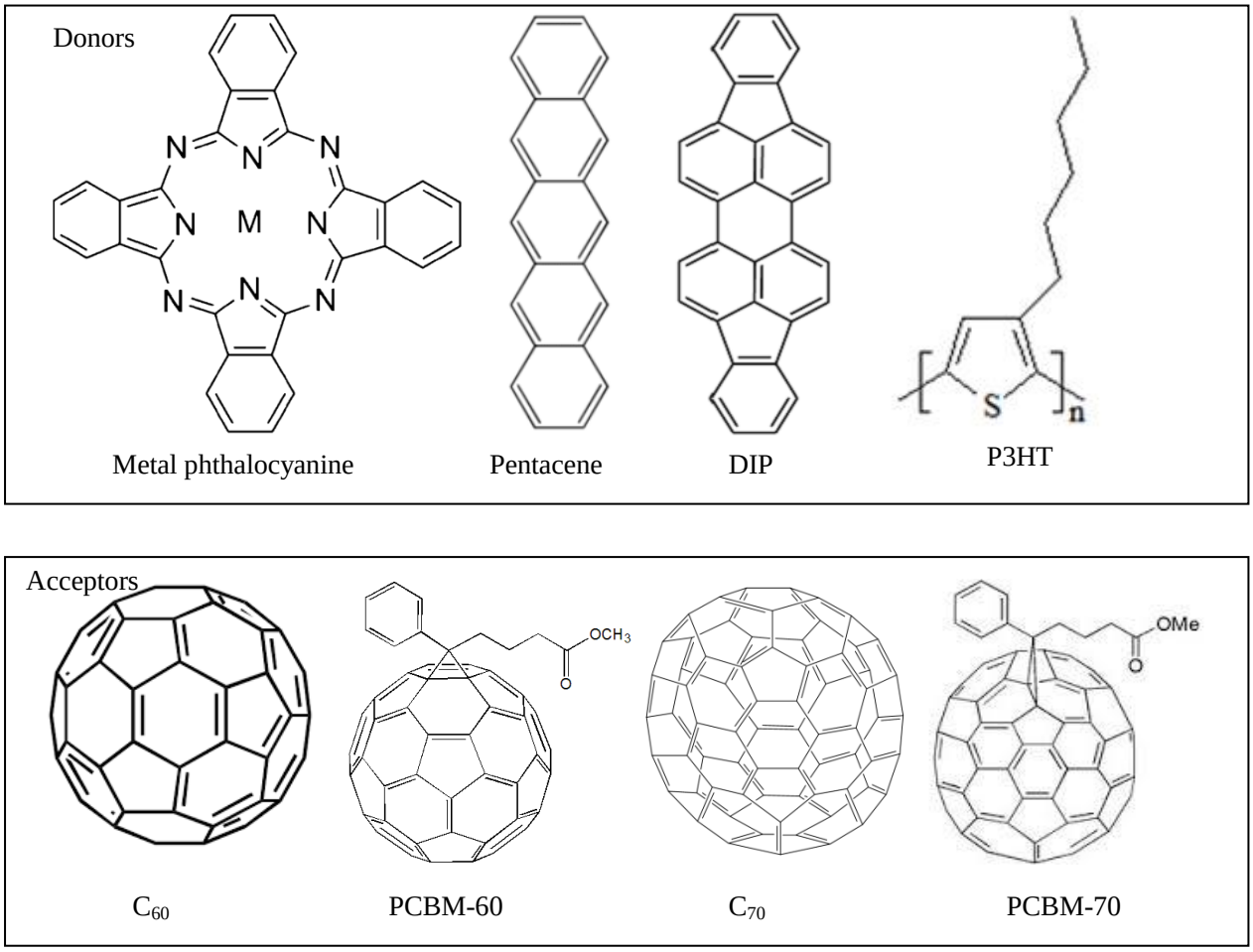

Fig. 1-8. Chemical structures of commonly used donor and acceptors (PCBM: phenyl-C_{61}-butyric acid methyl ester).

1.4.2 Carrier transport in organic semiconductors

In inorganic semiconductors, such as silicon or germanium, the strong coupling between the constitution atoms and long-range order lead to the delocalization of the electronic states. Therefore, the allowed valence and conduction bands, which are separated by a forbidden gap, will form. By thermal activation or photo-excitation, free carriers will be generated in the conduction band, leaving behind positively charged holes in the valence band. The transport of these free carriers is described in quantum mechanical terms by Bloch functions, wave vector-space and dispersion relations. The band transport is illustrated in Fig. 1-9(a).

On the contrary, in organic semiconductors, it is generally accepted that the carrier motion could be explained by the hopping model, due to the existence of structural or chemical defects. The hopping transport is a phonon-assisted tunneling mechanism from site to site, which is displayed in Fig. 1-9(b). Many hopping models are based on the Miller-Abrahams equation.[1-19~1-21] In this case, hopping from a localized site i to a state j takes place at frequency ν_0, corrected for a tunneling probability and the probability to absorb a phonon for hops upwards in energy:

$$\omega_{ij} = \nu_0 \begin{cases} exp\left(-2\alpha R_{ij} - \frac{E_{j-E_i}}{k_B T}\right): E_j - E_i \geq 0 \\ exp\left(-2\alpha R_{ij}\right): E_j - E_i \leq 0 \end{cases}. \quad (1\text{-}1)$$

Here, α is the inverse localization length; R_{ij} is the distance between the localized state; E_i is the energy at the state i; ν_0 is the frequency that the state attempt to escape.

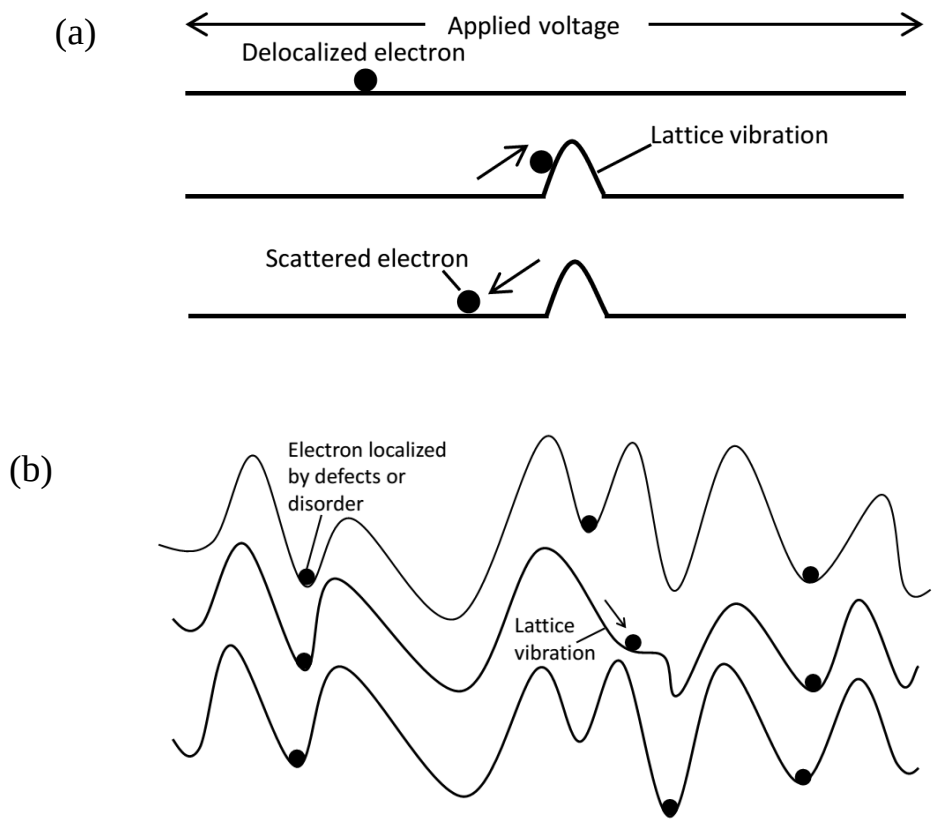

Fig. 1-9. Charge transport in inorganic and organic materials. (a) describes the band transport, which stands for an ideal crystal without defects, depicted as a straight line, in which free carriers are delocalized. There are always lattice vibrations that disrupt the symmetry of the crystal. (b) describes hopping transport. If a

carrier is localized by defects, disorder or it is self localized, the lattice vibrations will then determine the movement of a carrier from one site to another.[1-22]

Considering that the hopping probability depends on both the spatial and energetic difference between different hopping sites, the hopping process can be described in a four dimensional hopping space, which is composed of three spatial and one energy coordinate. In an organic semiconductor, covalent is the mainly interaction, while intermolecular interactions, due to van der Waals and London forces, are considerably weaker. In these organic semiconductors the HOMO and LUMO can be easily disrupted by disorder and they typically have narrow energy band. Thus, even in organic molecular crystals, the concepts of allowed transport sites are highly localized with a Gaussian distribution of energies.[1-22] The shape of the density of state (DOS) is suggested to be Gaussian based on the observed shape of the optical spectra.[1-23,1- 24]

To analyze the hopping transport in organic semiconductors, the transport energy[1-25] is an important concept. The transport energy is of significant importance because it stands for an energy that maximizes the probability for a carrier to hop upward in energy. It does not depend on the initial energy of the charged carrier, thus serving as a counterpart of the mobility edge.

For polycrystalline organic semiconductor layers, the temperature dependent transport data is often explained by a multiple trapping and release model.[1-26,1-27] In this model the organic semiconductor film consists of crystallites which are separated from each other by grain boundaries. In the composed crystallites the carriers are delocalized, while the charged carriers in the domain of grain boundaries become localized. The trapped carriers can be thermally activated to a transport level, which is very similar to hopping transport as above discussed.

1.5 Organic solar cells

1.5.1 The brief history of the development for organic solar cells

The first photocurrent was observed in anthracene by Kalman and Pope in 1959.[1-28] In the following two decades, several organic photovoltaic devices were reported. They consisted of a metal-organic junction which showed efficiencies of less than 0.1 %.[1-29] The first major breakthrough in the deployment of organic semiconductors in solar cells has been made by Ching W. Tang who published the donor-acceptor solar cell and reported an efficiency of 1%.[1-18] The second major step was the invention of the bulk heterojunction which is a mixed layer of donor and acceptor, fabricated by a co-deposition of the two molecules. This approach was firstly reported by Hiramoto, *et al.*[1-30~1-32]

After these achievements the amount of publications rose nearly exponentially in the last decade. Efficiencies recently reached 10%,[1-8] also pushed by several spin-offs and established companies turning focus on this topic. The reason for this boom can be found in the expected high potential of organic semiconductors.

1.5.2 Structures of organic solar cells

There are mainly three types of organic solar cells in terms of architectures. They are single layer device, bilayer device and bulk device. The first organic photovoltaic device fabricated in 1959[1-28] is single layered. This kind of device is simply using a single layer of organic semiconductor which was sandwiched between two electrodes with different work functions, as illustrated in Fig. 1-10(a). A low dielectric constant (typically 2-4) and the weak intermolecular coupling are the main characteristic for organic semiconductors. As a result, the problem with such kind of device is that the absorption of light in the organic layer results in

the production of a mobile excited state, namely, an exciton, rather than free electron-hole pairs that produced in the inorganic semiconductor. Here we also take anthracene as the example, which was utilized in Kalman and Pope's cell in 1959, the binding energy is as high as 1.5 eV,[1-33,1-34] which is greatly beyond the work function difference of the electrodes. The driving force to break up the excitons is therefore not sufficient and they diffuse within the organic material before reaching the electrodes. However, the problem is that the exciton diffusion length is ~10 nm in organic materials.[1-35~1-37] This is much shorter than the device thickness. Therefore, most of the photo generated excitons are recombined prior to be dissociated into electrons and holes. For this reason, the performance of single layer organic solar cell is not effective and the typical power conversion efficiency of is ~0.1%.

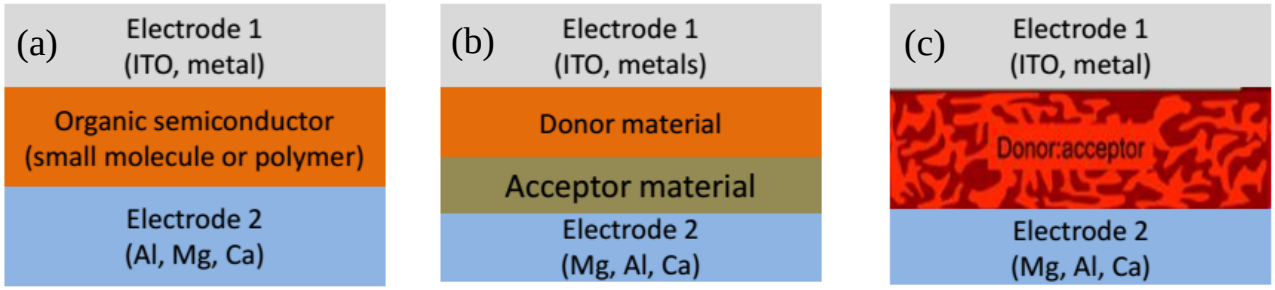

Fig. 1-10. Three main architectures of organic solar cells: (a) for the single layer device, (b) for the bilayer device and (c) for the bulk device.

Another category is bilayer device, which is composed of two organic materials with different affinities and ionization potentials (Fig. 1-10(b)). At the interface of these two materials, the contact potentials are strong and may favor excitons dissociation. The electrons will be accepted by the material with a larger electron affinity and the hole will be collected by the material with the lower ionization potential. In this device, the excitons also should be formed within the diffusion length. Otherwise the excitons will recombine and yield luminescence instead of contributing to photocurrent. Since the exciton diffusion length in the organic material is much shorter than the absorption depth of the film, the main limitation of bilayer device is the insufficient width of light absorbance layer.

The structure of another type: organic bulk device is shown in Fig. 1-10(c). The mixture of donor and acceptor is sandwiched between two electrodes. This configuration maximizes interfacial surface area to facilitate the exciton dissociation. If the interfacial length scale of the mixture is close to the exciton diffusion length, the exciton decay process will be dramatically reduced if every generated exciton reaches the interface, where fast dissociation takes place. Hence, the efficiency of charge generation was greatly improved by constructing enough interfaces of the active layer. As a result, a dramatic increase in the charge dissociation resulted in a higher short circuit current and open circuit voltage in bulk organic solar cells and so that an optimized photon-electron conversion efficiency.[1-31]

1.5.2 Working principle of organic solar cells

- Short circuit current and quantum efficiency

In solar cells, the photocurrent is generated by the absorption of photons, which are extracted as electron-hole pairs eventually. In the device, electrons have to be collected at some position that away from the holes. In case of organic solar cells, the main characteristic is that the free electron-hole pairs cannot be generated directly via light absorption. Instead, localized excited states or highly bound excitons would be generated. The separation of the exitons and the extraction of charged carriers are quite crucial in generating

current. Unfortunately, the efficiency of exciton dissociation is so limited in single layer devices due to the lack of the interfaces. As a result, a donor-acceptor heterojunction was utilized. In this architecture, the donor and acceptor are organic materials with different ability of accepting electrons (or holes). It is generally convinced that this heterojunction system is favorable for the electrons to transport in an orbital located close to the LUMO in acceptor material and makes the formal neutral acceptor into an anion. And the driving force for this procedure is the energy difference between the LUMO level of acceptor material and the HOMO level of the donor material.

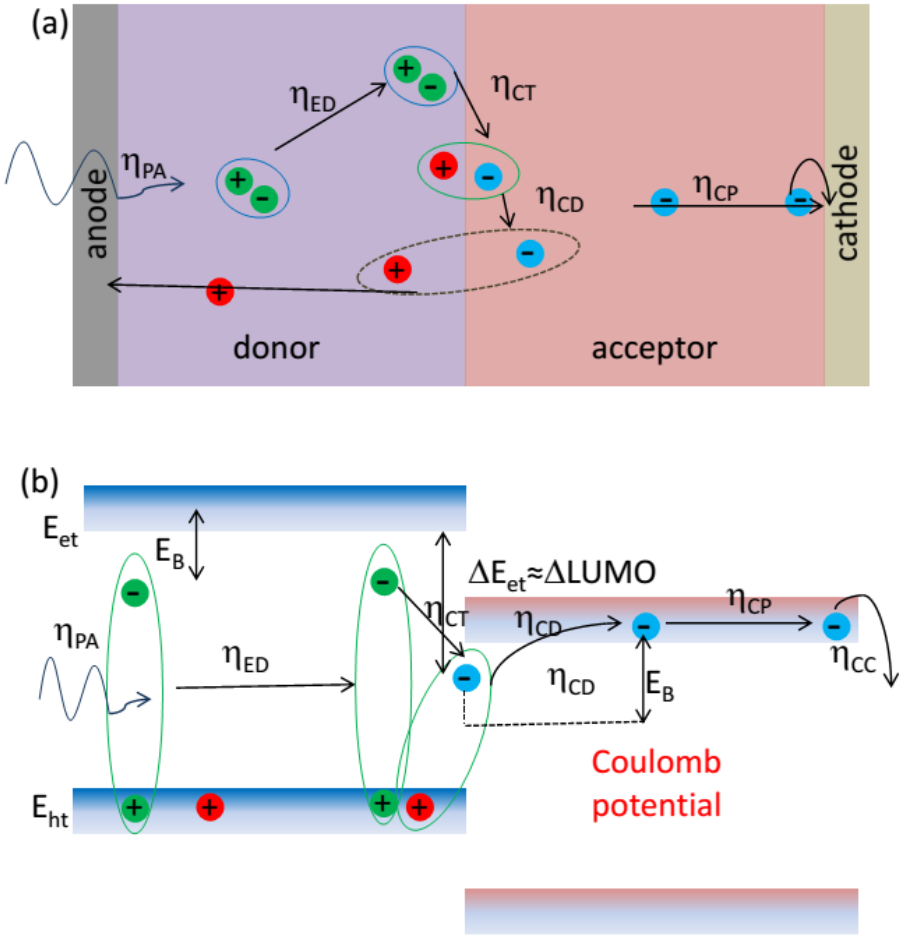

Fig. 1-11. Depicts of energy conversion processes in organic solar cells, with corresponding quantum efficiencies. (PA: photo absorption, ED: excitons diffusion, CT: charge transfer, CD: dissociation of charged carrier pairs, CP: charge transport and CC: charge collection)

The current generation process is illustrated in Fig. 1-11. After being excited by the incident light, the photons will be absorbed by the active materials with an efficiency of η_{PA}, which depends on the absorption coefficient of the absorber. After being generated in the active layer, reaching the donor-acceptor interface is the prerequisite for the excitons to dissociate. In this process, the diffusion and relaxation will compete with each other with an efficiency of η_{ED}, which is determined by the diffusion length L_D. $L_D = \sqrt{D\tau}$, in which D and τ are diffusivity of the absorber and exciton lifetime. Typically, L_D is ~10 nm[1-38]. Therefore, in order to get the maximum η_{ED}, there are two main solutions: one is to fabricate a bilayer device with absorber thickness of ~10 nm and the other is to fabricate donor-acceptor blending active layers. After dissociation,

charges will then be transported at an efficiency of η_{CT}. The charge transport is an ultra fast process that brought about at the donor-acceptor interface, typically less than a few hundreds of femtoseconds.[1-39~1-42] At the donor-acceptor interface, the electron-hole pair will be separated at an efficiency of η_{CT}. This process is still not yet understood completely. After separation, charges will transport through the organic semiconductors and they will be collected by the electrodes with an efficiency of η_{CP}. Then recombination of holes and electrons is the only remaining loss path. In a bilayer device, the recombination between the opposite charged carriers is expected to be low since they are located separately in donor and acceptor layers. On the contrary, for blended bulk device, electrons and holes can meet each other during extraction and recombine non-geminately. After transportation of the electrons and holes, they then are collected by the cathode and anode at an efficiency of η_{CC}. This is only a direct loss path if contacts are not selective and a charge carrier diffuses along the wrong direction to the opposite electrode.

The overall efficiency, so-called external quantum efficiency is given by the formula: $EQE = \eta_{PA}\eta_{ED}\eta_{CT}\eta_{CD}\eta_{CP}\eta_{CC}$, which is directly proportional to the short current density (J_{SC}) of the device.

- Open circuit voltage (V_{OC})

The V_{OC} is the bias voltage to be applied in order to evanish the photo-generated current. Therefore, at V_{OC}, there will be no external current flowing through the out circuit of the solar cell even the cells are irradiated by the sun light. In a single layered OSC, the V_{OC} is directly proportional with the work function difference of the anode and cathode. And it is easy to understand that V_{OC} is impossible to exceed the work function difference of the electrodes.[1-43,1-44] In a conventional p-n junction, the maximum V_{OC} can be described by the following equation:[1-45]

$$eV_{OC} = \frac{k_B T}{e} ln\left(\frac{j_\gamma^{abs}}{j_\gamma^0}\right), \tag{1-2}$$

here, e is the elementary charge, k_B is the Boltzmann constant, T is the temperature in Kelvin, j_γ^{abs} is the absorbed photon flux and the j_γ^0 is the recombination flux. Considering that the free carriers generation and recombination are carried out mainly at the donor-acceptor interface, we can suppose that the processes limiting V_{OC} also take place at such interfaces. If we ignored the recombination losses, the V_{OC} can be described by:

$$eV_{OC} = E_F^n - E_F^p = E_g^{DA} - k_B T ln\frac{N_C N_V}{np}, \tag{1-3}$$

in which n,p and E_g^{DA} represent the charge carrier densities at the heterojunction, respectively. N_C, N_V are effective density of states. Eq. 1-2 describes the V_{OC} ignoring the recombination losses. In case of conbining the recombination loss, V_{OC} could then be described as:

$$eV_{OC} = E_{CT} + k_B T ln\left(\frac{J_{SC} h^3 c^2}{fe2\pi(E_{CT}-\lambda)}\right) + k_B T ln(EQE_{EL}). \tag{1-4}$$

- Fill factor (FF)

The definition of FF is shown in Fig. 1-12. The main function of a solar cell is to generate electricity or power. The fourth quadrant of the J-V curve shows the power that a cell can deliver, where a point can be found. At this point, the delivered power maximized, so-called maximum power (P_{max}). The FF is defined by Eq. 1-5:

$$FF = \frac{P_{max}}{P_{theomax}} = \frac{(J \cdot V)_{max}}{J_{SC} \cdot V_{OC}}. \tag{1-5}$$

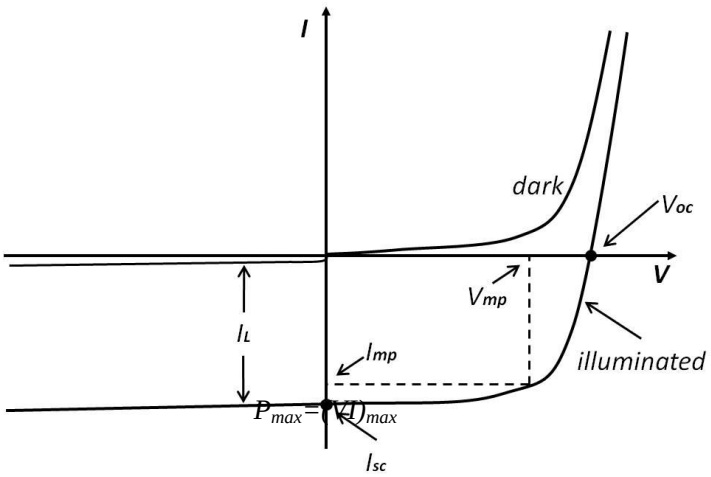

Fig. 1-12. Definitions of V_{OC}, I_{SC} (J_{SC}), *FF* and P_{max}.

The *FF* is a measure for the diode characteristics of the photovoltaic devices. A higher *FF* means a more ideal diode. Ideally, the *FF* should be unity, but due to energy losses during the operation that may be caused by the transport barrier or charge recombination. The value of *FF* is generally found to be in between 0.2-0.8 for organic photovoltaic devices.[1-46] The *FF* is greatly affected by the mobility of the mobility of charge carriers. Moreover, series and shunt resistance are also found to be the limiting factors of *FF*. In order to obtain a higher *FF*, a maximum shunt resistance and a minimized series resistance are required.

- The power conversion efficiency (*PCE*)

  The maximum power conversion efficiency of a single band edge absorber as a function of the bandgap is derived by Shockley and Queisser:[1-47]

$$J(V, E_g) = e\left(j_\gamma(E_g) - R_0(E_g)e^{\frac{eV}{k_B T}}\right), \tag{1-6}$$

here, *J* is the current, *e* is the elementary charge, j_γ is the total photo flux from the sun, R_0 is the radiative loss. Then the maximum power can be calculated by finding the maximum of the electrical power $J \times V$. The power conversion efficiency (η) is given by:

$$\eta = \frac{J_{SC} V_{OC} FF}{P_\gamma}. \tag{1-7}$$

FF is the fill factor and P_γ is the incident light intensity.

1.5.3 The main advantages of organic solar cells

The most attractive advantage of the OSCs can be the low cost, because one of the important objectives for renewable energies is to be affordable. For one thing, the variety of the fabrication technologies such as spin coating, roll-to-toll printing or other low-temperature deposition methods, and for another, the diversity of the organic materials due to the toolbox of organic chemistry, make the fabrication of OSCs can be fabricated at a fairly low cost. Besides, the majority of the OSCs have good performance at low light intensity and a positive temperature coefficient of the efficiency, which ensure a priority of high energy yield. In addition, the preponderances of OSCs also include the non-toxicity, applicable in mobile devices and short pay-back time.

1.5.4 Challenges in organic solar cells

Realizing the potential properties of OSCs is the main challenge in which the most important thing is to compete with the traditional solar cells. As aforementioned, the crystalline silicon solar cells showed a tremendous reduction of production costs in the last decade. Furthermore, the developments in inorganic thin-film photovoltaics show the potential of these technologies to achieve the advantages of organic photovoltaics mentioned above, *e.g.*, mechanical flexibility and potable. For this reason, exceeding a *PCE* of 10% is of great significance in organic photovoltaic devices. At present, in the long term and for the large output on TW scale, the silicon and organic solar cells are the only two technologies that meet the requirement of material abundance.

The performance optimization of the OSCs is hindered by the void of understanding in the physical nature of the organic semiconductors, which are directly related to the charge generation, transportation, recombination *et al*.

1.6 Theoretical concepts

Due to the disorderd nature of organic semiconductors, traps are ubiquitous in organic materials. The presence of traps and charge trapping will affect the performance of organic semiconductor-based devices in various ways. This section will give a brief introduction on the charge trapping and recombination in organic semiconductors.

1.6.1 Defects and trapped charge

- Self-trapping

The charge trapping plays a dominant role in determining the mobility of the carriers and hence also the conductivity of the material. However, even if there were no impurities and no crystal defects, charge trapping could also take place as a result of a self-made local angulations or distortion. Thus, the transport of charge depends not only on the presence of defects but also on the interaction between the excess carriers and phonons in the lattice. In pure crystals, the degree of spatial localization of the charge will affect the behavior of the excess carrier states, depending on the phonon-carrier interaction. The typical mobility for a delocalized charge is characterized to be larger than 1 $cm^2V^{-1}s^{-1}$ with a temperature coefficient varying as T^n, in which $n>1$. While for the localized charges, they show a mobility less than 1 $cm^2V^{-1}s^{-1}$ and has an activation energy. The coexistence of the two types of behavior is principally possible, in particular, the material is highly anisotropic. The scale of mobility $\approx$1 $cm^2V^{-1}s^{-1}$ equal to a situation obtains in which relatively small effects can combine to change a delocalized charge state into a localized state.

- Defects in organic crystals

The presence and distribution of trapping states dominates the carrier transport in organic semiconductors. The defects in the organic crystal are playing a crucial role in trapping carriers. Carrier trapping may be caused by chemical or physical impurities. The defects could either be located at designated lattice sites or at some other place where they may possess extended characters: the twin planes or amorphous grain boundaries. The available energy levels could be modified by the defects. The presence of the defects tends to be leading to extra orbitals in the energy gap $E_{g.}$ Therefore, the carrier is quite possible to become localized or trapped. The category of the traps are dependent on the

semiconductor itself and in some materials, the traps are primarily neutral and will be charged after being filled by carriers. Although some defects do not trap charges, they may also act as carrier scattering centers.

The lattice deformation will generate unoccupied lattice sites, so-called vacancies. A lattice vacancy will behave like a free surface for the carrier that is located next to the vacancy because its polarization energy will decrease. From this point of view, the vacancy always tends to act as an antitrap and scatters the carrier instead of trapping it. This is quite different from the role of vacancies in ionic crystals, in which vacancies are always charged and trap the opposite carriers.

Likewise, other defects like point defects, line defects and will also play roles in trapping or scatter centers carriers in organic semiconductors.

- Surface traps

Except for the carrier traps in the bulk of a material, they may also exist at the materials surface. It is actually far more likely for the impurities, especially the chemical impurities, to be present at the surface region than that in the bulk. Apart from the possibility of traps at the surface of the material that is associated with a foreign molecule.

A surface space charge layer will be produced if there were traps at the material surface. This is due to the charge exchange between the surface region and the bulk region. The charge redistribution will then result in band bending at the surface region. The surface phenomena that caused by the surface space charge layer will play a major role in determining the charge injection efficiencies of an organic material, unless the surface is kept extremely clean. These effects will definitely lead to the differences in the contact potential.

The polarization energies will diminish only at a free surface of a perfect organic single crystal. This is ascribed as the absence of dangling bonds at the surface and as well as the polarizable medium in the top molecular layer. Accordingly, the gap between HOMO and LUMO for a clean surface of a known material increases here and no surface trapping sites for the charged carriers exist.

- Chemically induced trapping levels

The host material obviously possesses an energy level that is different from that of the impurity, hence traps will be formed at the chemical impurity. Particularly, their ionization energy and electron affinity are different. These divergences form the basis for the formation of the carrier traps. As an example, if the ionization energy of the impurity is higher than that of the host, the impurity will behave as an electron trap while as a hole trap in case of the electron affinity greater. An impurity can behave both as an electron trap and a hole trap, even though the trap depth will basically not be the same for each carrier.

Similarly, the traps will also generate at the host molecules that adjacent to the chemical impurity. It is very likely that the chemical impurity is energetically inert as a carrier trap in the sense that its ionization energy is greater and its electron affinity is less than that of the host.

- Detrapping process

Carriers trapped within the bulk or at the interface of the material can be restored as mobile by several detrapping processes. In some cases, trap emptying could bring about through the phonons absorption from the local surroundings, which is called the thermal detrapping. In inorganic semiconductor, for an electron at trap depth E_t below the conduction level E_C, the probability per unit time p (E_t) for this detrapping process is given by the standard Boltzmann expression:

$$p(E_t) = \upsilon exp[-(E_c - E_t)/k_B T], \quad (1\text{-}8)$$

ν stands for the frequency factor at which the charges are attempting to escape, which is described by $\nu=\mu\sigma N_c$. μ is the free electron thermal velocity in the conducting band, σ is the electron-capture cross section by the trap, and N_C is the effective density of states, kT stands for the conducting band edge.

Thermal detrapping is more general in shallow traps as compared with the deep traps. It can be easily distinguished from other mechanisms by performing the measurements at low temperatures when other detrapping effects are not competitive. E_t is determined by the temperature dependent detrapped carrier current.

Besides thermal detrapping, optical and electric field detrapping are other two main effects. Light absorption not only directly detrap carriers through photon absorption by the trapped charge, but also indirectly through the formation of triplet or singlet exciton intermediates that are subsequently absorbed by the trapped charge. The formed triplet or singlet exciton intermediates then lower the height of the charge localized barrier and assist detrapping. If the carrier is trapped in the coulombic well of an opposite charge, this process is then called the Poole-Frenkel effect. It should be noted that if the carrier is trapped in an neutral site, the external field will have a much smaller detrapping effect.

1.6.2 Recombination

After been excited by electron beam or light absorption, a semiconductor will become thermodynamic nonequilibrium due to the creation of the excess charges. After turning off the external excitation, the carriers will relax into lower energetic states. This process is recombination. Often, in the simplest way, the carrier generation rate is G under certain excitation. In the steady-state excitation, a constant excess charge carrier density is present. Then the generation exactly compensates the recombination processes.

- Radiative recombination (band to band recombination)

In traditional inorganic semiconductors, the band-band recombination is the relaxation from an electron in the conduction band into the valence, where an empty state is a hole. In a direct semiconductor, electrons can make an optical transition between the bottom of the conduction band to the valence band top. In indirect semiconductor, this process is only possible with the assistance of a phonon and is thus much less probable. Due to the direct combination of an electron and a hole, this kind of recombination is companied by the release of phonon. As a result, the emitted phonon has an energy similar to the band gap and is only weakly absorbed such that it can exit the semiconductor.

In case of organic semiconductor, the radiative recombination is classified as bimolecular recombination, which is depicted in Fig. 1-13.[1-48]

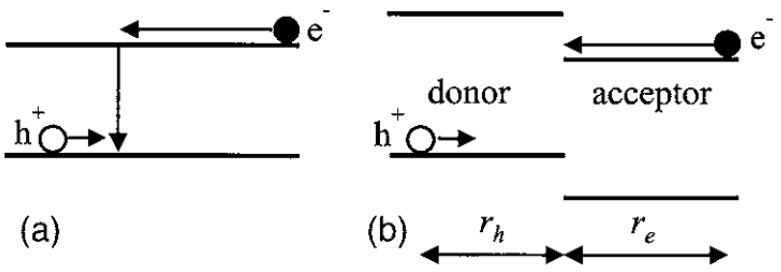

Fig. 1-13. Schematic semiconductor energy diagram showing bimolecular recombination in (a) pristine

semiconductors and (b) in heterojunction devices.

The bimolecular recombination is an important loss mechanism in OSCs and its rate R follows the Langevin recombination model, described by Eq. 1-7:

$$R = \gamma(np - n_{int}p_{int}), \tag{1-9}$$

where $n(p)$ is the mobile electron (hole) density, n_{int} (p_{int}) is the intrinsic electron (hole) density and γ is the Langevin recombination constant.

- Non-radiative recombination

At certain temperature, the requirement of thermaodynamic radiation of bodies makes the rediative recombination unavoidable. Except for the radiative recombination, there are other recombination processes which also play significant roles in influencing the device performances. The non-rediative recombination processes in a traditional inorganic semiconductor are sketched in Fig. 1-14.

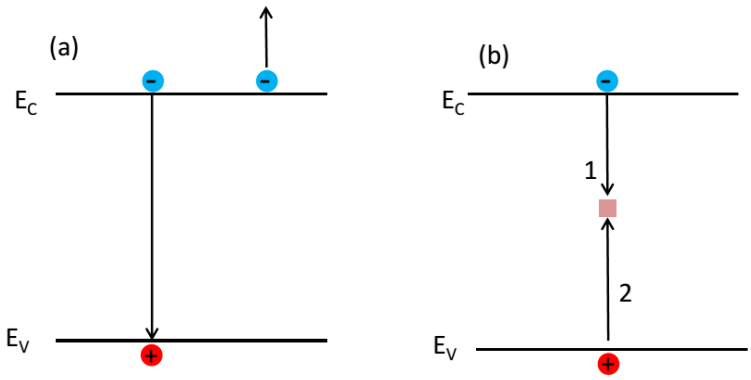

Fig. 14. Non-radiative recombination processes in semiconductor: (a) Auger transferring the energy to another electron and hole and (b) trap-assisted recombination.

The Auger recombination is a process in which the energy of a recombining electron-hole pair is transferred to another electron or hole. In indirect semiconductors, this recombination is quite important because owing to the conservation of the crystal momentum. Actually, recombination via intra-bandgap states is dominant in real semiconductors. These intra-bandgap states are above mentioed traps. The trap-assisted recombination can be explained by the Shockley-Read-Hall model as a two-step process: (1) a carrier is captured by the trap and become immobile (trapping effect) and (2) the carrier is emitted to corresponding band. The step 2 is equivalent to a capture of another carrier with the opposite sign.

To optimize the performance of organic solar cells, the material synthesizing and device structure engineering are two main topics. The progress that has been achieved is mainly on these topics. The energy loss caused by bimolecular recombination and trap-assisted recombination that are still in huge controversy for OSCs is thus the subject of this thesis.

1.7 The structure of this thesis

The thesis is organized like this. The background and brief introduction was given in this chapter. In chapter 2, the materials, the experimental details as well as the setup of the measurements were summarized; the theoretical models of transient measurements are explained as well. Chapters 3, 4 and 5 are the results and discussions. In chapter 3, the effect of bathocuproine cathode buffer in inverted small molecule planar

devices was investigated and the reason for the poor performance of the device free of cathode buffer is revealed. Chapter 4 mainly discusses the underlying physic mechanisms in the degradation of planar OSCs. In order to rule out the electronic and morphological changed induced by different buffers, the conventional and inverted devices were fabricated with identified materials and the fabrication procedures accommodated with each other. And the last part of result and discussion is on the factor that determines the open circuit voltage of small molecule bulk devices. These works are all dedicated to clarifying the effect of charge trapping and recombination in small molecule organic photovoltaic devices with various structures and systems.

Finally, the conclusion will be presented in Chapter 6. The effects of charge trapping and recombination in OSCs, especially in small molecular device systems were illustrated, either for the freshly fabricated devices or for the aged devices. The work presented in this thesis is just a work that beneath discussion and there are still many mysteries waiting for solving and the ready-to-do works will be also presented in the final chapter.

References

[1-1] Heliatek. Heliatek Consolidates Its Technology Leadership by Establishing a New World Record for Organic Solar Technology with a Cell Efficiency of 12%. (2013).

[1-2] T.L. Steck, A. Sharma, P. Bartelmus. Human Population Explosion. (2008).

[1-3] W. Lutz, W. Sanderson, S. Scherbov. The End of World Population Growth. Nature, **412** (2001) 543.

[1-4] C. Ponting, A Green History of the World, Sinclair-Stevenson London. (1991).

[1-5] B. petroleum. Statistical Review of World Energy. (2014).

[1-6] R.E. Smalley. Future Global Energy Prosperity: The Terawatt Challenge. MRS Bulletin, **30** (2005) 412.

[1-7] V. Balan. Current Challenges in Commercially Producing Biofuels from Lignocellulosic Biomass. International Scholarly Research Notices. (2014).

[1-8] M.A. Green, K. Emery, Y. Hishikawa, W. Warta, E.D. Dunlop. Solar Cell Efficiency Tables (Version 45). Progress in Photovoltaics: Research and Applications, **23** (2015) 1.

[1-9] K. Wu, Q. Li, Y. Du, Z. Chen, T. Lian. Ultrafast Exciton Quenching by Energy and Electron Transfer in Colloidal CdSe Nanosheet-Pt Heterostructures. Chemical Science, **6** (2015) 1049.

[1-10] S. Nakade, Y. Saito, W. Kubo, T. Kitamura, Y. Wada, S. Yanagida. Influence of TiO_2 Nanoparticle Size on Electron Diffusion and Recombination in Dye-Sensitized TiO_2 Solar Cells. The Journal of Physical Chemistry B, **107** (2003) 8607.

[1-11] J. You, L. Dou, K. Yoshimura, T. Kato, K. Ohya, T. Moriarty, K. Emery, C-C. Chen, J. Gao, G. Li. A Polymer Tandem Solar Cell with 10.6% Power Conversion Efficiency. Nature Communications, **4** (2013) 1446.

[1-12] M. Hiramoto, M. Kubo, Y. Shinmura, N. Ishiyama, T. Kaji, K. Sakai, T. Ohno, M. Izaki. Bandgap Science for Organic Solar Cells. Electronics, **3** (2014) 351.

[1-13] http://commons.wikimedia.org/wiki/File:Best_Research-Cell_Efficiencies.png.

[1-14] M.A. Green, K. Emery, Y. Hishikawa, W. Warta. Solar Cell Efficiency Tables (Version 33). Progress in Photovoltaics: Research and Applications, **17** (2009) 85.

[1-15] M.A. Green, K. Emery, Y. Hishikawa, W. Warta, E.D. Dunlop. Solar Cell Efficiency Tables (Version 39). Progress in Photovoltaics: Research and Applications, **20** (2012) 12.

[1-16] M.A. Green, K. Emery, Y. Hishikawa, W. Warta, E.D. Dunlop. Solar Cell Efficiency Tables (Version 44). Progress in Photovoltaics: Research and Applications, **22** (2014) 701.

[1-17] B. Averill, P. Eldredge. General Chemistry: Principles, Patterns, and Applications. (2011).

[1-18] C.W. Tang. Two-Layer Organic Photovoltaic Cell. Applied Physics Letters, **48** (1986) 183.

[1-19] A. Miller, E. Abrahams. Impurity Conduction at Low Concentrations. Physical Review, **120** (1960) 745.

[1-20] R. Schmechel. Gaussian Disorder Model for High Carrier Densities: Theoretical Aspects and Application to Experiments. Physical Review B, **66** (2002) 235206.

[1-21] D. Monroe. Hopping in Exponential Band Tails. Physical Review Letters, **54** (1985) 146.

[1-22] M. Pope, C.E. Swenberg. Electronic Processes in Organic Solids. Annual Review of Physical Chemistry, **35** (1984) 613.

[1-23] S. Baranovski, Charge Transport in Disordered Solids with Applications in Electronics, John Wiley & Sons. (2006).

[1-24] H. Bässler. Charge Transport in Disordered Organic Photoconductors a Monte Carlo Simulation Study. Physica Status Solidi (b), **175** (1993) 15.

[1-25] S. Baranovskii, P. Thomas, G. Adriaenssens. The Concept of Transport Energy and Its Application to Steady-State Photoconductivity in Amorphous Silicon. Journal of Non-Crystalline Solids, **190** (1995)

283.

[1-26] G. Horowitz, R. Hajlaoui, P. Delannoy. Temperature Dependence of the Field-Effect Mobility of Sexithiophene. Determination of the Density of Traps. Journal de Physique III, **5** (1995) 355.

[1-27] J. Noolandi. Multiple-Trapping Model of Anomalous Transit-Time Dispersion in a-Se. Physical Review B, **16** (1977) 4466.

[1-28] H. Kallmann, M. Pope. Photovoltaic Effect in Organic Crystals. The Journal of Chemical Physics, **30** (1959) 585.

[1-29] G. Chamberlain. Organic Solar Cells: A Review. Solar Cells, **8** (1983) 47.

[1-30] M. Hiramoto, H. Fujiwara, M. Yokoyama. Three-Layered Organic Solar Cell with a Photoactive Interlayer of Codeposited Pigments. Applied Physics Letters, **58** (1991) 1062.

[1-31] G. Yu, J. Gao, J.C. Hummelen, F. Wudl, A.J. Heeger. Polymer Photovoltaic Cells: Enhanced Efficiencies Via a Network of Internal Donor-Acceptor Heterojunctions. Science-AAAS-Weekly Paper Edition, **270** (1995) 1789.

[1-32] H. Spanggaard, F.C. Krebs. A Brief History of the Development of Organic and Polymeric Photovoltaics. Solar Energy Materials and Solar Cells, **83** (2004) 125.

[1-33] W. Salaneck. Intermolecular Relaxation Energies in Anthracene. Physical Review Letters, **40** (1978) 60.

[1-34] J. Riga, J. Pireaux, R. Caudano, J. Verbist. A Comparative ESCA Study of the Electronic Structure of Solid Acenes: Benzene, Naphthalene, Anthracene, and Tetracene. Physica Scripta, **16** (1977) 346.

[1-35] V. Choong, Y. Park, Y. Gao, T. Wehrmeister, K. Müllen, B. Hsieh, C. Tang. Dramatic Photoluminescence Quenching of Phenylene Vinylene Oligomer Thin Films Upon Submonolayer Ca Deposition. Applied Physics Letters, **69** (1996) 1492.

[1-36] J. Halls, K. Pichler, R. Friend, S. Moratti, A. Holmes. Exciton Diffusion and Dissociation in a Poly (P-Phenylenevinylene)/C_{60} Heterojunction Photovoltaic Cell. Applied Physics Letters, **68** (1996) 3120.

[1-37] J. Halls, R. Friend. The Photovoltaic Effect in a Poly (P-Phenylenevinylene)/Perylene Heterojunction. Synthetic metals, **85** (1997) 1307.

[1-38] P. Peumans, A. Yakimov, S.R. Forrest. Small Molecular Weight Organic Thin-Film Photodetectors and Solar Cells. Journal of Applied Physics, **93** (2003) 3693.

[1-39] N. Sariciftci, L. Smilowitz, A.J. Heeger, F. Wudl. Photoinduced Electron Transfer from a Conducting Polymer to Buckminsterfullerene. Science, **258** (1992) 1474.

[1-40] C.J. Brabec, G. Zerza, G. Cerullo, S. De Silvestri, S. Luzzati, J.C. Hummelen, S. Sariciftci. Tracing Photoinduced Electron Transfer Process in Conjugated Polymer/Fullerene Bulk Heterojunctions in Real Time. Chemical Physics Letters, **340** (2001) 232.

[1-41] J.G. Müller, J.M. Lupton, J. Feldmann, U. Lemmer, M.C. Scharber, N.S. Sariciftci, C.J. Brabec, U. Scherf. Ultrafast Dynamics of Charge Carrier Photogeneration and Geminate Recombination in Conjugated Polymer: Fullerene Solar Cells. Physical Review B, **72** (2005) 195208.

[1-42] A.A. Bakulin, D.S. Martyanov, D.Y. Paraschuk, M.S. Pshenichnikov, P.H. van Loosdrecht. Ultrafast Charge Photogeneration Dynamics in Ground-State Charge-Transfer Complexes Based on Conjugated Polymers. The Journal of Physical Chemistry B, **112** (2008) 13730.

[1-43] H. Frohne, S.E. Shaheen, C.J. Brabec, D.C. Müller, N.S. Sariciftci, K. Meerholz. Influence of the Anodic Work Function on the Performance of Organic Solar Cells. ChemPhysChem, **3** (2002) 795.

[1-44] B.A. Gregg. Excitonic Solar Cells. The Journal of Physical Chemistry B, **107** (2003) 4688.

[1-45] S.M. Sze, K.K. Ng, Physics of Semiconductor Devices, John Wiley & Sons. (2006).

[1-46] H. Kim, S.H. Jin, H. Suh, K. Lee. Origin of the Open Circuit Voltage in Conjugated Polymer-Fullerene Photovoltaic Cells, Optical Science and Technology, SPIE's 48th Annual Meeting, International Society

for Optics and Photonics, (2004) 111.

[1-47] W. Shockley, H.J. Queisser. Detailed Balance Limit of Efficiency of P-N Junction Solar Cells. Journal of Applied Physics, **32** (1961) 510.

[1-48] L. Koster, V. Mihailetchi, P. Blom. Bimolecular Recombination in Polymer/Fullerene Bulk Heterojunction Solar Cells. Applied Physics Letters, **88** (2006) 052104.

Chapter 2 Fabrication and Characterization Methodologies

2.1 Brief introduction of used materials

In this section the materials which are employed to realize the above-mentioned various functions (donor, acceptor and charge transport layers) are introduced and their properties are discussed. The performance of OSC differs depending on the properties and stacking of composed functional materials. The primary requirement for the charge transport layers is the highly transparency in visible spectral range. To achieve efficient hole and electron transport, for the hole transport layers (HTL), a HOMO in the range of the HOMO for the absorber materials is necessary while a LUMO in the range of LUMO for acceptor in electron transport layers (ETL). Considering in OSCs, the grain boundaries are the main factor that limits the charge transport,[2-1] the crystallization of absorber will benefit the device performance due to a higher exciton diffusion length and charge carrier mobility.[2-2,2-3] On the contrary, to provide a smooth underneath layer for the active materials, the charge transport layers are preferred to grow amorphous.

2.1.1 Donor

In this work, boron phthalocyanine chloride (SubPc) is used as donor materials. The structure of SubPc is shown in Fig. 2-1. SubPc has a relatively cone-shaped molecule structure with an extended aromatic system. Central B-Cl atom can be exchanged by other elements and the exchange will lead to energetic changes[2-4] as well as absorption properties due to a large interaction of the metal atom with π system. The absorption will be shifted towards lower energies if exchanged the metal into Sn, Pb and Cl-Al.[2-5,2-6] MPcs are most common absorbers in small molecule OSCs.[2-7,2-8] The absorbance of SubPc is shown in Fig. 2-2 and the absorption peak is around 590 nm. The absorption band in the visible range peaked at 587 nm is called Q-band while that in the UV range centered at 308 nm is called B-band. Both of them are attributed to the π-π^* transition.[2-9] The deep HOMO of SubPc (-5.2 eV[2-10]) and the high absorption coefficient of ~10^5 cm^{-1} makes SubPc an ideal donor molecule[2-11].

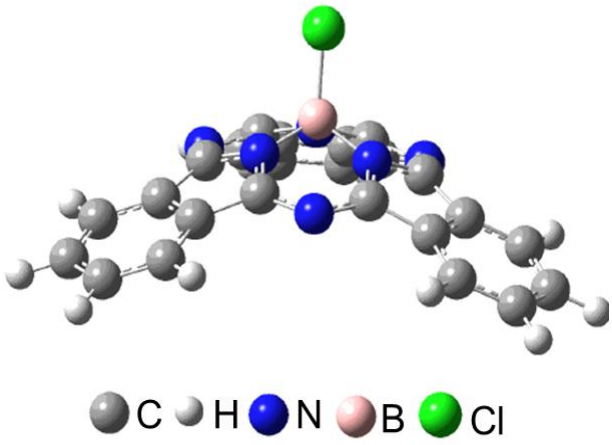

Fig. 2-1. The chemical structure of SubPc.

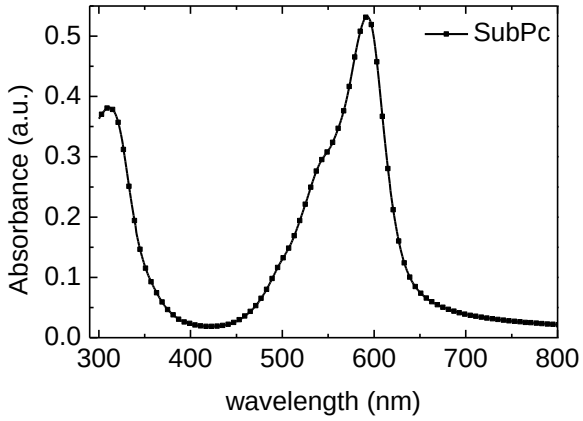

Fig. 2-2. Absorption spectrum of SubPc thin film (thickness: 50nm).

2.1.2 Acceptor

In this work we use C_{60} as the acceptor since it has intrinsic electron mobility of as high as 1 $cm^2 V^{-1} s^{-1}$,[2-12] which makes it promising acceptor material. Besides, the band gap of C_{60} is 1.7 eV and it also has a deep lying LUMO level of -4.0 eV.[2-10] The chemical structure of C_{60} is shown in Fig. 2-3 and the absorption spectrum in Fig. 2-4.

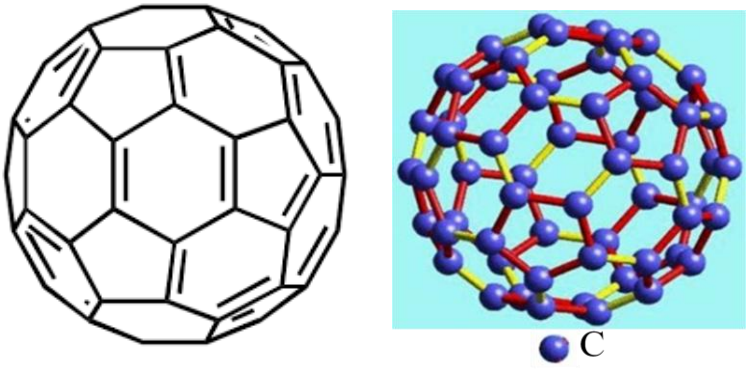

Fig. 2-3. Chemical structure of C_{60}.

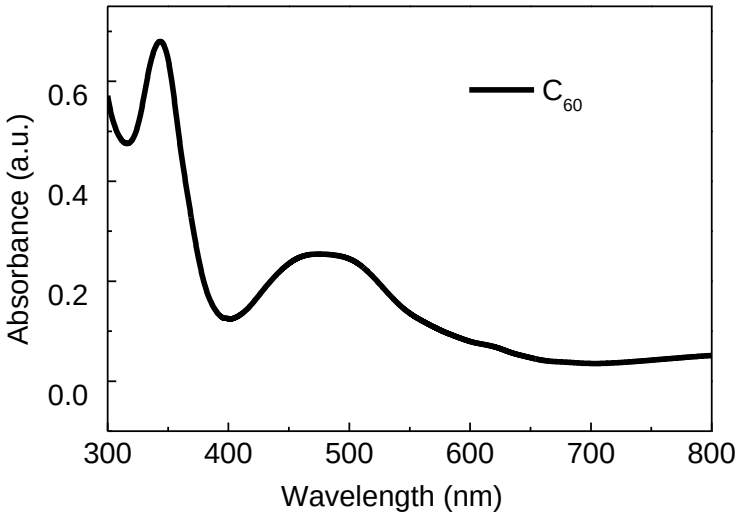

Fig. 2-4. Absorption spectrum of C_{60} thin films (thickness: 50 nm).

2.1.3 Charge transport layers

- Hole transport layer (HTL)

Molybdenum trioxide (MoO_3) is used as hole transport material in this work, which is a p-type conducting semiconductors with an electron affinity (E_A) and ionization energy (*IE*) on the order of 2.3 and 5.3-5.4 eV, respectively.[2-13~2-15] The charges in MoO_3 are mainly transported via the valence band. Also the interactions between MoO_3 and organic active materials hole will benefit the hole transportation and extraction, *i.e.*, band bending induced p-doping of the interface can lead to a built-in field that enhances hole extraction in OLED and reduces recombination in OSCs;[2-16~2-18] the insertion of MoO_3 can also significantly reduce the conductor resistance;[2-15] besides, some interfaces such as ITO/MoO_3 display a significant density of gap states which provide extra charge transport paths, as observed on ultra thin MoO_3 layer (1 nm).[2-19] In addition, the MoO_3 is commonly used in organic devices also due to a fairly low deposition temperature (~ 400 ℃) and the chemical stability of MoO_3. However, MoO_3 is insulator in nature, with a considerably low conductivity (100 nm thick film with a conductivity of 1×10^{-7} S/cm). Therefore, the thick MoO_3 films will increase the resistance of organic devices and in general the MoO_3 hole transport layer in OSCs is no thicker than 50 nm.[2-20,2-21]

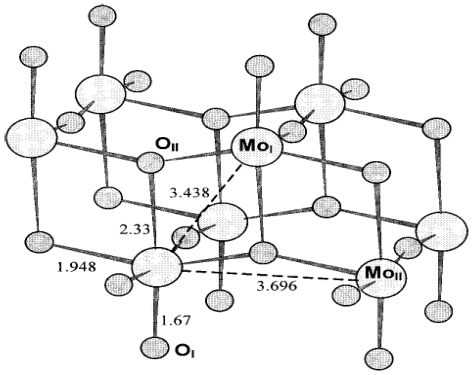

Fig. 2-5. Crystal structure of MoO_3.

- Electron transport layer (ETL)

The 2,9-dimethy1-4,7-dipheny1-1,10-phenanthroline, known as bathocuproine (BCP) is a commonly used organic material in both organic solar cells and organic light-emitting diodes (OLEDs). The chemical structure of BCP is displayed in Fig. 2-6. Although the BCP has been vastly used in OSCs with conventional structure, the application and effect of BCP in inverted devices are still unclear and therefore one of the topics of this thesis.

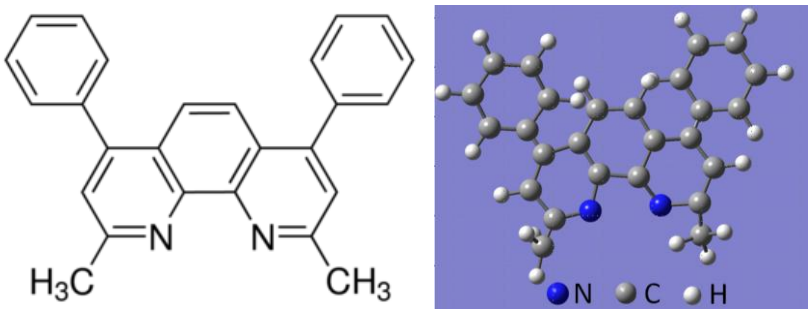

Fig. 2-6. Chemical structure of BCP (left) and the molecular geometry calculated by Gaussian 03 (right).

2.1 Purification of source materials

The presence of impurity is strongly influencing the electronic properties of semiconductors due to the dopping effects. One example is the decreased low-temperature hole mobility of anthracene with an impurity concentration as low as 10^{-7} g/mol (99.99999% purity).[2-22] For this reason, the purity of as-received materials is not sufficient for the organic devices application and purification of source materials is essential. Further, purification is also required to prevent contaminants from entering the high vacuum chamber which might result in a high background pressure, as well as constant source of contamination of the subsequently grown films due to outgassing from the deposits in the chamber itself. There are several purification techniques, chromatography,[2-23] zone refining from the melt,[2-24] gradient sublimation[2-23] and so on. Although the highest purity organic material was achieved by zone refining,[2-24,2-25] considering that the organic powders used in this work do not have a liquid phase at atmospheric pressure or below, gradient sublimation is the most useful technique and the purification method of this work.

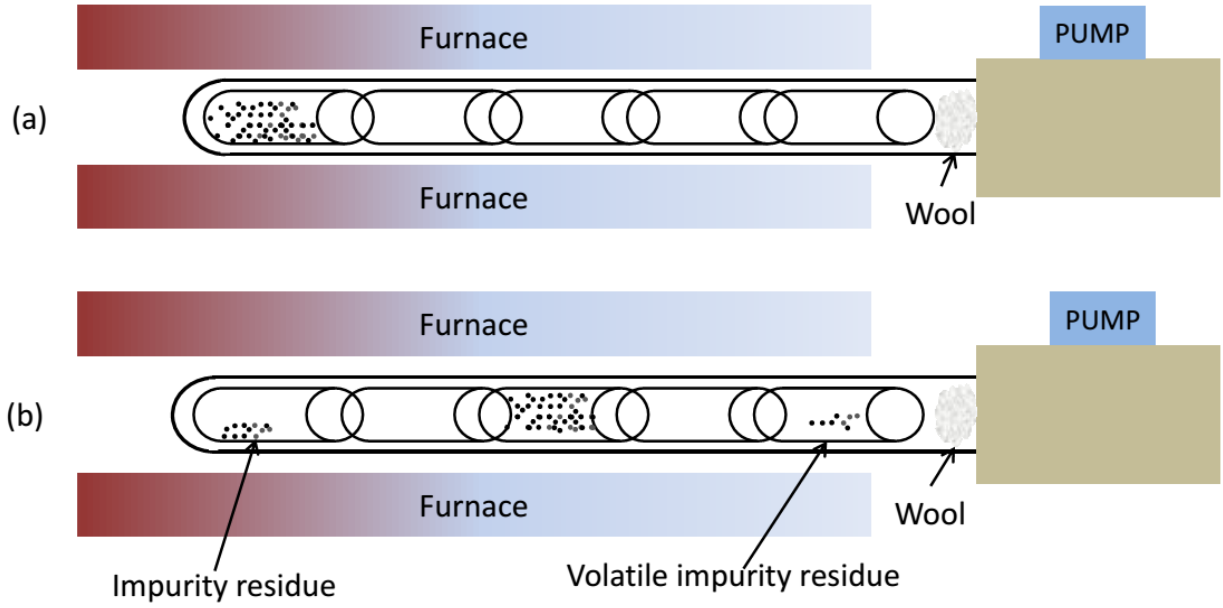

Fig. 2-7. Schematic representation of a sublimation tube.

Fig. 2-7 shows the gradient sublimation tube and the purification process is as follows: 1) load the source material (SubPc, C_{60}, BCP) obtained from a commercial source into the end of the glass tube (see Fig. 2-7(a)); 2) place other sleeves inside the tube to capture the sublimed material and also impurity; 3) put a wad of wool at the open end of the tube to prevent the material from contaminating the pumping system; 4) evacuate the tube until reaching ~ 10^{-6} Torr and insert the tube into the furnace; 5) gradually increase the furnace temperature to the sublimation point of the source material (approximately 200 ℃, 400 ℃ and 80 ℃ for SubPc, C_{60} and BCP, respectively). This process usually takes 24 hours and the purified material will be captured by the 3rd sleeve and volatile impurity is evacuated to the open end which is connected with the vacuum system while nonvolatile impurities are left at the hottest end of the tube (see Fig. 2-7(b)). The purified materials will be extracted to be used as source material for the next purification cycle. The organic materials are often purified in multiple cycles by gradient sublimation before being loaded into the high vacuum evaporation system. After being purified for 3 cycles, the materials were then be loaded into the Knudsen-cells (K-cells)where they are continuously maintained in ultrahigh vacuum at elevated temperatures awaiting growth.[2-22]

2.2 Fabrication details

2.2.1 Patterning of Indium Tin Oxide (ITO) coated glass substrate

In order to produce multiple devices and define the exact device area, prior to deposition, the ITO coated glass substrate was patterned by photolithography. The procedure of photolithography is shown in Fig. 2-8:

1) The ITO coated substrates were cleaned in an ultrasonic bath with detergent, acetone, ethanol and deionized water for 10 minutes and dried with nitrogen gas.
2) The photoreactive polymer layer was deposited on top of the ITO by spin-coating (500 r/min for 3 s and 3000 r/min for 23 s). The substrate was then transferred to a hotplate and heated for 5 min at 110 ℃ to solidify the photoreactive layer.
3) The substrate was then ultraviolet (UV) irradiated through a photo mask. The irradiated part will then react with UV and ready to be removed by photographic developer.
4) The irradiated part of photoreactive layer was put into the developer and dissolved, followed by a rinse in deionized water for 25 s.
5) The substrate was then heated on a hot plate for another 5 min to remove the remained water and solidify the photoreactive layer again.
6) The substrate was dipped in an etching solution of 36 % HCl liquid to remove the undesired part of ITO.
7) In the end, after etching, the remaining photoreactive polymer layer was removed by ultrasonic bath with acetone for 10 min.

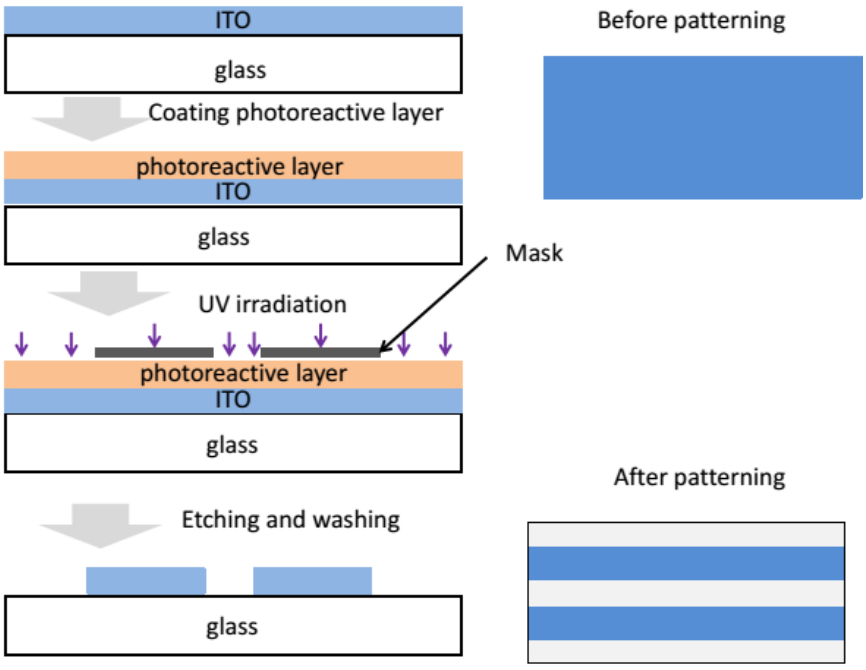

Fig. 2-8. Schematic illustration of photolithographic method used for ITO patterning.

After being ultrasonic cleaned in acetone, ethanol and deionized water, the pre-patterned ITO substrate will be loaded into the deposition chamber for the fabrication of the devices.

2.2.2 Fabrication of the devices

The OSCs are fabricated in a molecular beam epitaxy (MBE) vacuum chamber ($<4\times10^{-6}$ Pa) by thermally evaporating the subsequent layers. Fig. 2-9 displays the schematic of the MBE chamber as well as the conformation of a K-cell. It was equipped with 3 organic sources, 2 metal sources and 1 oxides source. Hence, it allows one to fabricate a completed device without breaking the vacuum. It can handle a substrate with 3.5×3.5 cm^2, consisting of 2 substrates, as shown in Fig. 2-10(b). The substrates were placed face down on the sample holder, which is rotated at a certain speed in order to assure the uniformity of the evaporated thin films. The deposition speed was monitored by a quartz crystal microbalance. The functional layers were then evaporated subsequently on the ITO substrate (see Fig. 2-10(a)). The structure of the device in this work is in a general anode/HTL/active layers/ETL/cathode sandwiched structure and this will be introduced in details separately in the following chapters.

As shown in figs. 2-10(b) and 2-10(c), each substrate contains 8 single solar cells, with a nominal area of 4 mm^2. After fabrication, they are taken out from the vacuum chamber for the further characterization without encapsulation. This area is defined as geometrical overlap between the pre-patterned ITO contact and the top Ag electrode. The definition of the active area via a geometrical overlap of the electrodes is difficult, since the active regions extend over the edges and contribute to the overall photocurrent by lateral currents from the surrounding absorber which is also illuminated. Therefore, using an aperture to define the exact illuminated area during measurement increases the accuracy. However, the application of an aperture will include the effect of a dark solar cell in parallel. For this reason, the aperture is only taken as area calibration while measuring the short circuit current.

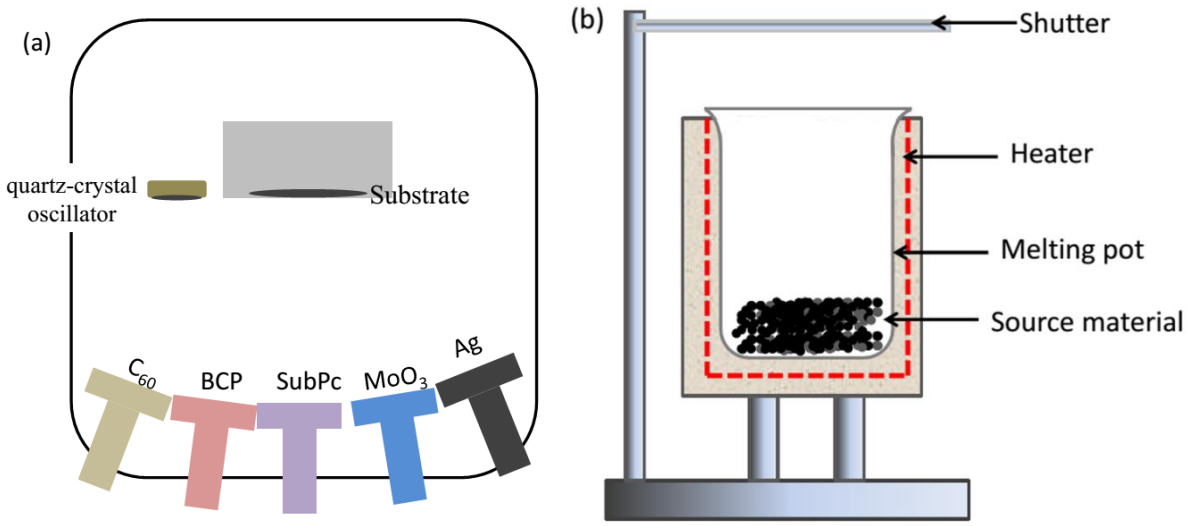

Fig. 2-9. Schematic of (a) MBE deposition chamber and (b) a Knudsen-cell (K-cell).

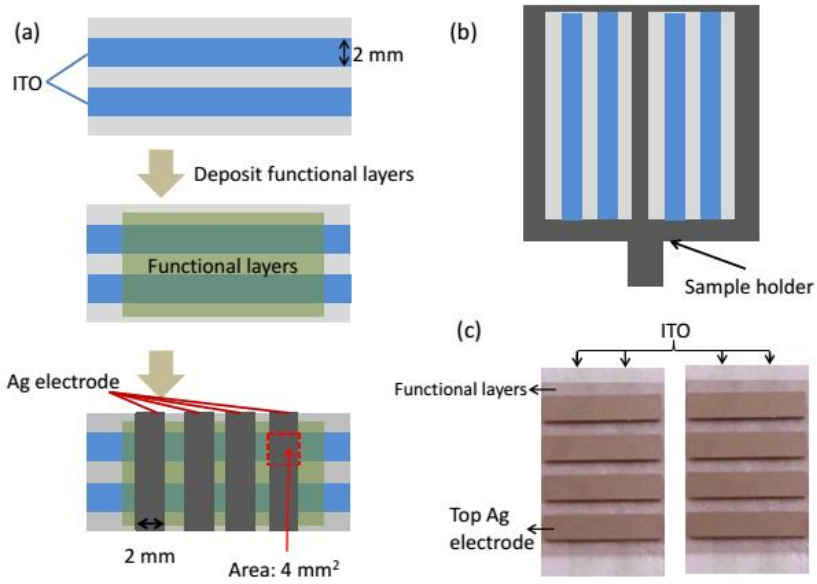

Fig. 2-10. (a) Fabrication procedure of the devices, (b) schematic of substrates loaded on the sample holder and (c) a photograph of as deposited devices (same batch). (Functional layers include: donor, acceptor, electron transport layer and hole transport layer)

2.3 Characterization methodes

2.3.1 Current density-voltage characteristics (*J-V* curve)

J-V curve is the most important characterization method for solar cells and ideally, it should be carried out under real solar illumination at a well-defined temperature. The standard condition for *J-V* measurement is the AM 1.5G spectrum (as shown in Fig. 2-11) and 25 ℃. In practical, the *J-V* characteristics are carried out under a simulated sunlight, which is generated by a light source, mostly a Xenon lamp with a specific gas mixture. In this work, the *J-V* curves are measured under a sun simulator whose light intensity was calibrated by a Si photodiode. A voltage sweep is applied and the current is recorded by a *J-V* source meter (Advantest R6245). The V_{OC}, J_{SC}, *FF* and *PCE* are then extracted.

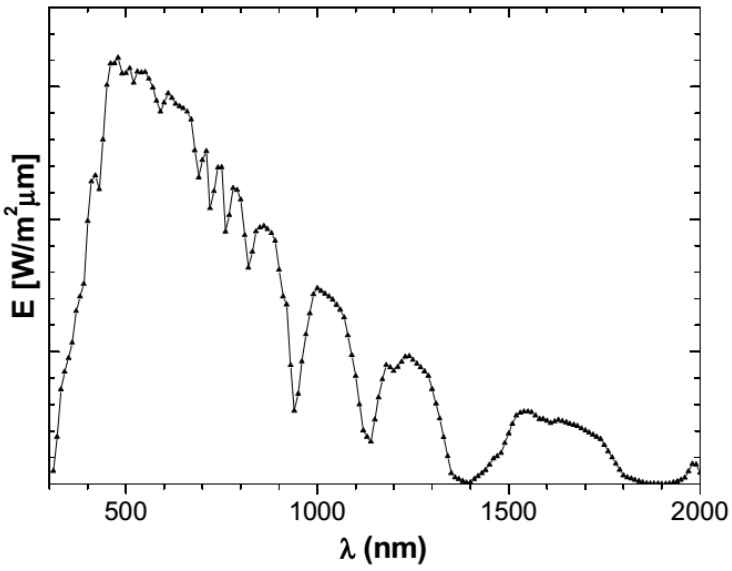

Fig. 2-11 The standard AM 1.5G solar irradiation spectrum (ASTMG 173).

2.3.2 External quantum efficiency (*EQE*)

The spectral photocurrent response describes the current density per unit wavelength and incoming intensity in the unit mA/(mW nm). Converting the incoming intensity into the number of photons and the current into the number of electrons, *EQE* can be obtained. In this work, we use a xenon light as the excitation source, which is dispersed through a monochromator (Bunko Keiki SM-1700A) and the current response of the device is detected by a lock-in amplifier. The lock-in technique increases the signal to noise ratio, as the lock-in amplifier only measures the signal at the chopping frequency. Consequently, parasitic signals and noise having another frequency are filtered out. The calibration of the setup is done by measuring a silicon reference cell that has a certain spectral response. The photocurrent data of the reference device are used to calculate the spectral intensity distribution which reaches the solar cell that is under measure. The system operation and the data extraction were finished by a PC with LabView program.

2.3.3 Transmittance and absorption

Ultraviolet-visible spectroscopy (UV-Vis) refers to absorption spectroscopy or reflectance spectroscopy in the ultraviolet-visible spectral region. The absorption or the reflectance in the visible range directly affects the perceived color of the chemicals involved and it is used to measure the transition from ground state to the excited state. Fig. 2-12 shows the schematic of a UV-Vis spectroscopy, which is composed of a light source, a diffraction grating in a monochromator to disperse the light and other parts. The transmittance is measured by comparing the light intensities before and after passing through a sample which is usually expressed as T%. The absorbance (*A*) is given by:

$$A = -log(T\%), \tag{2-1}$$

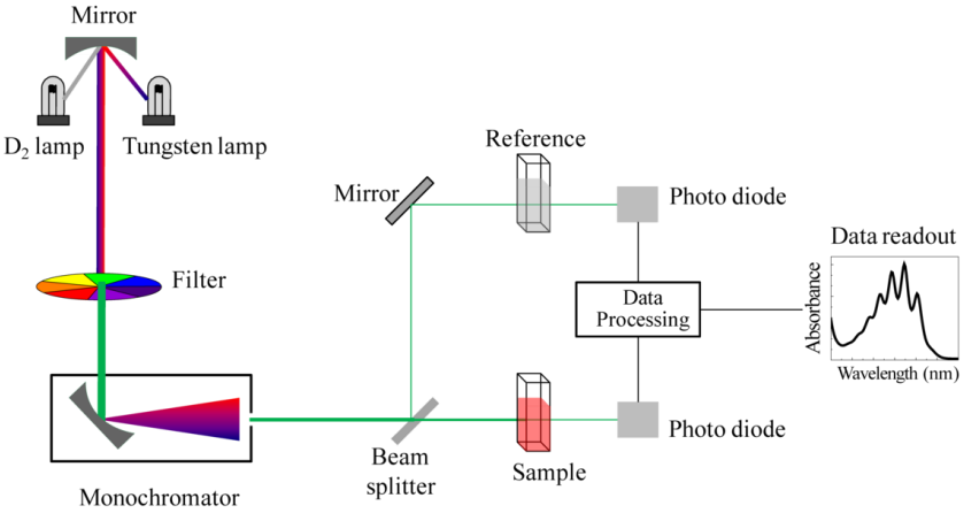

Fig. 2-12. The schematic of the setup for UV-Vis spectrophotometers, reprinted from *Ref.* [2-26].

2.3.4 Photoluminescence (PL)

The fluorescence for organic thin films was determined by photoluminescence (PL) in this work. The properties such as bandgap energy, electronic defects, recombination properties and so on can be studied by

PL spectrum. It is a measurement that reflects the transition from excited state to ground state: when incident photons with energy greater than the band-gap of the materials, they will be absorbed and create electronic excitations. The electronic excitations will eventually relax and transit from excited state to ground state. During this process, a photon with certain energy will be detected if radiative relaxation occurs. This emitted light is called photoluminescence, known as PL.

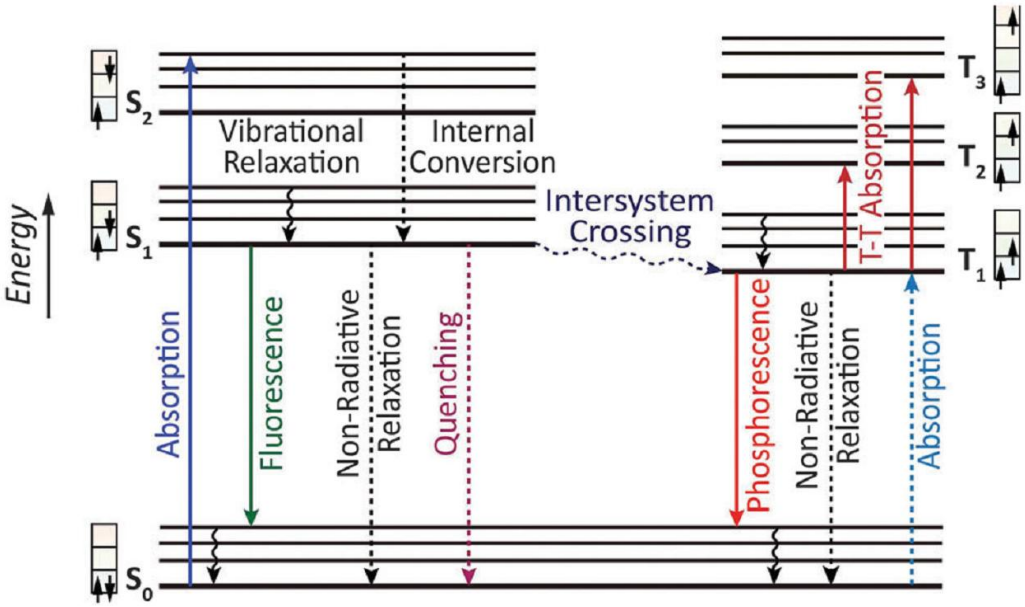

Fig. 2-13. Jablonski energy level diagram, reprinted from *Ref.* [2-27] showing principal luminescence processes in an organic molecule (left: singlet manifold, right: triplet manifold; the full arrows represent radiative process while dotted arrows for non-radiative process).

Fig. 2-13 shows the typical luminescence processes in the π-electronic system of organic molecules.[2-27] Luminescent emits light upon absorption of the light brought complexity in analyzing the PL signal and for this reason the PL measurement is always combined with the absorption spectra of a certain material. The absorption process often occurs primarily between the ground state S_0 and the singlet states S_1, S_2, *etc.*, which is governed by the quantum mechanical selection rule. The vibrational and rotational energy of the electronic levels geminated with one other is a set of sublevels. In principal, the fluorescence emission is mainly induced by the transition from the singlet state S_1 at the lowest excited level to the ground state, regardless of the initial state excited. This can be attributed to the rapid non-radiative process of internal energy conversion between higher excited states such as S_2, S_3… *etc.* and the lowest excited state S_1. In intersystem crossing from the singlet manifold to the triplet manifold and the reverse, non-radiative recombination can also be observed. Although these processes are forbidden by quantum mechanics, they will still occur only progress at a slower time scale than that of the singlet-singlet transitions.

Phosphorescence is defined as the radiative decay from the excited triplet state back to a singlet state.[2-28] For a certain molecule, because the triplet state exhibits a significant longer lifetime, the probability of non-radiative energy losses is much higher in the triplet state than in the singlet state. One of the abilities of the Phosphorescent molecules is to store light energy and release gradually. It is quite difficult for a pure organic compounds exhibiting phosphorescence at room temperature. When it notably that the phosphorescence may be enhanced by the addition of metal ions. The metal ions will promote intersystem crossing via spin-orbital coupling. Therefore, in the application of organic photovoltaics, the PL is always used to determine the excitons quenching for a certain molecule on exciton quenchers, the excitons quenching an organic-molecule interface is an energy loss path and to improve the performance of an organic

photovoltaic device, the excitons are expected to be vastly quenched at donor-acceptor interface or active-charge transporter interface.

2.3.5 Grazing incidence X-ray diffraction (GIXRD)

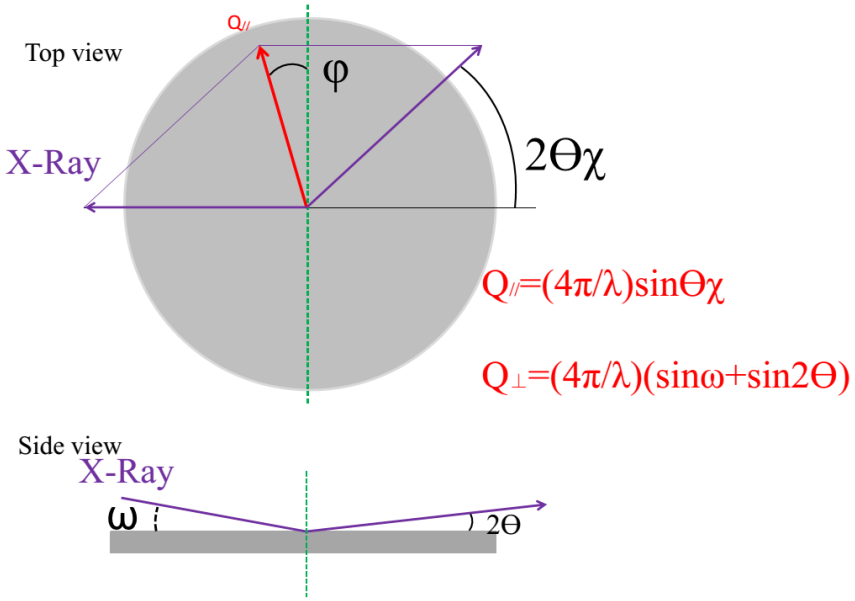

Fig. 2-14. Geometry of the GIXRD measurements and definition of the scattering vectors, $Q_{//}$ and $Q_{\perp}$.

Grazing incidence X-ray diffraction is typically from a crystalline structure uses small incident angles for the incoming X-ray so that make the surface sensitive. It can be used to measure the diffraction of surface or ultrathin layers because it offers a unique opportunity to study the diffraction from weakly scattering sample and the electric field at the critical angle is amplified locally by a factor of 4 and as a result, a stronger signal can be detected. The geometry of the GIXRD setup is shown in Fig. 2-14, describing the definition of vectors $Q_{//}$ and $Q_{\perp}$. The GIXRD combined with the traditional X-ray diffraction, will provide a three-dimensional structure and GIXRD is always used to observe the molecule orientation of organic materials. In this work, we utilized GIXRD to measure the molecule orientation of SubPc:C_{60} co-deposited bulk layers on different buffers.

2.3.6 Atomic force microscope (AFM)

The surface morphology of organic thin layers was investigated by using AFM, which is a high-resolution (on a scale of nanometer) scanning probe microscopy. An AFM is typically consisted of a cantilever, driven by a preamplifier; a tip, directly connected with the open end of the cantilever; a detector, detecting the deflection and motion of the cantilever; a sample stage with xyz-driver and a detector. The setup of a typical AFM is illustrated in Fig. 2-15. It should be noted that the deflection of the cantilever will be detected by the detector and converted into electrical signal. Therefore, the output of the detector is a time-dependent curve, with an intensity proportional to the cantilevers deviation. Basically, there are three contact modes in AFM measurement: contact mode, tapping mode and non-contact mode. Due to the tips dragging on the sample surface, the contours of the surface are measured either by the deflection of the cantilever directly or the feedback signal which keeps the tip at a constant position. In this work, the surface morphologies of the films were investigated in a tapping mode.

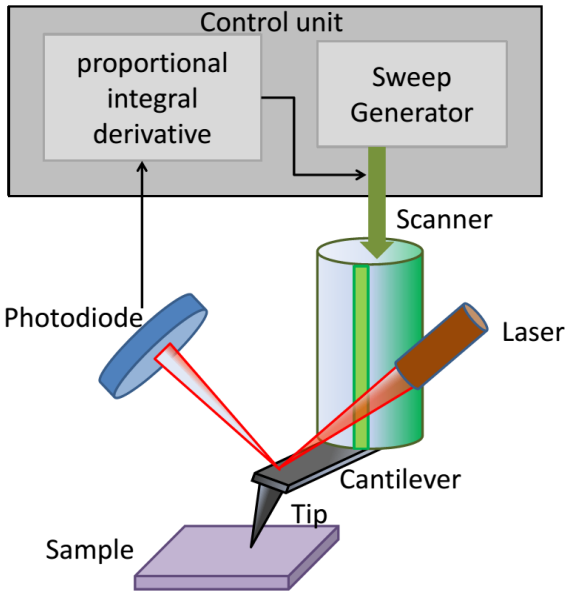

Fig. 2-15. Illustration of AFM system.

2.3.6 Transient measurements (transient photovoltage and transient photocurrent)

Interfacial charge separation and transportation is of great importance in organic photovoltaic devices. However, at present, much focus is given to the nature of charge separation and transportation though the examination of steady state characterizations. Transient technologies can provide direct information regarding the dynamics of charge behaviors such as trapping effect[2-29], transport[2-29~2-31] and recombination[2-32,2-33], *etc*. This section introduces the principles and characterization setups of transient measurements utilized in this work.

- Transient photovoltage (TPV)

When a semiconductor was excited by an above band-gap light, tightly bonded electron-hole pairs are generated near the surface region by inter-band transitions. The free carriers may then respond to the electric field existing within the surface barrier. Take InP semiconductor as an example, the electrons are drawn into the bulk region and the holes into the surface region due to the n-conducting type.

The hole current in the surface region may be become trapped or recombine with electrons. The trapped holes will deplete the surface charge and reduce the band bending. The corresponding reduction in the surface barrier allows an increase in an electron current into the semiconductor and an increased voltage. At the same time, due to the lowered barrier, the electrons from the bulk may also tunnel into the surface region, but at a lower probability. This reverse process will greatly increase the barrier and as a result, reduce the photovoltage.

The photovoltage would also be affected by other mechanisms. Under real operating conditions, electron and hole mobilities may be different in some semiconducting materials and therefore, even in a flat band initial configuration, a potential difference will be obtained between the surface and bulk regions of the material. As a result, the photovoltage will be modified a little and the deviation is called Dember potential (V_D), which was firstly published by Dember and can be described by:[2-34]

$$V_D = G_0 \frac{k_B T}{e} \frac{\mu_n - \mu_p}{n\mu_n + p\mu_p} \frac{1}{D/_L + S}, \quad (2\text{-}2)$$

where G_0 is the incident photon flux, k_B is Boltzmann's constant, T is temperature, μ_n and μ_p are the electron and hole mobilities, n and p are the electron and hole densities at equilibrium. D is the diffusion constant, L is the diffusion length and S is the surface recombination velocity. In an n-type semiconductor, one can take that $\mu_n >> \mu_p$, *also* $n >>$p. In this case, the maximum of this potential can be obtained when S=0.

$$V_D \cong G_0(k_B T/ne)\left(L/_D\right), \tag{2-3}$$

By using the reported values of L and D one can then estimate the maximum Dember potential.

The surface charge may be affected by direct exciting the electrons into or out of surface states. Especially in the sub-band-gap illumination, these processes are of greater significance. However, in general, for bulk materials, inter-band bulk transitions are dominant. Therefore, the surface state only affects the photovoltage at a quite limited range, at least, the eventual photovoltage.

To explore the transient properties of photovoltage for a certain semiconductor, one has to consider the photovoltaic behavior at short time range. Here we also take n-type semiconductor as example, the photogenerated holes are swept into the surface region where they deplete the surface charge and reduce the surface barrier. This process can be described as:

$$\frac{dn_h}{dt} = g - \frac{n_h}{\tau}\ , \tag{2-4}$$

where n_h is the excess hole concentration, g is the source term which shold be a function of light intensity and wavelength, and τ is the recombination time of holes with electrons at the surface. For small changes in the band bending the photovoltage should be proportional to the hole accumulation at the surface. The transit time for a photo-generated hole across the barrier is several orders of magnitude faster than the observed time constant. While in case of long term behavior, we must consider the slow process of minority electrons tunneling into the surface. Suppose the electrons are captured by traps and recombine with the trapped holes at a quite small direct recombination rate, which could account for the return to the illuminated photovoltage value of the surface barrier. Still in case of small band bending, the change in the barrier height δV_B, may be directly related to the accumulation of charge at the surface:

$$\delta V_B = \alpha\left(n_e - n_p\right), \tag{2-5}$$

where α is a proportionality constant depending on the temperature and material, [35, 36] and n_e and n_h are the excess electrons and holes densities at the surface. The rate of filling traps by electrons should be related to the barrier height by the following equation:

$$j_e = j_0 exp^{-\frac{e\delta V_B}{k_B T}} - 1, \tag{2-6}$$

In the limit that $e\delta V_B << k_B T$, we can get:

$$\frac{dn_e}{dt} = \frac{n_h - n_e}{\tau_B}, \tag{2-7}$$

where $\tau_B = k_B T/j_0 ae$. Combining Eq. 2-5 and Eq. 2-7 gives the expressions of photovoltage V_P:

$$V^P(t) = \begin{cases} V_{on}^P(I)\left[e^{-t/\tau_B} - e^{-t/\tau}\right], & 0 < t < t_{off}, \\ V_{t=t_{off}}^P + V_{off}^P(I)\left\{e^{\left[-(t-t_{off})/\tau\right]} - e^{\left[-(t-t_{off})/\tau_B\right]}\right\}, & t > t_{off}. \end{cases} \tag{2-8}$$

Then Eq. 2-8 is the primary principle prototype of the transient photovoltage measurement. According to it, for a semiconductor thin film, if light was incident on it, holes will accumulate at the surface which lower the barrier and increase the V^P signal. However, the lowered barrier allows electrons to migrate to the surface and fill traps which have a long recombination time with holes at the surface. Such absolute electron trap can also be investigated by the photoconductivity quenching. Before the barrier returning to its pre-illumination value, the filling of traps will not finish. And at the time light was turned off, the holes trapped at the surface recombine at a faster rate than the electrons. Thus the barrier height reverses in sign and becomes greater than its initial value. With the increase of the barrier height, electron traps are then emptied and the barrier returns to its equilibrium value. So the investigation of the turn-on and turn-off process can provide the charge trapping effects. And in case of organic materials, the dipole generation and interfacial effects can be similar with the band bending.

As for the recombination, based on the aforementioned Eq. 2-6, when saturation occurs, the generation rate of holes equals to the recombination rate of electrons with the trapped holes. For large band bending, the recombination current, j_e, is given by $j_e = j_0[exp(-e\delta V_B/k_BT) - 1]$, and the hole current by $j_h = gI$. Therefore, at steady state, j_h=j_e, then:

$$\delta V_B(I) = \frac{k_BT}{e} ln\left(\frac{gI}{j_0} + 1\right), \tag{2-9}$$

The vibration of the transient photovoltage, in a transient photovoltage (TPV) signal, at the turn-on and turn-off behavior, is therefore a reflection of recombination.

In case of OSCs, a much more simple model of TPV has been set up.[2-37,2-38] This model is based on the equivalent circuit of an OSC, as shown in Fig. 2-16. In a trap-limited device, the processes of charge trapping and detrapping can be assumed as charge and discharge of capacitors, since the defects acting as trap centers has the ability of storing the charges. In OSCs, the capacitance is a measure of the amount of charge that can be stored in the traps. The charge transport can be estimated by measuring the rise time of the TPV. The explanation is as followings. By comparing the rise time of the photovoltage to direct measurements of charge transport at open circuit condition, the relation between the voltage rise and charge transport can be monitored. This can be realized by using the cells with low RC time constants in which the current could then be measured across a wide voltage range. By doing so, we can measure the transport time of charges in this kind of cells. As compared with the transport time, the rise time of voltage is almost 1 order in magnitude faster. The donor/acceptor interface was replaced with a capacitor C_{active}, whose capacitance increases with voltage. The process of recombination is substituted with a resistor, which is dependent on the applied bias, R_{rec}. It should be noted that at the rise time of the voltage, the recombination is not occurred yet. The charge transport across the transport layers is represented as a resistor, R_{trans}, which is, on the contrary, decreased with the increasing bias. The interface of electrode/organic is represented by a second resistor, R_{rec} and a resistor $R_{electrode}$, which is a combination of organic layers and the lateral electrode. Under light irradiation and an applied bias of V_{OC}, there is a static charge on the capacitors while no current flow in the device. An additional pulsed light causes additional charge injection into the active layer, which is equivalent to adding extra charges to the C_{active}. This increases the voltage across C_{active}. As a result, some of these charges will move through R_{trans} to $C_{ITO/organic}$. The measured voltage gives a rise time which is expressed by:

$$\tau_{rise} = R_{trans} \times C_{ITO/organic} \tag{2-10}$$

When the device is held at a potential that quite close to V_{OC}, the same amount of charges will emerged on the capacitors. Also, under same extra pulsed light excitation, if $R_{electrode}$<R_{trans}, the transport across the ITO/organic interface will become the limiting factor in the process of discharge. The time constant of the current is given by:

$$\tau_{trans} = R_{trans} \times C_{active} \quad (2\text{-}11)$$

Therefore, the slight rearrangement of Eq. 2-10 and Eq. 2-11 will give:

$$\tau_{trans} = \tau_{rise} \times C_{active}/C_{ITO/organic} \quad (2\text{-}12)$$

From this simple model, we can then directly get the information of charge transport by measuring the TPV of the devices, especially for the rise time. Briefly speaking, the simple model suggests that in a device with lower trap densities at the ITO/organic interface, which means a lower $C_{ITO/organic}$, a shorter rise time is expected. Therefore, the longer rise time is an evidence of charge trapping.

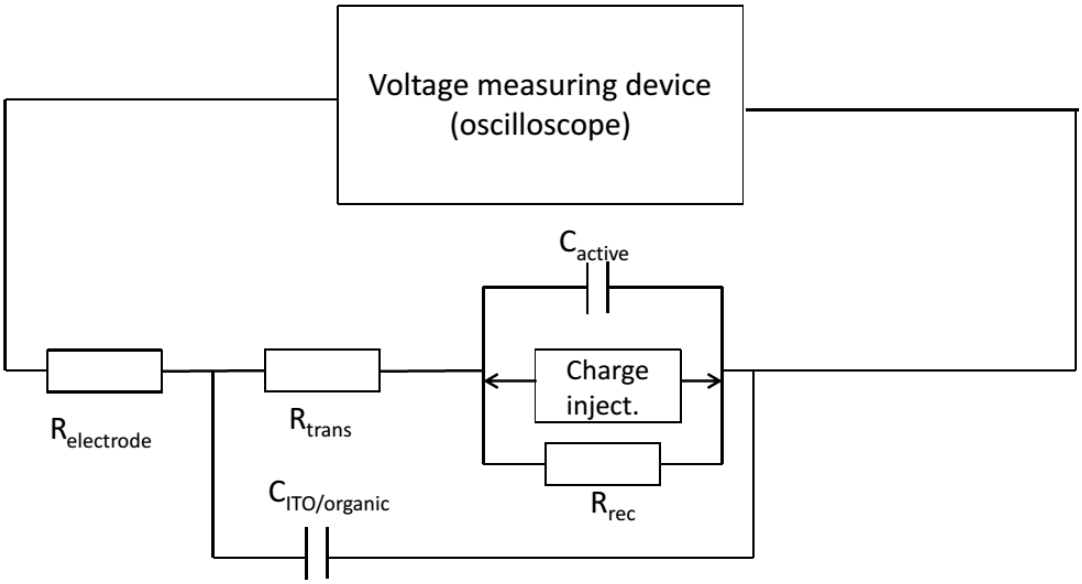

Fig. 2-16 The equivalent circuit of an OSC.

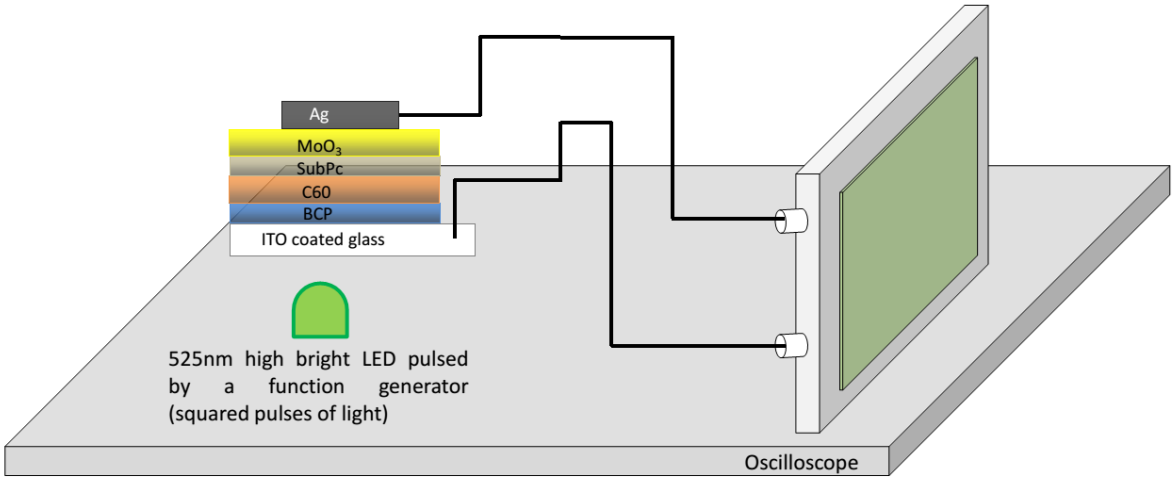

Fig. 2-17. Experimental set-up of transient photovoltage (TPV) measurement.

The setup of the TPV measurement is shown in Fig. 2-17. The TPV measurement was performed using a pulse generator (Agilent 33220A) driving a high intensity light-emitting diode (Kingbright L-7104VGC-H, peak emission wavelength of 525 nm, 35 nm full width at half maximum) with pulse durations of several 100 μs. The light intensity was varied by adjusting the applied voltage and calibrated by an optical power meter (THORLABS PM 100D). The TPV signal was recorded by an oscilloscope (Agilent DSO-X-2024) with the input impendence of 1 MΩ.

- Transient photocurrent (TPC)

The photocurrent behavior was controlled by carrier localization and delocalization process in an organic semiconductor. The following equations described the charge carrier kinetics under condition of uniform charge generation and trapping:[2-39,2-40]

$$\frac{dp(t)}{dt} = g - \left({}^{1}/_{\tau_R}\right)P_C(t) - RP_C(t)p(t), \tag{2-13}$$

$$\frac{\partial\rho(t,\xi)}{\partial t} = \left(\frac{1}{\tau_0}\right)\left[\left({}^{1}/_{\xi_0}\right)exp\left(-{}^{\xi}/_{\xi_0}\right) - \left({}^{1}/_{N_t}\right)\rho(t,\xi)\right]P_C(t) - \left({}^{1}/_{\tau_0}\right)\left({}^{N_c}/_{N_t}\right)\times exp\left({}^{-\xi}/_{k_BT}\right)\rho(t,\xi), \tag{2-14}$$

$$P_t = P_C(t) + \int_0^\infty d\xi\rho(t,\xi), \qquad p(0) = 0, \tag{2-15}$$

where p is the total carrier density, P_C the delocalized carrier density, ξ the energy of a localzied state, $\rho d\xi$ the density of carrier localzied in states with energies from ξ to $\xi+d\xi$, g the generation rate, τ_R the characteristic time of monomolecular recombination, R the bimolecular recombination constant, τ_0 the lifetime of a delocalzied carrier respective to trapping, N_t the total density of localized states, N_c the density of conductive states, ξ_0 the characteristic energy of the localized state distribution, T temperature and k_B Boltzmann constant.

The time dependent transient photocurrent was governed by the delocalzied carriers density $p_c(t)$ is quite sensitive to the level of the generation rate g. under high generation rates $g>g_*$,

$$g_* = \left({}^{1}/_{2}\right)\left({}^{N_c}/_{N_t}\right)\left({}^{\tau_0}/_{\tau_R}\right)^{1/\alpha}\left({}^{1}/_{R\tau_0\tau_R}\right), \tag{2-16}$$

In this case, recombination is completely determined by bimolecualr recombination mechanism and if $0 \leqslant t < t_*$,

$$t_* = \tau_0\left({}^{N_t}/_{N_c}\right)^{\alpha/(1+\alpha)}\left(gR\tau_0^2\right)^{-1/(1+\alpha)}, \tag{2-17}$$

the photocurrent rises by power law

$$p_c(t) = g\tau_0\left({}^{N_c}/_{N_t}\right)^{\alpha}\left({}^{t}/_{\tau_0}\right)^{\alpha}, \tag{2-18}$$

and at $t=t_*$, passes through the maximum

$$\mathrm{p_c^{(*)} = p_c(t) = g\tau_0\left({}^{N_c}/_{N_t}\right)^{\alpha/(1+\alpha)}\left(gR\tau_0\right)^{-\alpha/(1+\alpha)}}, \tag{2-19}$$

Further, at the time range of $t_* < t < t_{st}$, where

$$t_{st} = \tau_0\left({}^{N_c}/_{N_t}\right)^{\alpha/(1+\alpha)}\left({}^{RN_t^2}/_{g}\right)^{1/(1+\alpha)}, \tag{2-20}$$

the photocurrent will then decay by:

$$p_c(t) = \left({}^{g}/_{R}\right)^{1/2}\left({}^{N_c}/_{N_t}\right)^{\alpha/2}\left({}^{t}/_{\tau_0}\right)^{-(1-\alpha)/2}, \tag{2-21}$$

then reach the steady state value:

$$p_c^{(st)} = N_c\left({}^{g}/_{RN_cN_t}\right)^{1/(1+\alpha)}. \tag{2-22}$$

At very low generation rate, that is $g < g_0$, where

$$g_0 = 2^{-1/\alpha}\left(N_c/\tau_R\right)(RN_t\tau_R)^{-1/\alpha}, \tag{2-23}$$

the photocurrent is completely provided by the monomolecular recombination mechanism, and in the time range of $0 \leq t < t_m$, in which

$$t_m = \tau_0\left(N_t/N_c\right)\left(\tau_R/\tau_0\right)^{1/\alpha}, \tag{2-24}$$

it incerases by power law Eq. 2-16 until $t=t_m$ the photocurrent reaches a steady state value of

$$p_c^m = g\tau_R. \tag{2-25}$$

while for intermediate generation rages $g_0 < g < g_*$, at the time range of $0 < t < t_b$, where

$$t_b = 2^{-1/(1-\alpha)}\tau_0\left(N_t/N_c\right)^{\alpha/(1+\alpha)}\left(gR\tau_R^2\right)^{-1/(1-\alpha)}. \tag{2-26}$$

From Eq. 2-26, one can tell that monomolecualr recombination dominates and at the range of $t < t_b$.

Based on these calculations, one can tell that in case of a material with less trap density, the photocurrent will not obviously affected by the time and only shows a dielectronic feed back with the incident pulse excitation. Also, in case of rapid charge transportation and limited recombination, the photocurrent will change along with the time with the absent peak photocurrent. Based on this basic theory, a model that describes the current flow in the organic photovoltaic devices was set up by using the one-dimensional drift-difusion eqation[2-41~2-43]. It has been successfully used to model the steady-state properties of bilayer[2-44] and bulk[2-45] OSCs. They proposed that if the nanostructure of the active layer is ignored, the device can then be modeled by an effective medium approach with the mobilities of μ_n (for electrons) and μ_p (for holes). They seperately represent the transport of the respective carrier thtough the acceptor and donor in the z direction. The electron, hole and charge pairs are defined by n, p and X. Then the equations are:

$$\frac{\partial n}{\partial t} = \frac{\partial}{\partial z}\left[-\mu_n k_B T\frac{\partial n}{\partial z} - u_n neE\right] + k_{diss}(E)X - \gamma np, \tag{2-27}$$

$$\frac{\partial p}{\partial t} = \frac{\partial}{\partial z}\left[-\mu_p k_B T\frac{\partial p}{\partial z} - u_p peE\right] + k_{diss}(E)X - \gamma np, \tag{2-28}$$

$$\frac{\partial X}{\partial t} = G - k_{rec}X - k_{diss}(E)X - \gamma np, \tag{2-29}$$

$$\frac{\partial E}{\partial z} = \frac{e(p-n)}{\varepsilon_0\varepsilon_r}, \tag{2-30}$$

here e is the elementary charge, ε_0 the permittivity of free space, ε_r the relative permittivity of the organic material; t stands for time and T represents the absolute temperature while k_B is the Boltzmann constant.Eqs. 2-27 and 2-28 represent the coupled drift-diffusion equations for electrons and holes, with a free carrier generation rate constant of k_{diss}, the bimolecular recombination of electrons and holes with a constant rate of γ. Eq. 2-29 describes the dynamics or charge paris which undergo monomolecular recombination with a rate constant k_{rec} and are generated with rate G and Eq. 2-30 represents the change in field inside the device due to the change of space charge. The generation rate G is supposed to be directly proportional to the light intensity linearly.

They assumed the bondary conditions by thermionic injection in the presence of image charge effect with barriers between electrode and the organic layer of 0.5 eV. The voltage across the active layer is 0.5 V, and for simplicity electron and hole mobilities were regarded as 2×10^{-4} $cm^2v^{-1}s^{-1}$. Plus an uniform generation rate of G and a Langevin-like recombination. The equations can be solved and photocurrent can be given by:

$$J = \left(-\mu_n \frac{\partial n}{\partial z} - \mu_p \frac{\partial p}{\partial z}\right) k_B T - (\mu_n n + \mu_p p) eE. \tag{2-31}$$

This photocurrent will then be recorded at each step.

This model was then further developed by separating the total density of electrons n into free (n_f) and trapped (n_t) electron concentrations. Then:

$$\frac{\partial n_f}{\partial t} = \frac{1}{e}\frac{\partial y}{\partial z}\left[\mu_n k_B T \frac{\partial n_f}{\partial z} + \mu_n n_f eE\right] + \left(k_{diss} X - \gamma n_f p\right) - \frac{\partial n_t}{\partial t}, \tag{2-32}$$

$$\frac{\partial n_t}{\partial t} = C_t (N_t - n_t) n_f - C_{dt} n_t, \tag{2-33}$$

$$\frac{\partial p}{\partial t} = \frac{1}{e}\frac{\partial y}{\partial z}\left[\mu_p k_B T \frac{\partial p}{\partial z} - \mu_p peE\right] + \left(k_{diss} X - \gamma n_f p\right), \tag{2-34}$$

$$\mu_{n(p)} = \mu_{n0(p0)} exp\left(\gamma_{n(p)} \sqrt{|E|}\right), \tag{2-35}$$

$$n = n_f + n_t, \tag{2-36}$$

$$\frac{\partial E}{\partial z} = \frac{e(p-n)}{\varepsilon_0 \varepsilon_r}, \tag{2-37}$$

$$\frac{\partial X}{\partial t} = I G_0(z) - k_{rec} X - k_{diss}(z, E, T) X + \gamma n_f p, \tag{2-38}$$

$$k_{diss}(z, E, T) = \frac{3\gamma}{4\pi\alpha^3} \exp\left(-\frac{\mathrm{E_B}}{\mathrm{k_B T}}\right) \frac{\mathrm{J_1} 2\sqrt{-2\mathrm{b}}}{\sqrt{-2\mathrm{b}}}, \tag{2-39}$$

$$b = \frac{e^3 |E|}{8\pi\varepsilon_0 \varepsilon_r k_B^2 T^2}, \tag{2-40}$$

here E_B is the binding energy of the charge pairs. Eqs. 2-32 and 2-34 represent the coupled drift-diffusion equations for free electrons and holes. Eq. 2-33 is the trapping and detrapping dynamics of free charges in which C_t is tha trapping rate constant. And in this model, the photocurrent is given by:

$$J = \left(\mu_n \frac{\partial n_f}{\partial z} - \mu_p \frac{\partial p}{\partial z}\right) k_B T + (\mu_n n_f + \mu_p p) eE, \tag{2-41}$$

Consiering the role of charge pair separation and recombination, they then induced an important parameter of charge generation efficiency P, ginven by the Onsager-Braun model:

$$P = \frac{k_{diss}(E)}{[k_{diss}(E) + k_{rec}]} = \frac{1}{1 + \frac{k_{rec}}{k_{diss(E)}}}, \tag{2-42}$$

The energy loss caused by the recombination will bring about the charge generation and exction separation. By importing a parameter of P^{av}, which is calculated by intergrating the charge generation efficiency across the device, the total reduction in the separation efficiency can be expressed:

$$P^{av} = \frac{\int_0^d G_z \frac{k_{diss}(z,E) X - \gamma n_f p}{k_{diss}(z,E) X - \gamma n_f p + k_{rec} X} dz}{\int_0^d G_z(z) dz}. \tag{2-43}$$

This equation suggests that the suppression of charge generation and the recombination , caused by the space charge effects mediated by charge trapping, play a role in producing a peak in the photocurrent trasients. Also the space charge effecs and recombination will lead to a reduction in the photocurrent generation efficiency.

The experimental setup for TPC is shown in Fig. 2-18. The setup of TPC is almost the same as that of the TPV. In the TPC measurement, the device was excited by the pulsed green LED and was connected in

series with a 50 Ω resistance. An oscilloscope set to high impendence input (1 MΩ) was used to record the voltage drop across the resistance, so that the photocurrent could be calculated.

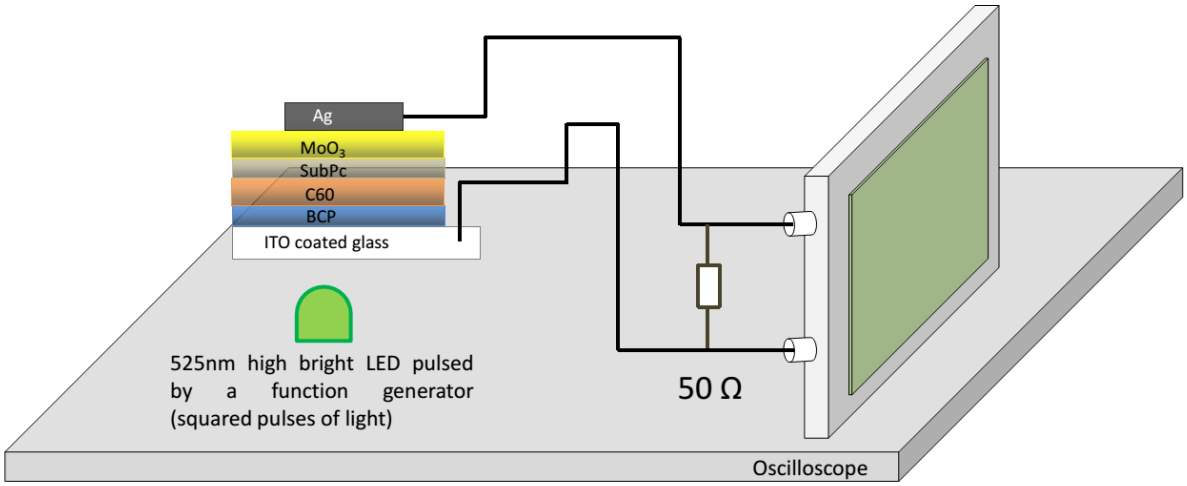

Fig. 2-18. The experimental setup of TPC measurement.

Due to the sensitivity of transient signals to the excitation time, the incident light source is required to have relatively short rise and fall times to eliminate the measurement errors. The rise and fall time of the high bright LED was measured by a Si biased photo detector (THORLABS DET10A/M) and Fig. 2-19 shows the result. The black curve shows the output of the driving pulse while the green one is the transient photovoltage signal collected by the detector, with a pulse width of 500 ns. From the TPV signal we can easily tell that the rise and fall time is less than 100 ns and the response on this scale will not affect the intrinsic TPV/TPC signal of the devices.

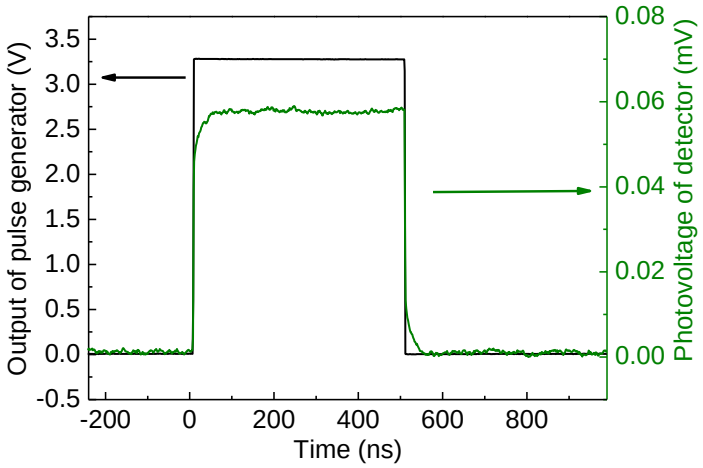

Fig. 2-19. The photovoltage of Si biased photo detector as compared with the pulsed power.

References

[2-1] R.R. Lunt, J.B. Benziger, S.R. Forrest. Relationship between Crystalline Order and Exciton Diffusion Length in Molecular Organic Semiconductors. Advanced Materials, **22** (2010) 1233.

[2-2] T.B. Singh, N. Sariciftci, H. Yang, L. Yang, B. Plochberger, H. Sitter. Correlation of Crystalline and Structural Properties of C_{60} Thin Films Grown at Various Temperature with Charge Carrier Mobility. Applied Physics Letters, **90** (2007) 213512.

[2-3] D. Kurrle, J. Pflaum. Exciton Diffusion Length in the Organic Semiconductor Diindenoperylene. Applied Physics Letters, **92** (2008) 133306.

[2-4] M-S. Liao, S. Scheiner. Electronic Structure and Bonding in Metal Phthalocyanines, Metal=Fe, Co, Ni, Cu, Zn, Mg. The Journal of Chemical Physics, **114** (2001) 9780.

[2-5] B.P. Rand, J. Xue, F. Yang, S.R. Forrest. Organic Solar Cells with Sensitivity Extending Into the Near Infrared. Applied Physics Letters, **87** (2005) 233508.

[2-6] R.F. Bailey-Salzman, B.P. Rand, S.R. Forrest. Near-Infrared Sensitive Small Molecule Organic Photovoltaic Cells Based on Chloroaluminum Phthalocyanine. Applied Physics Letters, **91** (2007) 013508.

[2-7] J.Y. Kim, S. Noh, Y.M. Nam, J.Y. Kim, J. Roh, M. Park, J.J. Amsden, D.Y. Yoon, C. Lee, W.H. Jo. Effect of Nanoscale SubPc Interfacial Layer on the Performance of Inverted Polymer Solar Cells Based on P3HT/PC_{70}BM. ACS Applied Materials & Interfaces, **3** (2011) 4279.

[2-8] J. Kim, S. Yim. Influence of Surface Morphology Evolution of SubPc Layers on the Performance of SubPc/C_{60} Organic Photovoltaic Cells. Applied Physics Letters, **99** (2011) 193303.

[2-9] C.G. Claessens, T. Torres. Synthesis, Separation, and Characterization of the Topoisomers of Fused Bicyclic Subphthalocyanine Dimers. Angewandte Chemie International Edition, **41** (2002) 2561.

[2-10] N. Li, B.E. Lassiter, R.R. Lunt, G. Wei, S.R. Forrest. Open Circuit Voltage Enhancement Due to Reduced Dark Current in Small Molecule Photovoltaic Cells. Applied Physics Letters, **94** (2009) 023307.

[2-11] H. Gommans, D. Cheyns, T. Aernouts, C. Girotto, J. Poortmans, P. Heremans. Electro-Optical Study of Subphthalocyanine in a Bilayer Organic Solar Cell. Advanced Functional Materials, **17** (2007) 2653.

[2-12] T.B. Singh, N. Marjanović, G. Matt, S. Günes, N. Sariciftci, A.M. Ramil, A. Andreev, H. Sitter, R. Schwödiauer, S. Bauer. High-Mobility N-Channel Organic Field-Effect Transistors Based on Epitaxially Grown C_{60} Films. Organic Electronics, **6** (2005) 105.

[2-13] J.S. Park, B.R. Lee, J.M. Lee, J.-S. Kim, S.O. Kim, M.H. Song. Efficient Hybrid Organic-Inorganic Light Emitting Diodes with Self-Assembled Dipole Molecule Deposited Metal Oxides. Applied Physics Letters, **96** (2010) 243306.

[2-14] H. You, Y. Dai, Z. Zhang, D. Ma. Improved Performances of Organic Light-Emitting Diodes with Metal Oxide as Anode Buffer. Journal of Applied Physics, **101** (2007) 026105.

[2-15] C-W. Chu, S-H. Li, C-W. Chen, V. Shrotriya, Y. Yang. High-Performance Organic Thin-Film Transistors with Metal Oxide/Metal Bilayer Electrode. Applied Physics Letters, **87** (2005) 193508.

[2-16] D.Y. Kim, J. Subbiah, G. Sarasqueta, F. So, H. Ding, Y. Gao. The Effect of Molybdenum Oxide Interlayer on Organic Photovoltaic Cells. Applied Physics Letters, **95** (2009) 093304.

[2-17] H. Ding, Y. Gao, C. Small, D.Y. Kim, J. Subbiah, F. So. Energy Level Evolution of Air and Oxygen Exposed Molybdenum Trioxide Films. Applied Physics Letters, **96** (2010) 243307.

[2-18] S. Cho, L. Piper, A. DeMasi, A. Preston, K. Smith, K. Chauhan, R.A. Hatton, T.S. Jones. Soft X-Ray

Spectroscopy of C_{60}/Copper Phthalocyanine/MoO_3 Interfaces: Role of Reduced MoO_3 on Energetic Band Alignment and Improved Performance. The Journal of Physical Chemistry C, **114** (2010) 18252.

[2-19] K. Kanai, K. Koizumi, S. Ouchi, Y. Tsukamoto, K. Sakanoue, Y. Ouchi, K. Seki. Electronic Structure of Anode Interface with Molybdenum Oxide Buffer Layer. Organic Electronics, **11** (2010) 188.

[2-20] L. Nazar, Z. Zhang, D. Zinkweg. Insertion of Poly (P-Phenylenevinylene) in Layered MoO_3. Journal of the American Chemical Society, **114** (1992) 6239.

[2-21] Y. Kinoshita, R. Takenaka, H. Murata. Independent Control of Open-Circuit Voltage of Organic Solar Cells by Changing Film Thickness of MoO_3 Buffer Layer. Applied Physics Letters, **92** (2008) 243309.

[2-22] K. Probst, N. Karl. Energy Levels of Electron and Hole Traps in the Band Gap of Doped Anthracene Crystals. Physica Status Solidi (a), **27** (1975) 499.

[2-23] T. Connolly. Organic Semiconductors, Semiconductors, Springer. (1972) 175.

[2-24] W. Warta, R. Stehle, N. Karl. Ultrapure, High Mobility Organic Photoconductors. Applied Physics A, **36** (1985) 163.

[2-25] N. Karl, J. Marktanner, R. Stehle, W. Warta. High-Field Saturation of Charge Carrier Drift Velocities in Ultrapurified Organic Photoconductors. Synthetic Metals, **42** (1991) 2473.

[2-26] Http://En.Wikipedia.Org/Wiki/Ultraviolet%E2%80%93visible_Spectroscopy

[2-27] M. Orchin, H.H. Jaffé, Symmetry, Orbitals, and Spectra (Sos), Wiley-Interscience New York. (1971).

[2-28] H. Xu, R. Chen, Q. Sun, W. Lai, Q. Su, W. Huang, X. Liu. Recent Progress in Metal-Organic Complexes for Optoelectronic Applications. Chemical Society Reviews, **43** (2014) 3259.

[2-29] B.C. O'Regan, F. Lenzmann. Charge Transport and Recombination in a Nanoscale Interpenetrating Network of N-Type and P-Type Semiconductors: Transient Photocurrent and Photovoltage Studies of TiO_2/Dye/CuSCN Photovoltaic Cells. The Journal of Physical Chemistry B, **108** (2004) 4342.

[2-30] J. Noolandi. Multiple-Trapping Model of Anomalous Transit-Time Dispersion in a-Se. Physical Review B, **16** (1977) 4466.

[2-31] R. Brüggemann. Analysis of the Photoconductive Decay from a Trapping Perspective. Solid State Communications, **101** (1997) 199.

[2-32] J. Nelson. Diffusion-Limited Recombination in Polymer-Fullerene Blends and Its Influence on Photocurrent Collection. Physical Review B, **67** (2003) 155209.

[2-33] J.G. Müller, J.M. Lupton, J. Feldmann, U. Lemmer, M.C. Scharber, N.S. Sariciftci, C.J. Brabec, U. Scherf. Ultrafast Dynamics of Charge Carrier Photogeneration and Geminate Recombination in Conjugated Polymer: Fullerene Solar Cells. Physical Review B, **72** (2005) 195208.

[2-34] S.M. Sze, K.K. Ng, Physics of Semiconductor Devices, John Wiley & Sons. (2006)

[2-35] J. Łagowski, C. Balestra, H. Gatos. Electronic Characteristics of "Real" CdS Surfaces. Surface Science, **29** (1972) 213.

[2-36] J. Łagowski, C.L. Balestra, H.C. Gatos. Photovoltage Inversion Effect and Its Application to Semiconductor Surface Studies: CdS. Surface Science, **27** (1971) 547.

[2-37] H. Scher, E.W. Montroll. Anomalous Transit-Time Dispersion in Amorphous Solids. Physical Review B, **12** (1975) 2455.

[2-38] B.C. O'Regan, K. Bakker, J. Kroeze, H. Smit, P. Sommeling, J.R. Durrant. Measuring Charge Transport from Transient Photovoltage Rise Times: A New Tool to Investigate Electron Transport in Nanoparticle Films. The Journal of Physical Chemistry B, **110** (2006) 17155.

[2-39] H. Scher, E.W. Montroll. Anomalous Transit-Time Dispersion in Amorphous Solids. Physical Review B, **12** (1975) 2455.

[2-40] A. Andriesh, V. Arkhipov, M. Iovu, A. Rudenko, S. Shutov. Anomalous Transient Photocurrent in Disordered Semiconductors: Theory and Experiment. Solid State Communications, **48** (1983) 1041.

[2-41] L. Hsiao, K. Zhang. The Relaxation of the Hydrodynamic Model for Semiconductors to the Drift-Diffusion Equations. Journal of Differential Equations, **165** (2000) 315.

[2-42] R. Jordan, D. Kinderlehrer, F. Otto. The Variational Formulation of the Fokker-Planck Equation. SIAM journal on mathematical analysis, **29** (1998) 1.

[2-43] I. Hwang, N. Greenham. Modeling Photocurrent Transients in Organic Solar Cells. Nanotechnology, **19** (2008) 424012.

[2-44] J. Barker, C. Ramsdale, N. Greenham. Modeling the Current-Voltage Characteristics of Bilayer Polymer Photovoltaic Devices. Physical Review B, **67** (2003) 075205.

[2-45] I. Hwang, C.R. McNeill, N.C. Greenham. Drift-Diffusion Modeling of Photocurrent Transients in Bulk Heterojunction Solar Cells. Journal of Applied Physics, **106** (2009) 094506.

Chapter 3 Study on the Performance Improvement in Inverted Bilayer Devices

In this chapter, we mainly discussed the effect of BCP buffer layer in SubPc/C_{60} based small molecule bilayer device. We also attempted to optimize the device performance by further modifying the ITO cathode.

3.1 Introduction

Although great progress in the *PCE* of small molecule OSCs has been achieved in recent years,[3-1~3-3] the device lifetime is short for the conventional OSCs and the possible reasons might be the oxidation of cathode with low work function,[3-4,3-5] the degradation of organic materials[3-6,3-7] and the interfacial instabilities.[3-8,3-9] One feasible approach to the instable issues of the conventional devices is to construct an inverted structure in which the ambient or illumination sensitive organic materials could be well protected and as a result, extend the device lifetime.

The utilization of appropriate buffer layers between electrodes and active layer is quite common in conventional devices and the improvement in the device performance were vastly observed.[3-10,3-11] Bathocuproine ($C_{26}H_{20}N_2$, BCP) is widely used in conventional devices to optimize the device performance by establishing an ohmic contact between C_{60} and metal, eliminating the metal induced charge transfer states, preventing the dipole formation and so on.[3-12,3-13] In our previous work, we have clarified the electronic properties of BCP/metal interface.[3-14~3-16] Also the possibility to incorporate it into an inverted device is proved.[3-17] However, the function of BCP in an inverted OSC is still not yet fully understood.

We fabricated inverted OSCs without/with BCP layer incorporated between indium-tin-oxide (ITO) and C_{60} to clarify the effect of the BCP buffer in an inverted device. A significant improvement of device performance in device with BCP was witnessed. The photoluminescence (PL), the transient photovoltage (TPV), and the transient photocurrent (TPC) measurements were carried out to reveal the reason of this efficiency improvement and to clarify the role of BCP in the inverted OSCs. At the end of this chapter, we discussed the effect of interfacial modification in the BCP device by using light intensity dependent *J-V* measurement and revealed the reason of the further improvement in device performance.

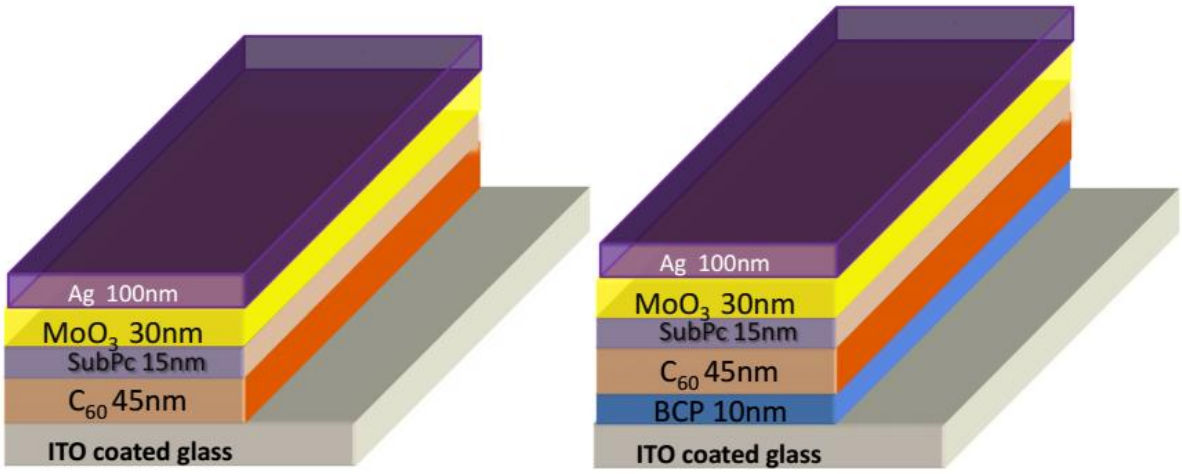

Fig. 3-1. Structures of inverted devices without (left) and with (right) BCP buffer layer.

3.2 Experimental methods

3.2.1 Device fabrication

The OSCs used in this study were based on hetero-junction of boron subthalocyanine chloride (SubPc)/ C_{60}, where SubPc acts as donor and C_{60} acts as acceptor.[3-18,3-19] As shown in Fig. 3-1, devices were fabricated with a structure of ITO (150 nm) coated glass/without or with BCP (10 nm)/C_{60} (45 nm)/SubPc (15 nm)/MoO_3 (30 nm)/Ag (100 nm). The effective area is 4 mm^2, as defined by overlapping of vertical ITO strip and horizontal Ag layer. The devices were fabricated by thermally evaporating the subsequent layers in a vacuum ($\leqslant 4\times10^{-6}$ Pa) chamber. The BCP, SubPc and C_{60} were purchased from Aldrich and purified by vacuum gradient sublimation for 3 times to remove impurities. The deposition rates for organic layers are 0.5 Å/s and that for MoO_3 and Ag are 1 Å/s, as monitored by a quartz crystal microbalance. After fabrication, the unencapsulated devices were characterized under an air ambient condition at room temperature.

3.2.2 Characterization methods

The steady-state characteristics were examined by measuring the current density-voltage (*J-V*) curve and external quantum efficiency (*EQE*). The *J-V* characteristics were carried out with the Advantest R6245 under dark and constant illumination with a light intensity of 1000 W/m^2 at AM 1.5 G spectrum. In order to test the solar cells under various light intensities, the intensity of the light was adjusted by a series of two neutral density filters wheels of six filters apiece. The intensity of light transmittance through the filter was independently measured via an optical power meter (THORLABS, PM 100D). The *EQE* spectra were measured by using a lock-in technique under a xenon light illumination dispersed through a monochromator (Bunko Keiki SM-1700A). The PL spectra were recorded by a CCD spectrophotometer by using a 532 laser as excitation source and the laser power is 10 mW. The TPV measurements were performed by using a high brightness 525 nm light-emitting diode (Kingbright L-7104VGC-H) driven by a pulse generator (Agilent 33220A) to generate a square-pulse optical excitation. The frequency of 1 kHz and pulse width of 500 μs were chosen. The light intensity, calibrated by an optical power meter (THORLABS PM 100D), was varied by adjusting the applied voltage. A digital oscilloscope (Agilent DSO-X-2024) with an input impendence of 1 MΩ was used to record the transient voltage. The TPC measurements were performed using a similar setup as for the TPV by measuring the voltage drop across a 50 Ω resistor in series with the devices.

3.3 Results and discussion

3.3.1 Steady state characteristics

- *J-V* curves

Fig. 3-2 depicts the illuminated *J-V* curves of both the devices without and with BCP layer. The device without BCP shows poor performance, only with J_{SC} of 3.21 mA/cm^2, V_{OC} of 0.68 V, *FF* of 0.37 and the *PCE* of 0.8 %. After the incorporation of BCP, the J_{SC}, V_{OC}, *FF* and *PCE* of the device are 3.71 mA/cm^2, 0.91 V, 0.46 and 1.6 %. Apparently, the device performance was greatly improved by employing BCP layer.

In the previous work, we have confirmed that the transmittance of 10-nm-thick BCP layer is nearly 99 %.[2-17] Therefore, the insertion of BCP layer will not affect the light absorption in the active layers, and the improvement of J_{SC} should be related to other factors, other than the absorption. Fig. 3-3 shows the *EQE* spectra of the devices and the absorbances of ITO/C_{60} (45 nm) and ITO/SubPc (15 nm). Apart from an

overall reduction in *EQE* for the device without BCP as compared to the device with BCP, the spectral features of the two devices coincide closely. At the wavelength of around 590 nm (the absorption peak of SubPc), the *EQE* values are 32 and 38 % for the devices without and with BCP, respectively, while they are 18 and 23 % at 460 nm (the absorption peak of C_{60}). We suppose that the total exciton population in device without BCP is lower than that with BCP, which may be caused by high exciton quenching rates at the ITO/C_{60} interface.

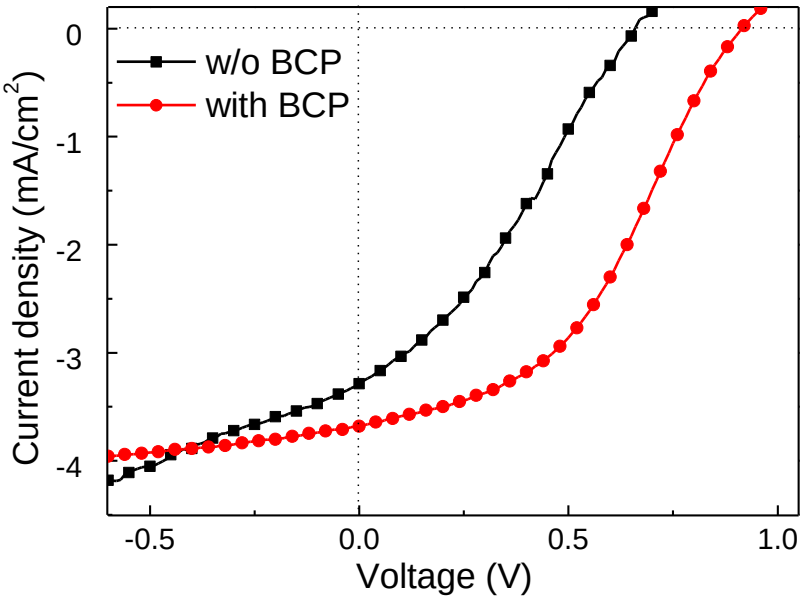

Fig. 3-2. *J-V* characteristics for the devices without BCP layer (filled squares) and with (filled circles).

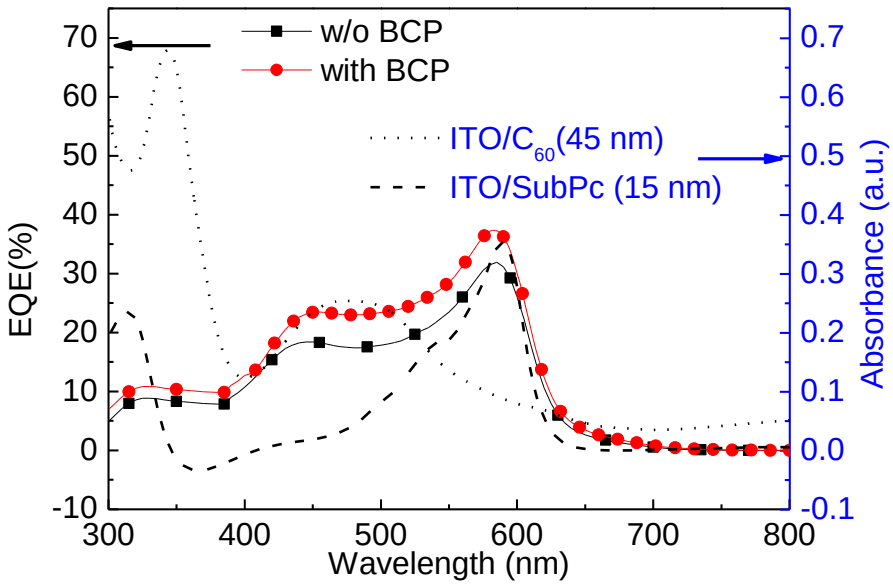

Fig. 3-3. *EQE* spectra for devices without (filled squares)/with BCP (filled circles) and the absorbances of ITO/C_{60} (squares) and ITO/SubPc (circles).

- Luminescence properties

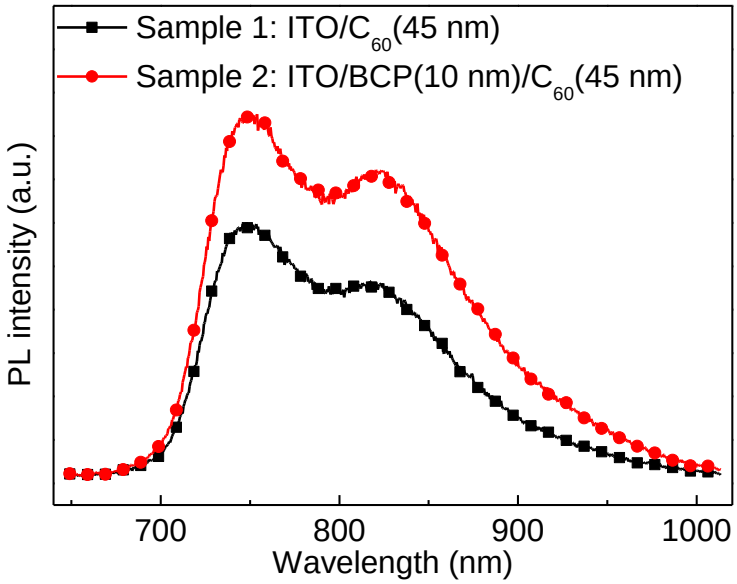

Fig. 3-4. The PL spectra of ITO/C_{60} (45 nm) and ITO/BCP(10 nm)/C_{60}(45 nm).

The exciton lifetime is determined by both radiative and nonradiative recombination rates. Considering that the radiative recombination rate of C_{60} is an intrinsic property and it will not be affected by the interfaces, the nonradiative procedure, say exciton quenching, can be examined by employing a quencher adjacent to C_{60}. Fig. 3-4 depicts the PL spectra of sample 1: ITO/C_{60} (45 nm) and sample 2: ITO/BCP (10 nm)/C_{60} (45 nm). Sample 1 shows low PL intensity while sample 2 yields a spectrum with higher intensity. The peaks around 729 and 826 nm correspond to the photoluminescence peaks of C_{60} thin film at room temperature.[3-20] In absence of BCP, that is, in the case of sample 1, nonradiative recombination at the ITO/C_{60} interface lead to a lower photoluminescence intensity. The phenomenon is expected near ITO surface, since the oscillating dipole field of the excited molecules induces a field inside the ITO.[3-21] This interaction may generate electron-hole pairs, phonons, or surface plasmons and thus quench the exciton. While in case of with BCP layer, sample 2 shows a stronger photoluminescence and consequently a lower exciton quenching rate. Therefore, the BCP indeed prevents exciton quenching between ITO and C_{60} interface and the larger population of exciton leads to an improved photocurrent in the device with BCP layer. In addition, the interfacial morphological modification also contributes to the increase of J_{SC} for the device with BCP buffer layer by forming an interdigitated donor/acceptor interface, which is beneficial to the dissociation of excitons.[3-17]

- Dark *J*-*V*

The correlation of V_{OC} and dark current J_S is inferred from:[3-22]

$$J = \frac{R_P}{R_S + R_P}\left\{ J_S\left[\exp\left(\frac{q(V - JR_S)}{nkT} \right) - 1 \right] + \frac{V}{R_P} \right\} - J_{ph}(V), \tag{3-1}$$

where J is the total current, R_P and R_S are the parallel and series resistance, respectively, J_S is the reverse dark

saturation current, n is the ideal factor, V is the biased voltage and J_{ph} is the photocurrent.

At open circuit condition, the total current J=0, then Eq. 3-1 can be simplified as

$$V_{OC} = \frac{nkT}{q} \ln\left[\frac{J_{ph}(V_{OC})}{J_s} + 1 - \frac{V_{OC}}{R_P J_s}\right]. \quad (3\text{-}2)$$

When $J_{ph} \gg J_S$, V_{OC} is proportional to ln (J_{ph}/J_S), suggesting that a large J_S results in a reduction of V_{OC}. The dark J-V characteristics, as shown in Fig. 3-5, yield 1.33×10^{-2} and 3.67×10^{-8} mA/cm^2 of J_S for the devices without and with BCP, respectively. Apparently, the insertion of BCP layer greatly suppressed the reverse dark saturation current. As a result, the V_{OC} was improved significantly. The large J_S in the device without BCP probably arises from the trap or defect states at the ITO/C_{60} interface, which may involve in charge trapping, and therefore act as charge recombination sites.

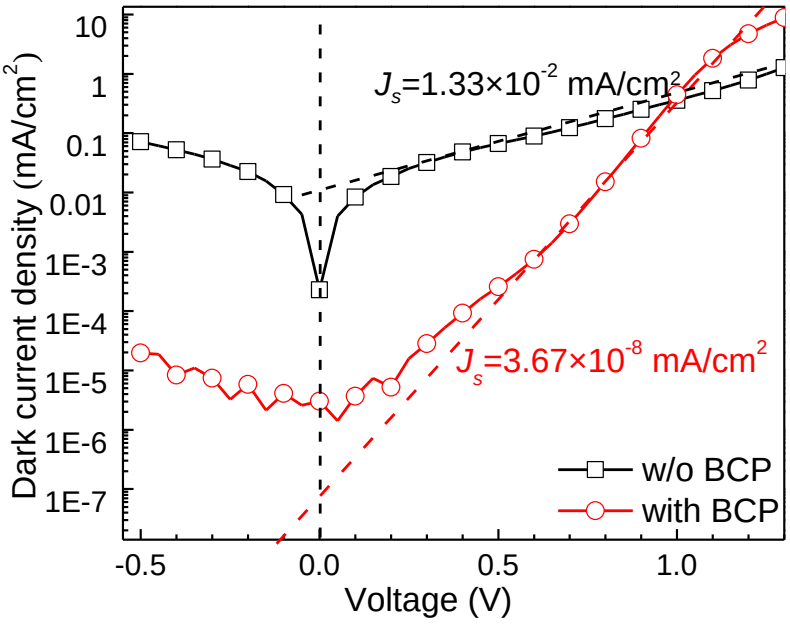

Fig. 3-5. Dark J-V characteristics for the devices without/with BCP layer.

- ITO/C_{60} interface

In C_{60} layer, the electron transfer can occur in singlet and triplet states, and the latter has a longer transition time. Therefore in a C_{60} layer with a solar cell structure (presence of donors), the C_{60}^- anion radial will be formed mainly from the triplet states.[3-23] These states are quite sensitive to the molecular oxygen and the energy level lies at about 1.6 eV above the ground state (Fig. 3-6).[3-24,3-25] In our work, for device free of BCP, the direct contact of ITO/BCP lead to the diffusion of oxygen from ITO into C_{60} layer and therefore, the C_{60}^- anion radial formed. Further, according to the work of Sun *et al.*[3-26] and Ding *et al.*[3-27] In single layer device with a structure of ITO/C_{60}/metal, the excitons will dissociate at ITO/C_{60} interface. At the very beginning after the device was exited by a pulsed laser, large quantity of excitons will generate in C_{60}, together with quite a few carriers. The holes generated by the exciton dissociation at ITO/C_{60} will be collected by ITO, leaving the electrons in C_{60}. In our devices, the remained electrons dissociated from ITO/C_{60} and C_{60}/SubPc will then be dispersed or captured by the states generated by oxygen molecules. This may eventually affect the device performance by slowing down the charge transportation, charge trapping or

even aggravating recombination of the charges.

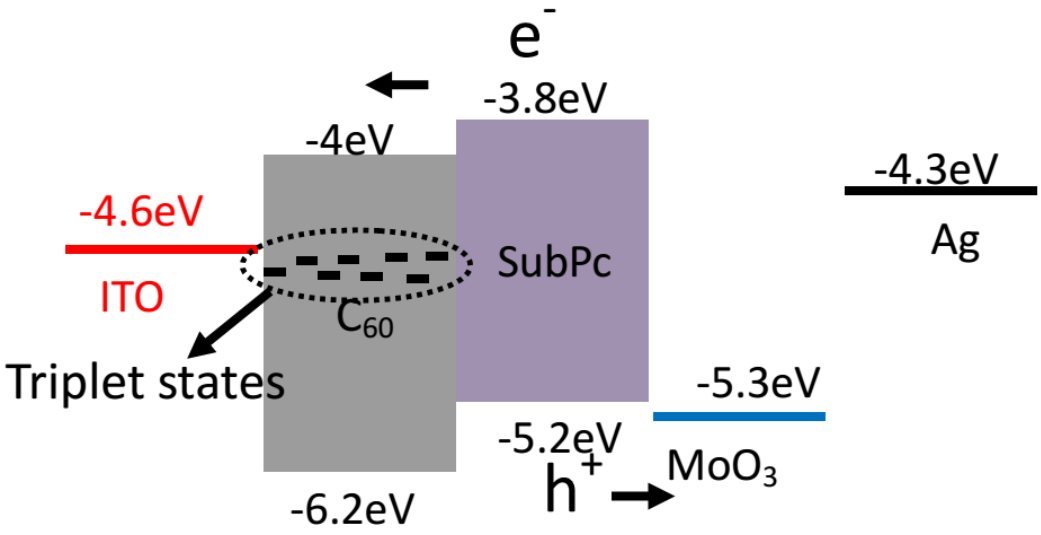

Fig. 3-6. Level alignment of the device free of BCP.

3.3.2 Transient characteristics

To get direct insight into the charge trapping, the TPV measurements were carried out. Figs. 3-7(a) and 3-7(b) show the TPV results for the device free of BCP without background illumination. From Fig. 3-7(a), we can see that the TPV plots are composed of: a fast rise after turn-on, followed by a slower increase till reaching equilibrium in ~100 μs; and a sharp decrease after turn-off, followed by a positive long tail. The rise after turn-on and the decay after turn-off get faster with the increase of light intensity. These features can be discerned more clearly when the plots are normalized, as shown in Fig. 3-7(b). At low pulse intensity, the population of photo-generated charge is small and the TPV rise time is long after turn-on. However, at higher pulse intensity, the photo-generated charge density is considerably high, and the rise becomes faster. This is an evidence of charge trapping. Likewise, in the turn-off behavior, the long positive tail arises from the slow charge detrapping after the mobile carriers have been swept out of the device. Therefore, the dependence of TPV on pulse light intensity suggests charge trapping and detrapping, which can be further confirmed by the TPV measurement under a constant background illumination, as shown in Figs. 3-7(c) and 3-7(d). With a background illumination, the trap states were occupied by the background illumination generated charges in advance. The TPV exhibits typical mobile charges behavior, namely, a fast rise to the equilibrium after turn-on and a fast decay after turn-off, as well as independence on the light intensity.

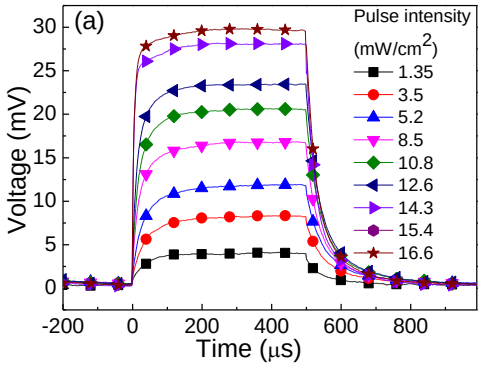

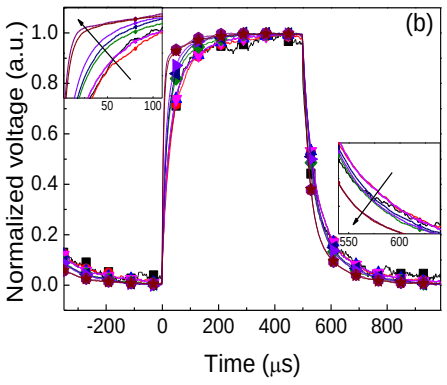

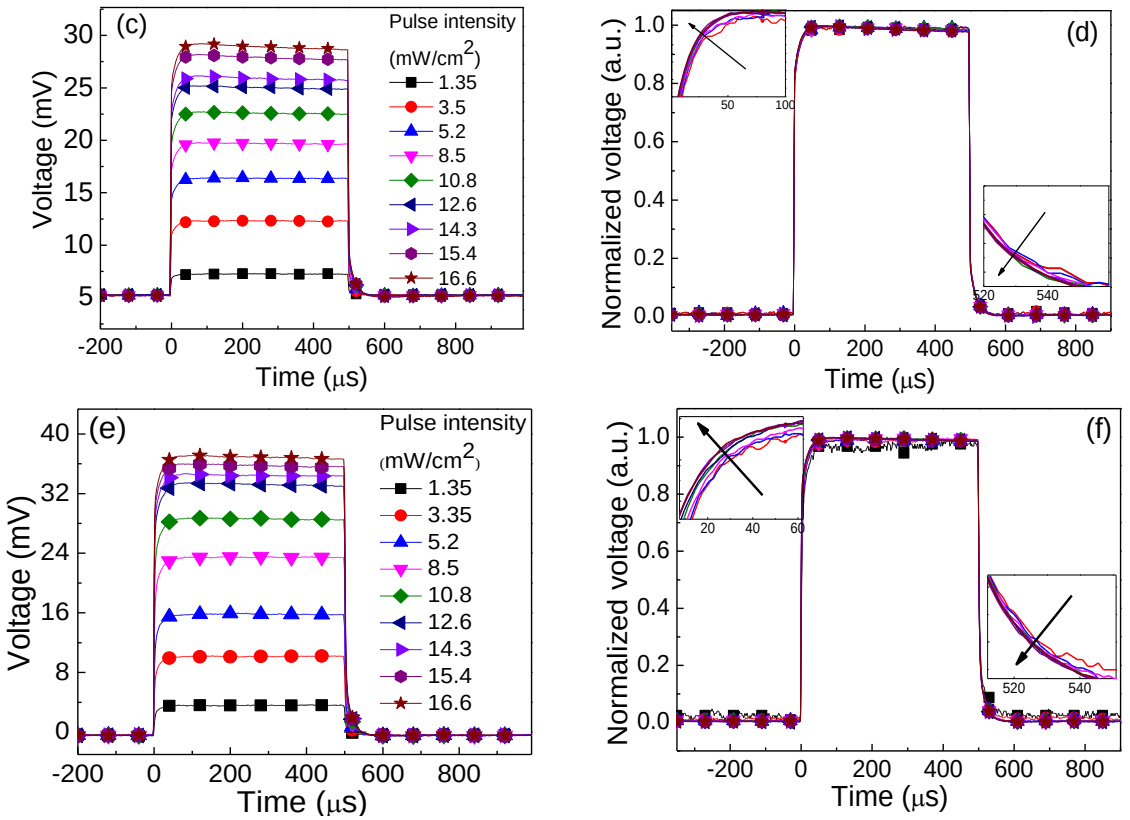

Fig. 3-7. TPV characteristics as a function of pulse intensity: (a,c,e) for the absolute traces and (b,d,f) for the normalized traces. The turn-on and turn-off dynamics are enlarged in the insets, with arrows pointing from low to high light intensity. (a,b) Plot the TPV of the device free of BCP without background illumination. (c,d) Plot TPV for the device without BCP under 5 mW/cm^2 background illumination. (e,f) Plot the TPV for the device with BCP without background illumination.

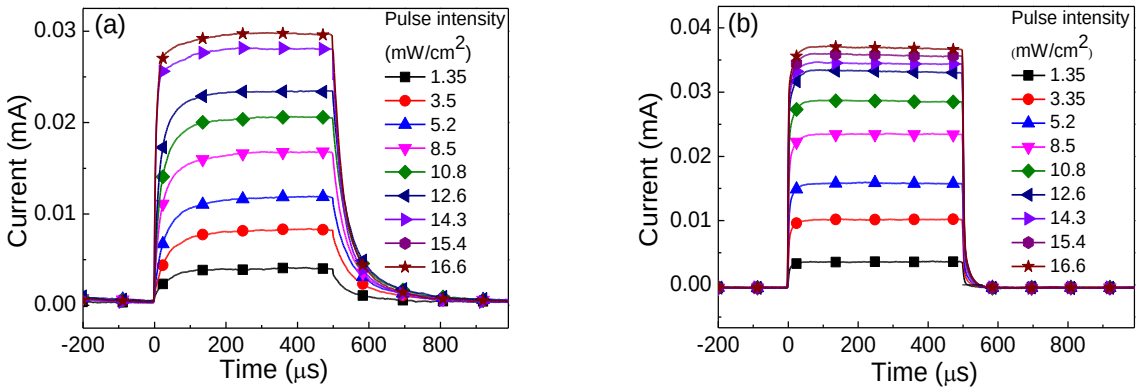

Fig. 3-8. Absolute values of TPC measurements for the devices (a) without and (b) with BCP as a function of incident light intensity.

In contrast, for the device with BCP, little variation was observed in the TPV shape under different pulse intensities (Fig. 3-7(e)). The normalized plots are overlapped (Fig. 3-7(f)). This pulse intensity independent feature suggests that the device with BCP is trap free. Since the only difference of the compared devices is the insertion of a 10-nm-thick BCP between ITO and C_{60}, we deduce that the build-up of charge trapping

mainly occurs at the interface between ITO and C_{60}, and the incorporation of BCP can eliminate the charge trapping. Therefore, the device performance was improved greatly by the insertion of BCP buffer layer.

3.3.3 The amount of extracted charges

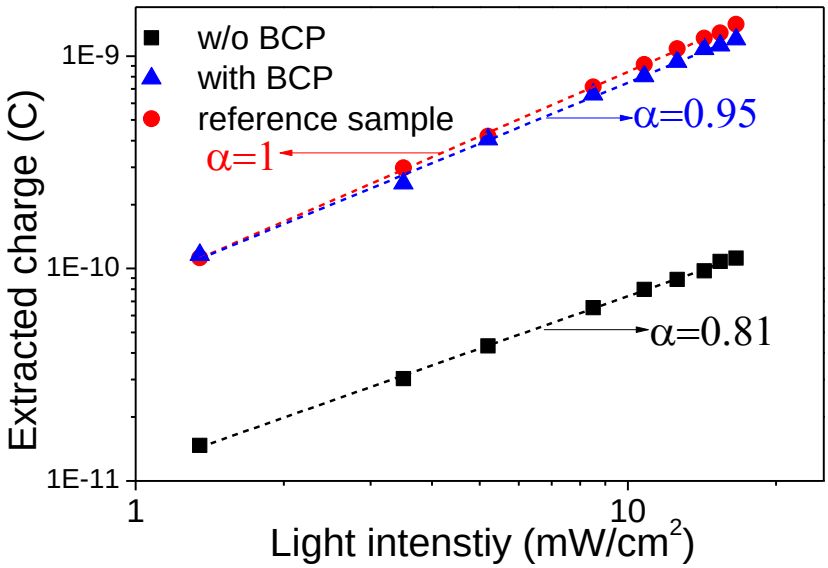

Fig. 3-9. Plots of extracted charge *vs* incident light intensity on the logarithmic scale at short circuit for the devices without/with BCP and reference sample after turn-off. The symbols represent the measured values and the dot lines are the exponential fitted lines which yield α.

Further insight into the nature of device operation could be provided by calculating the amount of extracted charge. Fig. 3-8 presents the photocurrent response of the devices without and with BCP as a function of incident light intensity. The amount of extracted charge is determined simply by integrating the area under the photocurrent decay transient. In the absence of charge trapping, the amount of extracted charge reflects the steady-state charge density in the device. On the contrary, in the presence of charge trapping, it cannot be assumed that all charge is extracted from the device, and the amount of extracted charge is a reflection of the efficiency of charge collection. For the device without BCP, the amount of extracted charge is calculated to be 7.42×10^{-11} C under 10 mW/cm^2 while that for the device with BCP is 7.65×10^{-10} C. The extracted charge vs incident light intensity at short circuit was plotted in Fig. 3-9. Here, we defined a parameter α to describe the relationship between extracted charges and light intensity, which stands for the slope of linear fitting for extracted charge vs ln(I). The device without BCP exhibits a sub-linear dependence with α=0.81, while the device with BCP almost shows linear dependence with α=0.95. As aforementioned, for the device without BCP under constant background illumination, the trap states were occupied prior to TPC measurement. Therefore, it can be regarded as a trap-free reference sample. The α of this reference sample is equal to 1, as illustrated in Fig. 3-9. The fitted α value for the device with BCP is quite close to 1, while that deviates from 1 for the device without BCP. This indicates that the device with BCP is trap free.

3.3.4 Recombination mechanisms

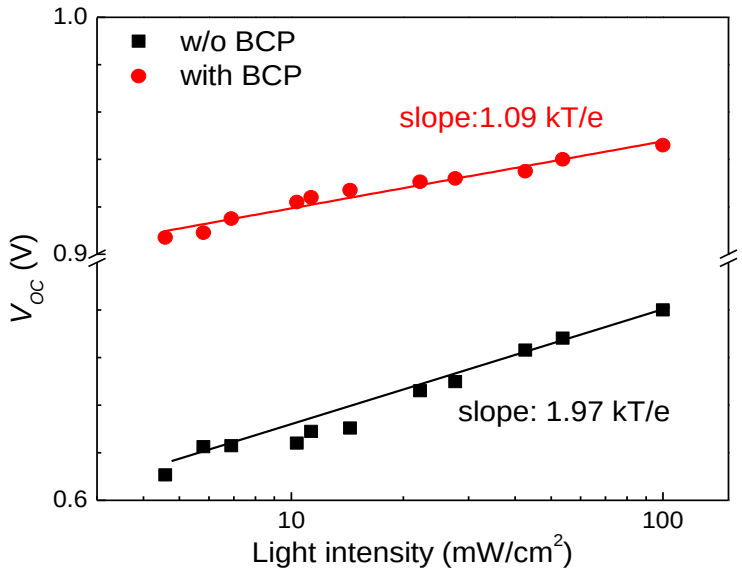

Fig. 3-10. V_{OC} as a function of incident light intensity in logarithm scale for the devices without/with BCP. The symbols are measured values and the solid lines are for the linear fitting.

The presence of traps can affect the device performance such as aggravating the recombination. The insight into the recombination mechanism can be obtained by measuring the V_{OC} as a function of the light intensity.[3-28,3-29] At open circuit, the photo current is zero and all of the carriers recombine within the cell. Thus, recombination studies at open circuit can provide detailed information of various mechanisms. The V_{OC} and light intensity (I) are correlated by the following expression:

$$V_{OC} = \frac{1}{e}\left(E_{LUMO}^{C60} - E_{HOMO}^{SubPc} - \Delta\right) - \frac{kT}{e} ln\left(\frac{n_e n_h}{N_C^2}\right), \quad (3\text{-}3)$$

where E_{LUMO}^{C60} is the LUMO level of C_{60}, E_{HOMO}^{SubPc} is the HOMO level of SubPc, n_e and n_h are charge density in C_{60} and SubPc, which are proportional to the light intensity (I), e is the elementary charge, k is the Boltzman constant, T is temperature in Kelvin, N_C is the effective density of states and Δ represents the relatively small band tailing to energy below the LUMO level of the acceptor. For the bimolecular recombination, the Eq. 3-3 can be simplified as:[3-29]

$$V_{OC} \propto \left(\frac{kT}{e}\right) ln(I) + constant. \quad (3\text{-}4)$$

This implies that the slope of V_{OC} vs ln(I) is equal to kT/e for bimolecular recombination. In the case of monomolecular trap-assisted recombination, due to the n_e and n_h at open circuit would be each proportional to I, the slope of V_{OC} vs ln(I) should be equal to 2 kT/e. The measured V_{OC} as a function of ln(I) for the devices without/with BCP is displayed in Fig. 3-10. We can see that the device with BCP gives a slope of 1.09 kT/e, while for the device without BCP it is 1.97 kT/e. This suggests that the trap-assisted recombination is aggravated in the device free of BCP.

The TPV and TPC results are also consistent with the aspect of energy level alignment. From the energy diagram of C_{60}/ITO interface reported by Liu *et al.*, the lowest unoccupied molecular orbital (LUMO) level shows downward band bending in C_{60} layer.[3-30] Although this energy level alignment resulted in no barrier for free carrier transportation, there was recombination in this interface. However, in the case of BCP,

strong band bending occurs at the C_{60}/BCP interface,[3-15] which tends to create an electric field in the active semiconductor layer that drives holes away from the ITO/active layer interface.[3-31,3-32] Therefore, it is beneficial to suppress the recombination at the interface. In addition, BCP layer can block the hole injection from ITO to the active layer due to the deep highest occupied molecular orbital (HOMO) level of BCP.[3-15] The effective suppression of recombination by BCP buffer layer is also contributed to the increase of V_{OC}. Based on the discussion above, the traps at the ITO/C_{60} interface affected the device performance, not only by the build-up of charge trapping but also by the aggravation of trap-assisted recombination.

3.3.5 Performance improvement by Ca incorporation

Fig. 3-11(a) shows the *J-V* characteristics of the devices without/with Ca inter layer under 100mW/cm^2 (AM 1.5 G) illumination. As aforementioned, the device without Ca (BCP device) exhibited J_{SC} of 3.71 mA/cm^2, V_{OC} of 0.91V, and *FF* of 0.45.These values corresponded to a *PCE* of 1.6%. After inserting the Ca layer, the device performance improved greatly, yield a J_{SC} of 5.76mA/cm^2, V_{OC} of 0.92V, *FF* of 0.54 and *PCE* of 2.9%. Most of the increase in the in the performance of the Ca device comes from the ≈55% and ≈20% enhancements in J_{SC} and *FF*. The series resistance (Rs) of the device was estimated from the inverse of the slope of the tangential line (*TL*) of the *J-V* curve at V_{OC},[3-33~3-36] as shown in Fig. 3-11(a).The insertion of the Ca inter layer decreases the *Rs* from 132 to 53 Ωcm^2, which leads to much higher *FF* as compared with the device without Ca interlayer. The improvement of J_{SC} is also in agreement with the external quantum efficiency (*EQE*) measurement (Fig. 3-11(b)). The *EQE* value exceeds 45% over the wavelength range 550 nm and 600 nm for Ca device.

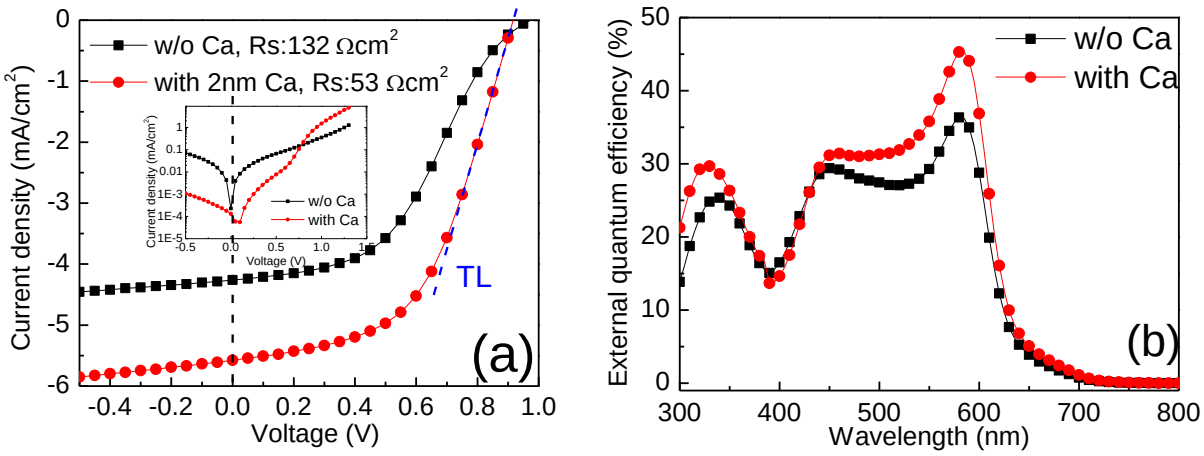

Fig.3-11. (a) *J-V* characteristics with dark *J-V* inset and (b) EQE spectra of the OSCs with and without Ca interlayer. The device structure is ITO/Ca (0 or 2 nm)/BCP/C_{60}/SubPc/MoO_3/Ag.

The recombination kinetics were investigated by measurements of the light intensity dependence of the *J-V* characteristics to get the insight into the increased *FF* and J_{SC} for Ca device.[3-29,3-37] The information of different recombination mechanism could be reflected by the light intensity dependent *J-V* measurements.[3-38~3-42] Fig. 3-12 shows the *J-V* curves of the devices without/with Ca as a function of light intensity. The Ca layer affects the shape of *J-V* curve which is strongly correlated with the recombination mechanism.[3-40] With the Ca layer (Fig. 3-12(b)), the photocurrent saturates faster at low

reversed biases. It suggests that in Ca device, much more photo-generated carriers are swept out prior to recombination. However, the photo current saturation rate is slower in the device without Ca, and the photo-generated carriers are not swept-out completely near short circuit. The Ca favors the sweep-out in competition with recombination, so that the recombination is suppressed and leading to higher *FF*.

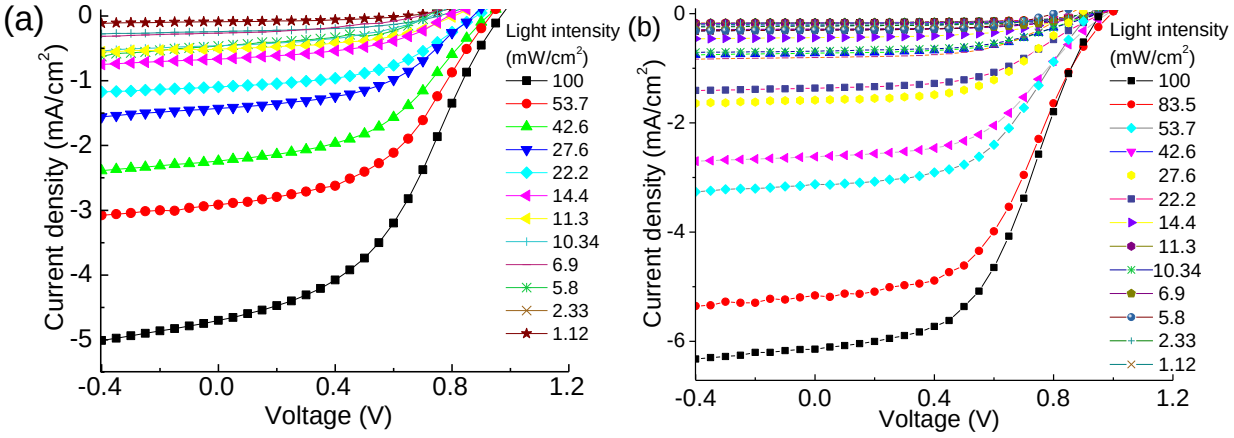

Fig. 3-12. *J-V* characteristics of OSCs with (a) 0 nm Ca and (b) 2 nm Ca, under various incident light intensities, ranging from 1.12 mW/cm^2 to 100mW/cm^2.

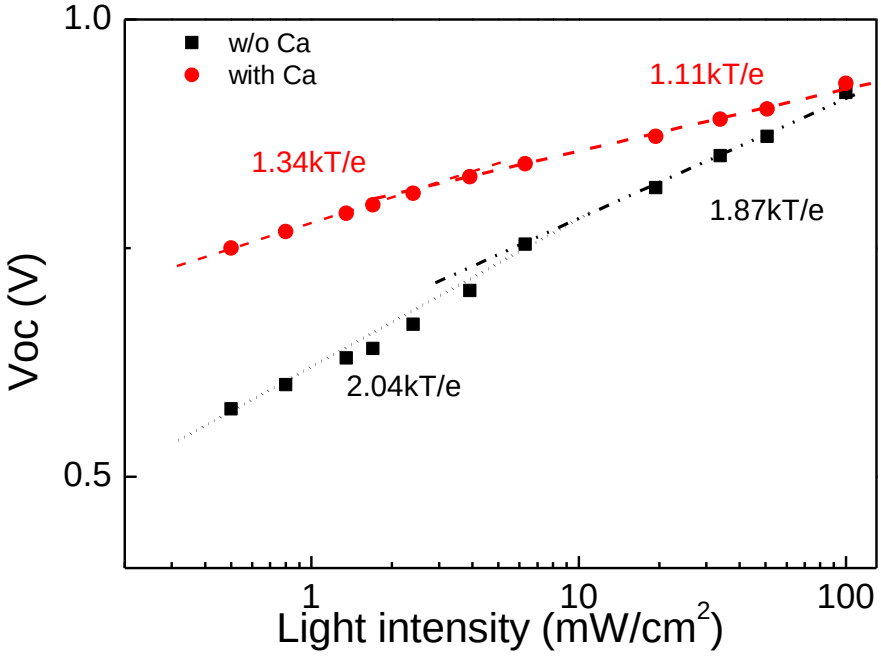

Fig. 3-13. The measured V_{OC} as a function of light intensity.

By measuring the light dependent V_{OC}, one can get the insight into the recombination mechanisms.[3-42,3-43] The photocurrent equals to zero at V_{OC}, and the photo-generated carriers are recombined in the device. At open circuit, where the extra bias is quite low, bimolecular recombination is predominant. When at short circuit, the recombination mechanism is accompanied by the charge sweep out. In an organic solar cell, the sweep out is approximately linearly with the light intensity, recombination only shows a small deviation from linearity. From Fig. 3-12(b), the photocurrent saturates fast at low reversed biases, the majority of the carriers are swept out prior to recombination while the charier sweep out is a little

bit slower in BCP device, (Fig. 3-12(a)), which implies photo-generated carriers are not completely swept out near J_{SC}. Thus, the Ca layer favors the sweep out in competition with recombination and leading to a higher *FF*.

The recombination mechanism can be obtained by monitoring the V_{OC} and J_{SC} as a function of light intensity (I). The V_{OC} and I are correlated by the following Eq. 3-4. The V_{OC} vs ln(I) relationship for the devices without/with Ca is shown in Fig. 3-13. For device free of Ca, a strong dependence of V_{OC} on light intensity is observed where the recombination at the open circuit is a combination of monomolecular (slope=2.04 kT/e, at low light intensities) and bimolecular processes (slope=1.87 kT/e, at high light intensities). After the incorporation of 2 nm Ca layer, the slopes were reduced from 2.04 kT/e to 1.34 kT/e at low light intensities and from 1.87 kT/e to 1.11 kT/e at high light intensities, respectively. This suggests that the use of Ca interlayer significantly suppressed the trap assisted recombination.

The charge recombination kinetics at short circuit for devices without/with Ca can be investigated by the J_{SC} vs light intensity (I). The J_{SC} correlated to I by the following formula:

$$J_{SC} \propto I^{\alpha} (\alpha \leq 1). \tag{3-5}$$

The bimolecular recombination shoud be minimum (α≈1) for the maximum carrier sweep-out. Therefore, any deviation from α≈1 implies the bimolecular recombination.[3-44~3-46] J_{SC} *vs.* I on log-log scale is shown in Fig. 3-14. It was fitted by the power law described above. The fitting of the data yield α=0.938 for device free of Ca, which can be attributed to bimolecular recombination. In the case of Ca device, after exponential power law fitting, α is 0.990, which implies that bimolecular recombination is close to minimum which suggests a high collection probability at short circuit.

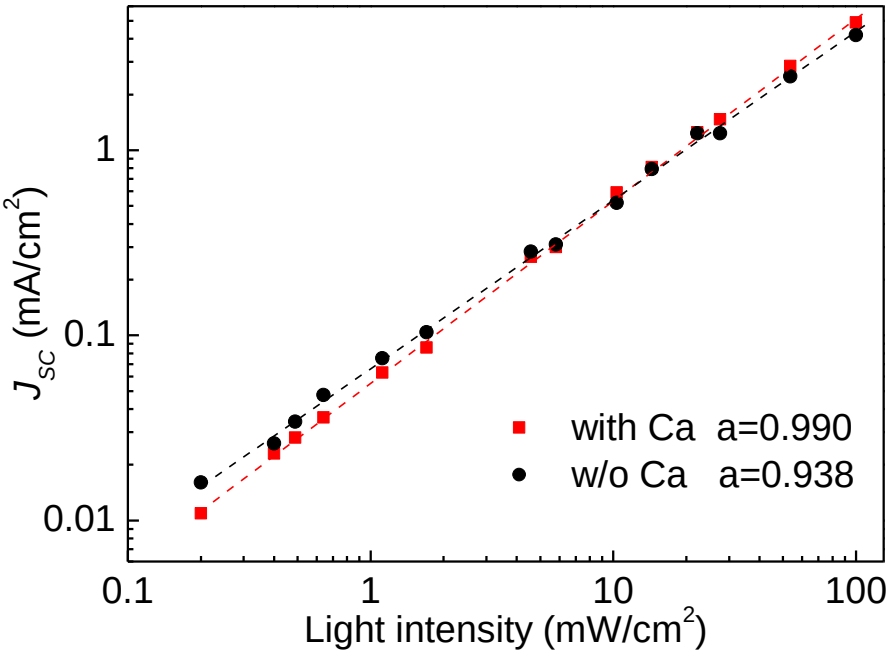

Fig. 3-13. J_{SC} of devices with Ca or without Ca interlayer plotted against light intensity (symbol) on the logarithmic scale. The fitted power law (line) yields α.

The internal voltage (V_{int}) can also contribute to the fast sweep-out. The inset of Fig. 3-11(a) shows the

dark *J-V* of both the devices. The device with Ca layer shows a turn-on voltage of ≈0.64 V whereas it is ≈0.5 V for the control device without Ca, indicating a significant increase in the built-in potential (V_{bi}) due to the lower work function of Ca (2.9 eV[3-16]) compared to ITO (4.6 eV).[3-47] A larger V_{bi} means a larger V_{int}, which might also facilitates the charge carriers escape the shallow traps.

3.4 Summary

The performance of inverted device was improved by inserting a BCP buffer between ITO cathode and active C_{60} layer. The effect of BCP in an inverted device was clarified. It can effectively block the excitons from quenching at the ITO/organic interface so that reduce the loss in the short circuit current. The incorporation of BCP also significantly suppressed charge trapping and recombination by preventing the direct contact of ITO and C_{60}. BCP is an effective cathode buffer for inverted small molecule OSCs. An extra 2 nm Ca interlayer between ITO and BCP further improved the performance of BCP device. We ascribe this improvement to a decrease in R_S and an increase of charge collection. The increased charge collection was verified to be due to the further suppression of the charge recombination.

References

[3-1] Y. Zhou, T. Taima, T. Miyadera, T. Yamanari, M. Kitamura, K. Nakatsu, Y. Yoshida. Glancing Angle Deposition of Copper Iodide Nanocrystals for Efficient Organic Photovoltaics. Nano Letters, **12** (2012) 4146.

[3-2] S.C. Veenstra, J. Loos, J.M. Kroon. Nanoscale Structure of Solar Cells Based on Pure Conjugated Polymer Blends. Progress in Photovoltaics: Research and Applications, **15** (2007) 727.

[3-3] Y. Zhou, T. Taima, T. Miyadera, T. Yamanari, M. Kitamura, K. Nakatsu, Y. Yoshida. Phase Separation of Co-Evaporated Znpc:C_{60} Blend Film for Highly Efficient Organic Photovoltaics. Applied Physics Letters, **100** (2012) 233302.

[3-4] K. Kawano, R. Pacios, D. Poplavskyy, J. Nelson, D.D.C. Bradley, J.R. Durrant. Degradation of Organic Solar Cells Due to Air Exposure. Solar Energy Materials and Solar Cells, **90** (2006) 3520.

[3-5] M. Jørgensen, K. Norrman, F.C. Krebs. Stability/Degradation of Polymer Solar Cells. Solar Energy Materials and Solar Cells, **92** (2008) 686.

[3-6] T. Kuwabara, T. Nakayama, K. Uozumi, T. Yamaguchi, K. Takahashi. Highly Durable Inverted-Type Organic Solar Cell Using Amorphous Titanium Oxide as Electron Collection Electrode Inserted between Ito and Organic Layer. Solar Energy Materials and Solar Cells, **92** (2008) 1476.

[3-7] B. Cumpston, I. Parker, K. Jensen. In Situ Characterization of the Oxidative Degradation of a Polymeric Light Emitting Device. Journal of Applied Physics, **81** (1997) 3716.

[3-8] K. Norrman, S.A. Gevorgyan, F.C. Krebs. Water-Induced Degradation of Polymer Solar Cells Studied by $H_2{}^{18}O$ Labeling. ACS Applied Materials & Interfaces, **1** (2008) 102.

[3-9] M. Hermenau, M. Riede, K. Leo, S.A. Gevorgyan, F.C. Krebs, K. Norrman. Water and Oxygen Induced Degradation of Small Molecule Organic Solar Cells. Solar Energy Materials and Solar Cells, **95** (2011) 1268.

[3-10] Z. Hong, Z. Huang, X. Zeng. Investigation into Effects of Electron Transporting Materials on Organic Solar Cells with Copper Phthalocyanine/C_{60} Heterojunctions. Chemical Physics Letters, **425** (2006) 62.

[3-11] C.J. Brabec, S.E. Shaheen, C. Winder, N.S. Sariciftci, P. Denk. Effect of LiF/Metal Electrodes on the Performance of Plastic Solar Cells. Applied Physics Letters, **80** (2002) 1288.

[3-12] S. Yoo, B. Domercq, B. Kippelen. Efficient Thin-Film Organic Solar Cells Based on Pentacene/C_{60} Heterojunctions. Applied Physics Letters, **85** (2004) 5427.

[3-13] N. Wang, J. Yu, Y. Zang, J. Huang, Y. Jiang. Effect of Buffer Layers on the Performance of Organic Photovoltaic Cells Based on Copper Phthalocyanine and C_{60}. Solar Energy Materials and Solar Cells, **94** (2010) 263.

[3-14] S. Wang, T. Sakurai, X. Hao, W. Fu, S. Masuda, K. Akimoto. Favorable Electronic Structure for Organic Solar Cells Induced by Strong Interaction at Interface. Journal of Applied Physics, **114** (2013) 183707.

[3-15] S. Wang, T. Sakurai, R. Kuroda, K. Akimoto. Energy Band Bending Induced Charge Accumulation at Fullerene/Bathocuproine Heterojunction Interface. Applied Physics Letters, **100** (2012) 243301.

[3-16] T. Sakurai, S. Toyoshima, H. Kitazume, S. Masuda, H. Kato, K. Akimoto. Influence of Gap States on Electrical Properties at Interface between Bathocuproine and Various Types of Metals. Journal of Applied Physics, **107** (2010) 043707.

[3-17] X. Hao, S. Wang, W. Fu, T. Sakurai, S. Masuda, K. Akimoto. Novel Cathode Buffer Layer of Ag-Doped Bathocuproine for Small Molecule Organic Solar Cell with Inverted Structure. Organic

Electronics, **15** (2014) 1773.

[3-18] H. Gommans, D. Cheyns, T. Aernouts, C. Girotto, J. Poortmans, P. Heremans. Electro-Optical Study of Subphthalocyanine in a Bilayer Organic Solar Cell. Advanced Functional Materials, **17** (2007) 2653.

[3-19] C-F. Lin, V.M. Nichols, Y-C. Cheng, C.J. Bardeen, M-K. Wei, S-W. Liu, C-C. Lee, W-C. Su, T-L. Chiu, H-C. Han. Chloroboron Subphthalocyanine/C_{60} Planar Heterojunction Organic Solar Cell with N, N-Dicarbazolyl-3, 5-Benzene Blocking Layer. Solar Energy Materials and Solar Cells, **122** (2014) 264.

[3-20] K. Pichler, S. Graham, O. Gelsen, R. Friend, W. Romanow, J. McCauley Jr, N. Coustel, J. Fischer, A. Smith. Photophysical Properties of Solid Films of Fullerene, C_{60}. Journal of Physics: Condensed Matter, **3** (1991) 9259.

[3-21] R. Chance, A. Prock, R. Silbey. Comments on the Classical Theory of Energy Transfer. The Journal of Chemical Physics, **62** (1975) 2245.

[3-22] N. Li, B.E. Lassiter, R.R. Lunt, G. Wei, S.R. Forrest. Open Circuit Voltage Enhancement Due to Reduced Dark Current in Small Molecule Photovoltaic Cells. Applied Physics Letters, **94** (2009) 023307.

[3-23] S. Bouchtalla, A. Deronzier, J-M. Janot, J-C. Moutet, P. Seta. Photoinduced Electron Transfer at an ITO/C_{60} Trapped in a Thin Polypyrrole Film Interface. Synthetic Metals, **82** (1996) 129.

[3-24] J.W. Arbogast, C.S. Foote, M. Kao. Electron Transfer to Triplet Fullerene C_{60}. Journal of the American Chemical Society, **114** (1992) 2277.

[3-25] R.R. Hung, J.J. Grabowski. A Precise Determination of the Triplet Energy of Carbon (C_{60}) by Photoacoustic Calorimetry. The Journal of Physical Chemistry, **95** (1991) 6073.

[3-26] X. Sun, B. Ding, Q. Song, X. Zheng, X. Ding, X. Hou. Dissociation of Excitons in the C_{60} Film Studied by Transient Photovoltage Measurements. Applied Physics Letters, **93** (2008) 063301.

[3-27] B-F. Ding, W.C. Choy, W-M. Kwok, Y. Yao, K.Y. Ho, C-Q. Wu. A Reduced Electron-Extraction Barrier at an Interface between a Polymer Poly (3-Hexylthiophene) Layer and an Indium Tin Oxide Layer. Organic Electronics, **14** (2013) 457.

[3-28] V. Gupta, A.K.K. Kyaw, D.H. Wang, S. Chand, G.C. Bazan, A.J. Heeger. Barium: An Efficient Cathode Layer for Bulk-Heterojunction Solar Cells. Scientific Reports, **3** (2013).

[3-29] S.R. Cowan, A. Roy, A.J. Heeger. Recombination in Polymer-Fullerene Bulk Heterojunction Solar Cells. Physical Review B, **82** (2010) 245207.

[3-30] T. Liu, N. Jiang, D. Wang, D. Luo, L. Yu, R. White, Z. Lu. Formation of Metal-Like Junction at Indium Tin Oxide/C_{60} Interface. Journal of The Electrochemical Society, **161** (2014) H21.

[3-31] C. Zhang, S-W. Tong, C-Y. Jiang, E-T. Kang, D.S. Chan, C. Zhu. Origin of Different Dependences of Open-Circuit Voltage on the Electrodes in Layered and Bulk Heterojunction Organic Photovoltaic Cells. Electron Devices, **57** (2010) 397.

[3-32] C.F. Zhang, S.W. Tong, C.Y. Jiang, E.T. Kang, D.S.H. Chan, C.X. Zhu. Origin of Different Dependences of Open-Circuit Voltage on the Electrodes in Layered and Bulk Heterojunction Organic Photovoltaic Cells. IEEE Transactions on Electron Devices, **57** (2010) 397.

[3-33] K. Rajkanan, J. Shewchun. A Better Approach to the Evaluation of the Series Resistance of Solar Cells. Solid-State Electronics, **22** (1979) 193.

[3-34] Y. Zheng, J. Xue. Organic Photovoltaic Cells Based on Molecular Donor-Acceptor Heterojunctions. Polymer Reviews, **50** (2010) 420.

[3-35] M. Ichikawa, E. Suto, H-G. Jeon, Y. Taniguchi. Sensitization of Organic Photovoltaic Cells Based on

Interlayer Excitation Energy Transfer. Organic Electronics, **11** (2010) 700.

[3-36] P. Peumans, A. Yakimov, S.R. Forrest. Small Molecular Weight Organic Thin-Film Photodetectors and Solar Cells. Journal of Applied Physics, **93** (2003) 3693.

[3-37] L. Koster, M. Kemerink, M.M. Wienk, K. Maturová, R.A. Janssen. Quantifying Bimolecular Recombination Losses in Organic Bulk Heterojunction Solar Cells. Advanced Materials, **23** (2011) 1670.

[3-38] W. Shockley, W. Read Jr. Statistics of the Recombinations of Holes and Electrons. Physical Review, **87** (1952) 835.

[3-39] D. Credgington, F.C. Jamieson, B. Walker, T.Q. Nguyen, J.R. Durrant. Quantification of Geminate and Non-Geminate Recombination Losses within a Solution-Processed Small-Molecule Bulk Heterojunction Solar Cell. Advanced Materials, **24** (2012) 2135.

[3-40] C.M. Proctor, C. Kim, D. Neher, T.Q. Nguyen. Nongeminate Recombination and Charge Transport Limitations in Diketopyrrolopyrrole-Based Solution-Processed Small Molecule Solar Cells. Advanced Functional Materials, **23** (2013) 3584.

[3-41] M. Mandoc, F. Kooistra, J. Hummelen, B. De Boer, P. Blom. Effect of Traps on the Performance of Bulk Heterojunction Organic Solar Cells. Applied Physics Letters, **91** (2007) 263505.

[3-42] L.J.A. Koster, V.D. Mihailetchi, R. Ramaker, P.W. Blom. Light Intensity Dependence of Open-Circuit Voltage of Polymer: Fullerene Solar Cells. Applied Physics Letters, **86** (2005) 123509.

[3-43] L. Koster, V. Mihailetchi, P. Blom. Bimolecular Recombination in Polymer/Fullerene Bulk Heterojunction Solar Cells. Applied Physics Letters, **88** (2006) 052104.

[3-44] I. Riedel, J. Parisi, V. Dyakonov, L. Lutsen, D. Vanderzande, J.C. Hummelen. Effect of Temperature and Illumination on the Electrical Characteristics of Polymer-Fullerene Bulk-Heterojunction Solar Cells. Advanced Functional Materials, **14** (2004) 38.

[3-45] P. Schilinsky, C. Waldauf, C.J. Brabec. Recombination and Loss Analysis in Polythiophene Based Bulk Heterojunction Photodetectors. Applied Physics Letters, **81** (2002) 3885.

[3-46] J.K. van Duren, X. Yang, J. Loos, C.W. Bulle-Lieuwma, A.B. Sieval, J.C. Hummelen, R.A. Janssen. Relating the Morphology of Poly (P-Phenylene Vinylene)/Methanofullerene Blends to Solar-Cell Performance. Advanced Functional Materials, **14** (2004) 425.

[3-47] H. Yu, X. Feng, D. Grozea, Z. Lu, R. Sodhi, A. Hor, H. Aziz. Surface Electronic Structure of Plasma-Treated Indium Tin Oxides. Applied Physics Letters, **78** (2001) 2595.

Chapter 4 Improvement of Stability for Bilayer Devices by Suppressing Trap Mediated Recombination

4.1 Introduction

In the previous chapter, we discussed the performance issue of the small molecule OSCs. While for OSCs based on SubPc/C_{60}, they also suffered from the poor stability. The possible reasons for the fast degradation include: the chemical and physical changes in the active layers, the instability of interfaces and the oxidation of electrodes.[4-1,4-2] Therefore, the lifetime could be improved by inserting air-stable buffer layer (eg., TiO_x,[4-3] ZnO,[4-4] poly(3,4-ethylenedioxythiophene):poly(styrene sulfonic acid) (PEDOT:PSS),[4-5] graphene oxide (GO),[4-6] and polymerized fluorocarbon film (CF_x)[4-7]) or by using a high work function metal electrode to avoid the degradation of constituted films. It is well known that the interfacial property of organic electronics plays an important role in the device performance, because they can greatly affect the charge transportation, charge injection and charge separation efficiency. In the reported works as aforementioned, people mainly focused on utilization of the air-stable buffer layer to block the water and oxygen for corroding the active layers. However, the factor of the interface change between active/buffer layers was inevitably included. In addition, the morphology of the active layer may change after inserting a different buffer layer, since the morphological properties are dependent on the surface energy and the properties of underneath layer. Therefore, the changes of interface and morphology bring complexity to illustrate the mechanism of the degradation.

Bathocuproine (BCP) is a commonly used buffer layer in the conventional OSCs. In our previous work, we have demonstrated that BCP can be used as a buffer layer in the inverted OSC.[4-8] In this chapter, we investigated the degradation mechanism of small molecule OSCs of both conventional and inverted structure with the identical buffer layers (MoO_3 as hole transport layer (HTL) and BCP as electron transport layer (ETL)). The inverted architecture was achieved by merely reversing the deposition sequence of the constituted functional layers on ITO substrates. In this case, the influences of interface properties and morphology issues can be ruled out.

Transient techniques such as charge extraction by linearly increasing voltage (CELIV),[4-9] ultra-fast transient photovoltage, time of flight (TOF)[4-10] and transient absorption spectroscopy (TAS)[4-11] can provide direct information regarding the charge transport and recombination dynamics to distinguish the energy loss mechanisms. However, these approaches require rigid laser pulse, which is not only far away from the real operating conditions of device, but also would induce damage to the interface or composed materials. TPC measurement, as introduced in Chapter 2, is quite preferable to acquire the charge behavior related information under the real device operating conditions. In TPC measurement, the information of the build-up of traps, charge transportation and dynamics of recombination can be obtained by studying the responses of photocurrent of OSCs to square pulsed optical excitation. The TPC measurement has been used to investigate the charge trapping and recombination dynamics of polymer OSCs,[4-12~4-14] but little report was carried out on the small molecule OSCs, especially for the dynamics of the degradation. In this chapter, the charge dynamic behaviors during the degradation for SubPc/C_{60} based small molecule OSCs was investigated by TPC measurement. The results suggest that in the conventional device, rapid degradation was caused by the energy loss which originated from the aggravated trap-mediated recombination. The device

lifetime was effectively improved by simply reversing the deposition sequence of the functional layers in order to constructing an inverted architecture. And the reason for the improvement of the stability was ascribed to be the decrease of the trap generation possibility and the effective suppression of the trap-mediated recombination by well protecting the C_{60} layer in the inverted device.

4.2 Experiment

The devices were prepared in a molecular beam epitaxy system by evaporating the subsequent layers in a vacuum chamber. The difference of the conventional and inverted devices is only the opposite deposition sequence of the layers. Their structures are shown in Fig. 4-1. The thickness of layers for MoO_3, SubPc, C_{60}, BCP and Ag are 25, 15, 50, 10 and 100 nm, respectively. In the conventional device, the indium tin oxide (ITO) and Ag acted as anode and cathode, respectively, whereas cathode and anode in the inverted structure device.[4-15] In order to characterize the degradation properties of OSCs, the unencapsulated devices were exposed to ambient air with a temperature of 25 ℃ and humidity of 50%. Except for carrying out the illuminated measurements, the devices were kept in dark. The *J-V* characteristics were measured with a *J-V* source meter (Advantest R6245) under illumination with a light intensity of 100 mW/cm^2 at AM 1.5 G spectrum. For the TPC measurements, a high brightness 525 nm light-emitting diode (Kingbright L-7104VGC-H) was driven by a pulse generator (Agilent 33220A) to generate a square-pulse optical excitation. The rise and fall time of light was measured to be less than 100 ns by a Si biased photo detector (THORLABS DET10A/M). The frequency of 1 kHz and pulse width of 500 μs were chosen. The pulsed light intensity, calibrated by an optical power meter (THORLABS PM100D), was varied by adjusting the bias applied on the light-emitting diode. Signals of photocurrent were recorded by using a digital oscilloscope (Agilent DSO-X-2024A, input impendence of 1 MΩ) to measure the voltage drop across an extra 50 Ω resistance series to the device.

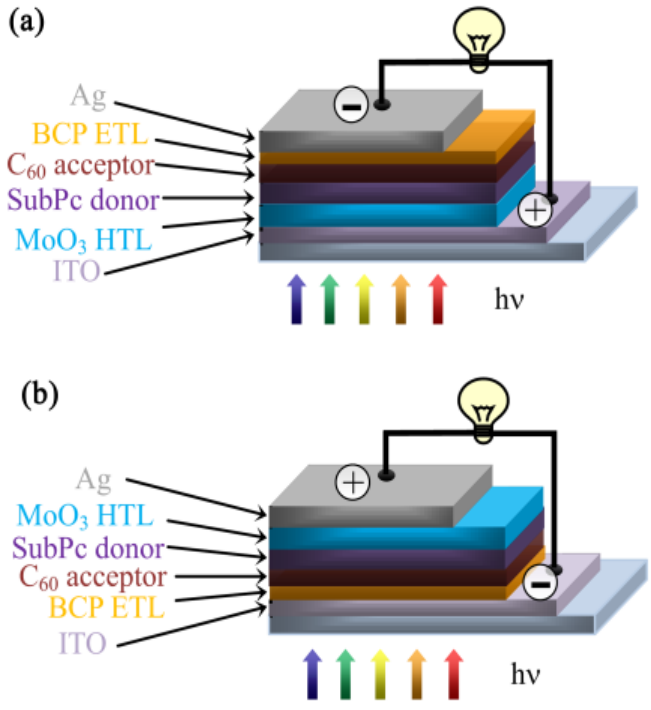

Fig. 4-1. The structures of (a) conventional and (b) inverted devices.

4.3 Results and discussions

4.3.1 Surface morphology

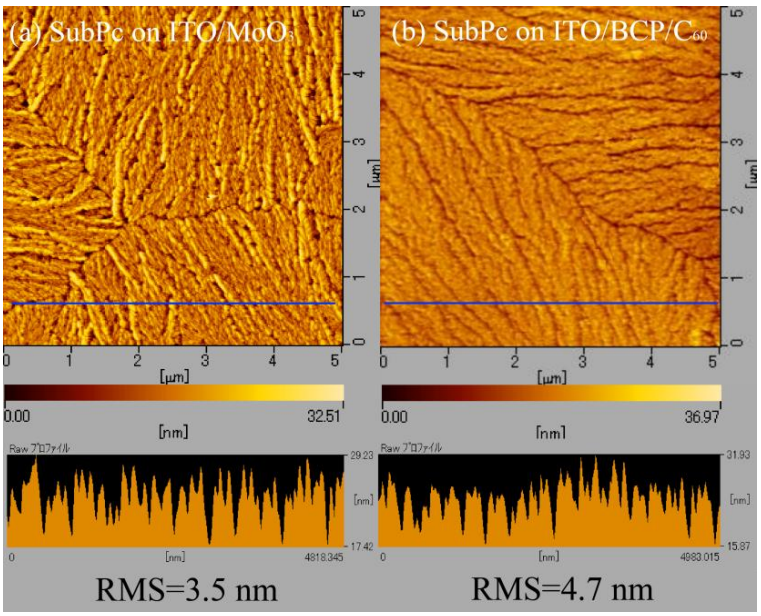

Fig. 4-2. AFM images of 15 nm SubPc thin films deposited on (a) ITO/MoO_3 (30 nm) and (b) ITO/BCP (10 nm)/C_{60} (50 nm). The images were taken with the scan area of 5μm×5μm.

As aforementioned, the surface morphology of active material, especially SubPc, is of significance in influencing the device performance. Kim *et al*.[4-16] have reported that the performance of SubPc/C_{60} based OSC is strongly dependent on the surface morphology of SubPc, that is, a corrugated nanostructure is necessary in order to form interdigitated donor-acceptor interface. The surface morphologies of the SubPc thin films (15 nm) on ITO/MoO_3 (30 nm) and ITO/BCP (10 nm)/C_{60} (50 nm) were examined using AFM, which are presented in Fig. 4-2. The root mean square roughness (RMS) of SubPc films deposited on ITO/MoO_3 and ITO/BCP/C_{60} are 3.5 and 4.7 nm respectively. We can tell that except for the little difference in the roughness, the SubPc films show similar surface morphologies from the viewpoint of forming corrugated structure. Therefore, constructing the inverted architecture by merely reversing the deposition sequence of films did not drastically change the morphological properties of active materials. Therefore, the influence of the morphology change of active materials and the interface in both conventional and inverted structures could be minimal, providing us opportunity to focus on the charge dynamic properties, which will be discussed later.

4.3.2 *J-V* characteristics and aging process

Fig. 4-3 shows the *J-V* characteristics for both the devices as a function of aging time. The fresh conventional device shows a J_{SC} of 3.86 mA/cm^2, V_{OC} of 1.02 V, *FF* of 0.49 and *PCE* of 1.93%. With the increased exposure time, the device performance becomes worse seriously. The reductions of J_{SC}, V_{OC} and *FF* are all responsible for the degradation of device performance. From the variation of *PCE* during the degradation, as shown in Fig. 4-3(c), we can see that it only took 20 hours for the *PCE* to decay to 50% of its initial value. After being exposed for 44 hours, the device degraded heavily, only with a low *PCE* of 0.29%. On the other hand, the inverted device fabricated by merely reversing the deposition sequence of all the

functional layers shows much better stability. Fig. 4-3(b) depicts the *J-V* characteristics of inverted device as a function of aging time. The fresh inverted device shows a J_{SC} of 4.71 mA/cm^2, V_{OC} of 0.99 V, *FF* of 0.41, and *PCE* of 1.91%, which is comparable with the conventional one. The *PCE* variation for this inverted device in 480 hours aging time is shown in Fig. 4-3(c). It can be seen that even if aged for 480 hours, the inverted device still shows 60% of the initial value. By constructing an inverted architecture, the device stability was improved greatly with a half-lifetime of over 480 hours.

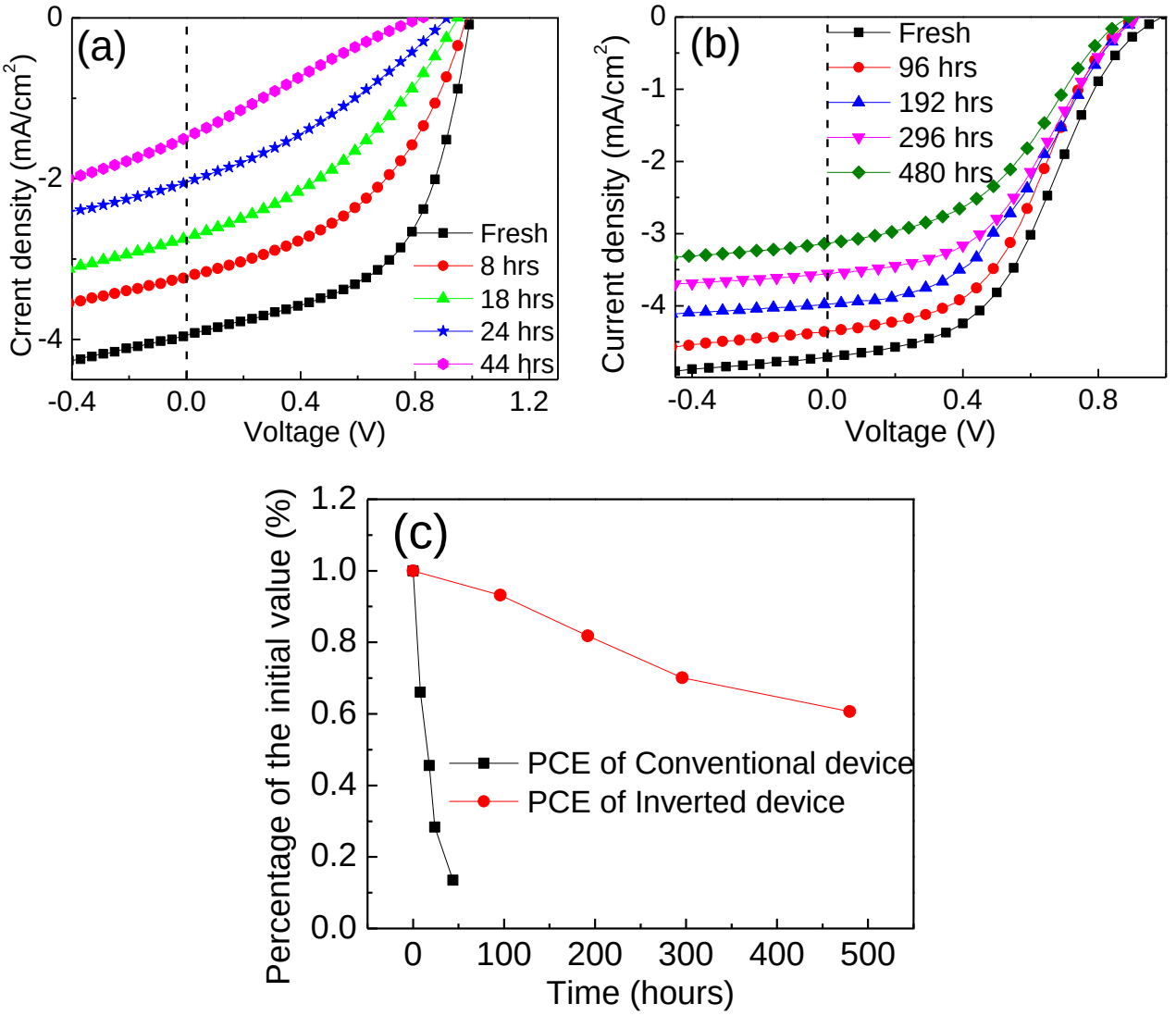

Fig. 4-3. The *J-V* curves of (a) conventional device and (b) inverted device as a function of aging time. The variation of normalized *PCE* during degradation is shown in (c).

As compared with reported small molecule OSCs with *PCEs* up to 3.6%,[4-17,4-18] what we are presenting is a bit low. One may concern that if the lifetime of the device will be affected by the initial *PCE*. So here we also show the *J-V* curves for optimized device which shows an optimized *PCE* of 2.7% as a function of degradation time duration, as shown in Fig. 4-4 and their photovoltaic parameters are listed in Table 4-1.

From Fig. 4-4(b) we can clearly observe that the optimized device o-1 show the quite similar degradation procedure as that used as investigating the stability. The main development in the *PCE* for the

optimized device comes from the increase in the J_{SC} and *FF*, which are ascribed to the optimized functional layers thicknesses. The structure of the optimized device is ITO/MoO_3(10 nm)/SubPc(13nm)/C_{60}(35 nm)/BCP(5 nm)/Ag (100 nm) while with a poor reproducibility of an average *PCE* of 1.73% and deviation of ±0.98% for the 16 devices of the same batch while in the batch of the present device, the average *PCE* is 1.81±0.12%. The poor reproducibility of the optimized device may be due to the nonuniformity of the ultrathin buffer layers that resulted in the direct contact of electrode and active layer.

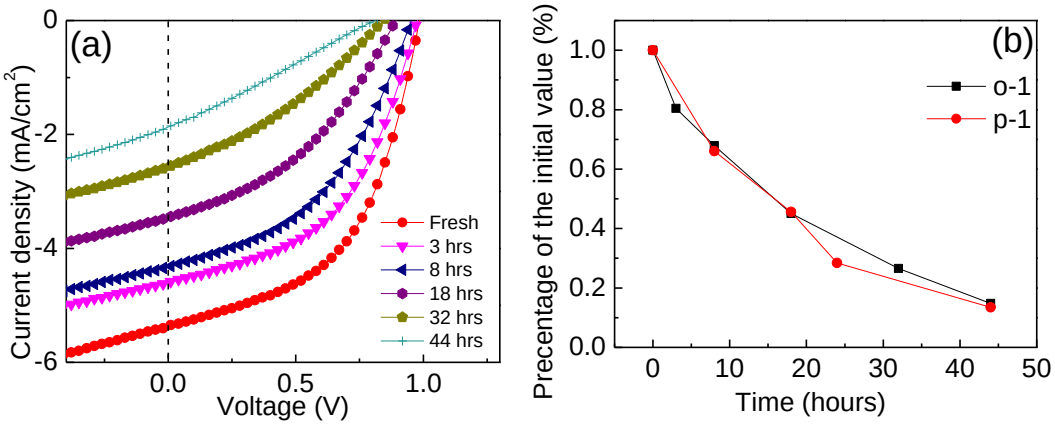

Fig. 4-4. (a) The *J-V* curves of conventional device with an initial *PCE* of 2.71% and (b) the degradation procedure for the performance optimized device (o-1) and the device in the present device (p-1).

Table 4-1. The photovoltaic parameters of conventional device with increased aging time.

Aged time (hours)	J_{SC} (mA/cm^2)	V_{OC} (V)	*FF*	*PCE* （%）	R_S (Ωcm^2)
0	5.36	0.99	51.3	2.71	46
3	4.6	0.98	48.6	2.18	61
8	4.32	0.95	44.6	1.84	87
18	3.45	0.89	39.6	1.22	132
32	2.57	0.84	33.2	0.72	419
44	1.87	0.81	26.6	0.40	815

Table 4-2 The photovoltaic parameters of conventional and inverted devices with increased aging time

	Aged time (hours)	J_{SC} (mA/cm^2)	V_{OC} (V)	*FF*	*PCE* (%)	R_S (Ωcm^2)
Conventional device	0	3.86	1.02	0.49	1.93	44
	8	3.22	0.99	0.40	1.28	82
	18	2.70	0.92	0.33	0.89	145
	24	2.07	0.90	0.29	0.54	496
	44	1.49	0.82	0.24	0.29	847
Inverted device	0	4.71	0.99	0.41	1.91	380
	96	4.35	0.98	0.40	1.71	332
	192	4.01	0.97	0.40	1.52	266
	296	3.58	0.95	0.41	1.42	239
	480	3.14	0.91	0.40	1.14	388

The photovoltaic parameters of conventional and inverted devices during the aging process were

summarized in Table 1, in which the series resistance (R_S) was calculated from the inverse of the slope of the tangential line of the *J-V* curve at V_{OC}.[4-19,4-20] As shown in Table 4-1, for the conventional device, R_S increases rapidly from 44 (for the fresh device) to 847 Ω cm^2 (for the device aged for 44 hours). The increase of R_S is the main cause of the deterioration of J_{SC}. It has been reported that C_{60} is very sensitive to oxygen and water, which would induce the decrease of carrier mobility.[4-21] In the conventional OSCs, the C_{60} is adjacent to the top metal cathode, suggesting that it is vulnerable to the air atmosphere. Thus, we can ascribe the increase of R_S to the carrier mobility decrease of C_{60} layer with increasing exposing time. After degradation, the V_{OC} of the conventional device also decreased rapidly from 1.02 V to 0.83 V. The decrease of V_{OC} suggests that the recombination may be aggravated during the degradation. It has also been reported that the performance of C_{60} based organic filed-effect transistor (OFET) is significantly sensitive to oxygen and water, which will lead to the transition from unipolar n-type to ambipolar for C_{60} layer and deteriorate the electron mobility.[4-22] Also, in case of C_{60}/BCP, upon the exposure of oxygen or water, the Fermi level of BCP shifts towards its LUMO. Owing to the formation of interfacial dipole, a VL offset of 0.3 eV takes place in the BCP/C_{60} junction prepared under UHV while no VL offset exist after exposure of oxygen or water. The water or oxygen can induce a higher extent of energy level bending in the HOMO of C_{60} at the BCP/C_{60} junction. The HOMO of C_{60} shows 0.3 eV bending in the BPC/C_{60} junction prepared in UHV, while the HOMO of C_{60} shows 0.8 eV bending after the exposure to oxygen and water. This suggests that upon ambient gas exposure, the band bending would shift the LUMO of C_{60} downward at the interface. This locally low energy LUMO can behave effectively as electron traps.[4-23] In C_{60}-based OSC, the generation of traps may deteriorate the device performance by the increase of recombination rate.

4.3.3 Recombination mechanisms

The trap-assisted recombination is a two-step process: 1) a new energy level is created inside the energy band gap by a trap state; and 2) this new energy level captures a charge carrier that subsequently recombines with an opposite charged carrier due to their Coulomb interaction.[4-24] The impacts of trap-assisted recombination could be revealed by the light intensity dependence of V_{OC}. The V_{OC} and light intensity (I) are correlated by the following expression:[4-25]

$$V_{OC} = \frac{1}{e}\left(E_{LUMO}^{C60} - E_{HOMO}^{SubPc} - \Delta\right) - \frac{kT}{e} ln\left(\frac{n_e n_h}{N_c^2}\right), \quad (4\text{-}1)$$

where e is the elementary charge, E_{LUMO}^{C60} is the lowest unoccupied molecular orbital (LUMO) level of C_{60}, E_{HOMO}^{SubPc} is the highest occupied molecular orbital (HOMO) of SubPc, Δ represents the relative small band tailing to energy below the LUMO of acceptor, k is the Boltzman constant, T is the temperature in Kelvin, N_C is the effective density of states, and n_e and n_h are the electron and hole densities. In the case of bimolecular recombination, $n_e n_h = G/\gamma$,[4-26] in which γ is the bimolecular recombination constant and G is the generation rate of polaron-pairs. Considering that G is the only term which is proportional to the light intensity (I), the V_{OC} could be given by:[4-25]

$$V_{OC} \propto \left(\frac{kT}{e}\right) ln(I) + const. \quad (4\text{-}2)$$

Here I is the incident light intensity. This formula implies that the slope of V_{OC} vs ln(I) is equal to kT/e for bimolecular recombination. For the trap-assisted recombination, due to the n_e and n_h at open circuit would be each proportional to light intensity, a stronger dependence of V_{OC} on light intensity is expected, namely, with a slope of $2\ kT/e$ for V_{OC} vs ln(I).[4-25] Fig. 4-4(a) depicts the V_{OC} vs ln(I) relationship for fresh, aged for 8, 18 and 44 hours of conventional device. With the increase of aging time, a gradual increase in the

slope was witnessed, from 1.17 *kT/e* for the fresh device to 1.91 *kT/e* for the heavily degraded one (44 hours). This suggests that the trap-assisted recombination was aggravated during the air-exposure process. This is also consistent with the decrease of V_{OC} with increasing the aging time.

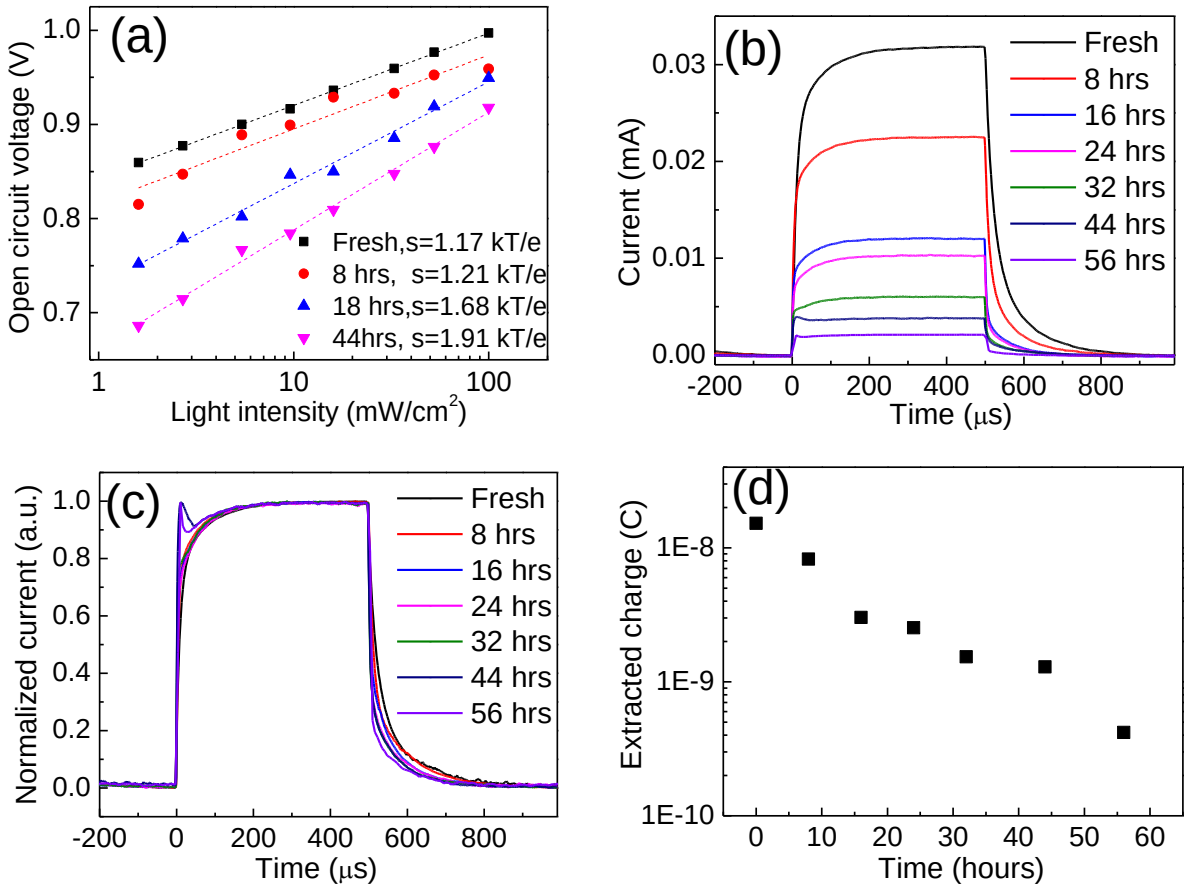

Fig. 4-4. The characteristics of conventional device as a function of aging time: (a) light intensity dependent $V_{OC,}$ (b) the absolute transient photocurrent, (c) normalized transient photocurrent, and (d) the extracted charge.

The aggravation of recombination during the degradation process can be further verified by the TPC measurement. Figs. 4-4(b) and 4-4(c) present the turn-on and turn-off dynamics of TPC as a function of aging time, with pulse light intensity of 14.3 mW/cm^2. The transient photocurrent signal of the fresh device is composed of a fast rise followed by a slow increase until reach the equilibrium after turn-on and a fast decay with a gradual decreased positive tail after turn-off. However, the TPC signals obviously changed with the increased aging time. As shown in Fig. 4-4(b), for the turn-on behavior, the intensity of the TPC decreases along with the aging time, which is due to the trap-induced reduction in charge generation efficiency.[4-13,4-27] In addition, a threshold in turn-on behavior of the TPC emerged with the increased exposing time. This feature can be clearly discerned when the curves are normalized in Fig. 4-4(c). Since the threshold persists for ~100 μs, which is consistent with the timescale of the charge trapping,[4-27] we therefore attribute the threshold to the trap mediated recombination. As for the turn-off dynamics, a fast decay followed by a long-lived positive tail suggests the slow detrapping process of the trapped charges in the aged device. The aggravated recombination possibility may reduce the amount of the extracted charges.[4-27] The amount of extracted charges can be estimated from TPC curves by integrating the area

under the photocurrent decay transients and the results were plotted in Fig. 4-4(d). It suggests that the loss of the extracted charges in the turn-off behavior mainly comes from the exacerbated carrier recombination after degradation, reflecting by the monotonically decreased charge amount with the increased aging time.

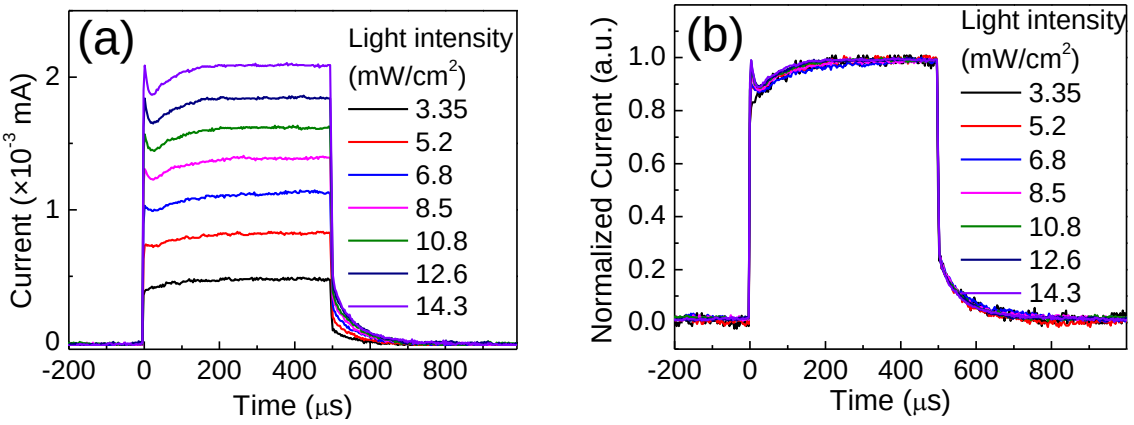

Fig. 4-5. Light intensity dependence of photocurrent transients for the conventional device after aged 56 hours: (a) for the absolute traces and (b) for the normalized traces.

The trap mediated recombination in the degraded device could also be clarified by observing the photocurrent transients as a function of incident light intensity. Fig. 4-5 presents the short circuit photocurrent response to the pulsed light for the heavily aged device. From Fig. 4-5(a), we can see that the TPC signal displays fast turn-on and turn-off dynamics with a quasi-rectangular shape at low intensities. With the increase of pulse intensity, a threshold after turn-on is emerged and becomes prominent. The turn-on and turn-off features can be more clearly discerned in the normalized traces in Fig. 4-5(b). For the turn-on behavior, the population of the photo-generated charges is limited under low pulse intensity, so the effect of recombination is minimal. In this case, the TPC only reflects the trapping/detrapping process. However, with increasing pulse intensity, the photo-generated charge density becomes higher and the population of the trapped charges increases until reaching the equilibrium. The free carriers were swept out and some of them were then killed either by trap-assisted recombination (for both the trapped and free charges) or by internal field redistribution induced bimolecular recombination (only for the free charges). Therefore, the threshold after turn-on appeared under high light intensities is also an evidence of trap mediated recombination.

On the other hand, the long tail following the sharp decrease in the turn-off behavior suggests that the charges are still extracted for ~300 μs due to detrapping. For device with traps that were not yet involved in obvious trap-mediated recombination, owning to the slow detrapping process, the transient photocurrent after turn-off is expected to be light intensity dependent. However, except for the presence of threshold, the traces in the turn-off behaviors in normalized TPC in Fig. 4-5(b) are overlapped under various light intensities. This is therefore attributed to a combined behavior of charge detrapping and trap mediated recombination, rather than a simple detrapping process.

The TPC measurement was then used to understand the stability improvement of inverted device. Ignoring bimolecular recombination at high intensity, for trap-free charge transport and fast electron-hole pair separation, the turn-on behavior is primarily determined by the charge mobility and independent of pulse intensity. Figs. 4-6(a) and 4-6(b) present the TPC of inverted device as a function of aging time, with pulse light intensity of 14.3 mW/cm^2. The photocurrent transient increases rapidly to the plateau region, and

decreases fast after turn-off. As compared to the conventional device, the turn-on and turn-off dynamics of the inverted device is much faster, indicating fast transport of the free carriers in the inverted device. With the increased aging time, the intensity of the TPC decreases, which coincides with the decreased J_{SC}. This TPC intensity reduction in the aged devices may due to the trap-induced reduction in charge generation efficiency. Additionally, there is little change in the TPC shape under various exposing time in the inverted device, whereas aforementioned drastic change of TPC signal in the conventional device. From the normalized TPC traces in Fig. 4-6(b), we can see that the inverted device shows no dependence on aging time in 480 hours. This suggests that the charge behaviors were not significantly affected by the exposure.

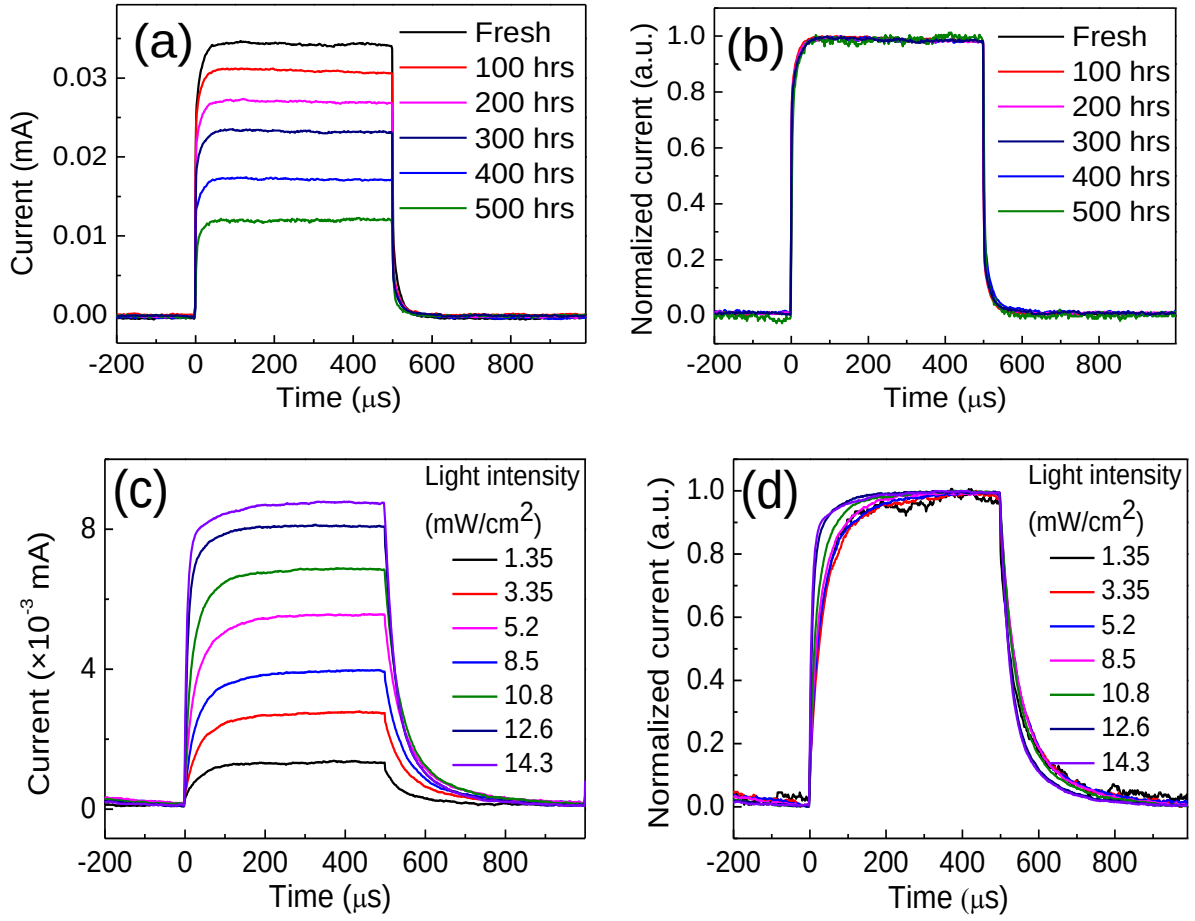

Fig. 4-6. Photocurrent transients of inverted device: (a), (b) for the TPC as a function of aging time, and (c), (d) for 480-hours-aged device as a function of pulse intensity. (a), (c) are for the absolute traces and (b), (d) are for the normalized traces.

To get further insight into the charge behaviors after aging, the TPC results for the inverted device aged for 480 hours as a function of light intensity are shown in Figs. 4-6(c) and 4-6(d). We can see that at low pulse intensities, the TPC shows slower dynamics, which are related to the time taken for the trapping/detrapping processes to reach steady state after turn-on, or the time taken for charges detrapping after turn-off. In addition, not like the degraded conventional device, the photocurrent transients of inverted device aged for 480 hours are dependent on the pulse intensity, which can be clearly observed in Fig. 4-6(d). Such pulse intensity dependent behaviors only suggest the trapping and detrapping effects but no evident trap mediated recombination. Importantly, although the magnitude of TPC decreases in the aged device, there is no threshold after turn-on, even at high light intensities. This suggests that the trap mediated recombination is

greatly suppressed, which is consistent with the small change of V_{OC} during 480 hours aging: from 0.99 V to 0.91 V. The stability is therefore improved significantly due to the suppression of the trap mediated recombination in inverted device.

4.4 Summary

The degradation mechanism of C_{60}-based small molecule OSCs of conventional and inverted structure with identical cathode and anode buffer layers was investigated by using TPC measurement. For the conventional device, it only takes 20 hours for the *PCE* to decay to 50% of its initial value. The appearance of a threshold after turn-on and pulse intensity independence of turn-off dynamics in the TPC for the heavily degraded conventional device are ascribed to the aggravation of the trap mediated recombination after exposure to the air ambient. In contrast, the stability of the inverted device was improved greatly, with a half-lifetime of over 480 hours. The absent of a threshold in the turn-on dynamics and a pulse intensity dependent turn-off trace in the TPC implies that the trap mediated recombination was significantly suppressed in the inverted structure. This study demonstrates fast degradation mechanism of the conventional device, and provides directions in improving the device stability.

References

[4-1] X. Wang, C. Xinxin Zhao, G. Xu, Z.-K. Chen, F. Zhu. Degradation Mechanisms in Organic Solar Cells: Localized Moisture Encroachment and Cathode Reaction. Solar Energy Materials and Solar Cells, **104** (2012) 1.

[4-2] M. Jørgensen, K. Norrman, F.C. Krebs. Stability/Degradation of Polymer Solar Cells. Solar Energy Materials and Solar Cells, **92** (2008) 686.

[4-3] J. Chang, Z. Lin, C. Jiang, J. Zhang, C. Zhu, J. Wu. Improve the Operational Stability of the Inverted Organic Solar Cells Using Bilayer Metal Oxide Structure. ACS applied Materials & Interfaces, **6** (2014) 18861.

[4-4] Z. Kam, X.Z. Wang, J. Zhang, J. Wu. Elimination of Burn-in Open-Circuit Voltage Degradation by ZnO Surface Modification in Organic Solar Cells. ACS Applied Materials & Interfaces, (2014).

[4-5] E. Bovill, N. Scarratt, J. Griffin, H. Yi, A. Iraqi, A. Buckley, J. Kingsley, D. Lidzey. The Role of the Hole-Extraction Layer in Determining the Operational Stability of a Polycarbazole: Fullerene Bulk-Heterojunction Photovoltaic Device. Applied Physics Letters, **106** (2015) 073301.

[4-6] I.P. Murray, S.J. Lou, L.J. Cote, S. Loser, C.J. Kadleck, T. Xu, J.M. Szarko, B.S. Rolczynski, J.E. Johns, J. Huang. Graphene Oxide Interlayers for Robust, High-Efficiency Organic Photovoltaics. The Journal of Physical Chemistry Letters, **2** (2011) 3006.

[4-7] M.F. Lo, T.W. Ng, S. Lai, M.K. Fung, S.T. Lee, C.S. Lee. Stability Enhancement in Organic Photovoltaic Device by Using Polymerized Fluorocarbon Anode Buffer Layer. Applied Physics Letters, **99** (2011) 033302.

[4-8] X. Hao, S. Wang, W. Fu, T. Sakurai, S. Masuda, K. Akimoto. Novel Cathode Buffer Layer of Ag-Doped Bathocuproine for Small Molecule Organic Solar Cell with Inverted Structure. Organic Electronics, **15** (2014) 1773.

[4-9] M.J. Tan, W-P. Goh, J. Li, G. Pundir, V. Chellappan, Z-K. Chen. Charge Mobility and Recombination in a New Hole Transporting Polymer and Its Photovoltaic Blend. ACS Applied Materials & Interfaces, **2** (2010) 1414.

[4-10] Y. Chen, J. Peng, D. Su, X. Chen, Z. Liang. Efficient and Balanced Charge Transport Revealed in Planar Perovskite Solar Cells. ACS Applied Materials & Interfaces, **7** (2015) 4471.

[4-11] B. Zhang, H. Yuan, X. Zhang, D. Huang, S. Li, M. Wang, Y. Shen. Investigation of Regeneration Kinetics in Quantum-Dots-Sensitized Solar Cells with Scanning Electrochemical Microscopy. ACS Applied Materials & Interfaces, **6** (2014) 20913.

[4-12] W. Tress, K. Leo, M. Riede. Influence of Hole-Transport Layers and Donor Materials on Open-Circuit Voltage and Shape of I-V Curves of Organic Solar Cells. Advanced Functional Materials, **21** (2011) 2140.

[4-13] Z. Li, C.R. McNeill. Transient Photocurrent Measurements of Pcdtbt: $PC_{70}BM$ and PCPDTBT: $PC_{70}BM$ Solar Cells: Evidence for Charge Trapping in Efficient Polymer/Fullerene Blends. Journal of Applied Physics, **109** (2011) 074513.

[4-14] X. Qiao, C. Zhao, B. Chen, L. Luan, B. Hu. In-Situ Investigation of Interfacial Effects on Charge Accumulation and Extraction in Organic Solar Cells Based on Transient Photocurrent Studies. Organic Electronics, **15** (2014) 1624.

[4-15] X. Hao, S. Wang, T. Sakurai, K. Akimoto. Effect of Bathocuproine Buffer Layer in Small Molecule Organic Solar Cells with Inverted Structure. Japanese Journal of Applied Physics, **54** (2015) 04DK06.

[4-16] J. Kim, S. Yim. Influence of Surface Morphology Evolution of SubPc Layers on the Performance of

SubPc/C_{60} Organic Photovoltaic Cells. Applied Physics Letters, **99** (2011) 193303.

[4-17] S. Morris, M. Shtein. High Efficiency Organic Photovoltaic Cells Based on Inverted Subpc/C_{60}/ITO Cascade Junctions. Organic Electronics, **15** (2014) 3795.

[4-18] W. Huang, E. Gann, Y-B. Cheng, C.R. McNeill. In-Depth Understanding of the Morphology-Performance Relationship in Polymer Solar Cells. ACS Applied Materials & Interfaces, (2015).

[4-19] K. Rajkanan, J. Shewchun. A Better Approach to the Evaluation of the Series Resistance of Solar Cells. Solid-State Electronics, **22** (1979) 193.

[4-20] M. Ichikawa, E. Suto, H-G. Jeon, Y. Taniguchi. Sensitization of Organic Photovoltaic Cells Based on Interlayer Excitation Energy Transfer. Organic Electronics, **11** (2010) 700.

[4-21] R. Könenkamp, G. Priebe, B. Pietzak. Carrier Mobilities and Influence of Oxygen in C_{60} Films. Physical Review B, **60** (1999) 11804.

[4-22] A. Tapponnier, I. Biaggio, P. Gunter. Ultrapure C_{60} Field-Effect Transistors and the Effects of Oxygen Exposure. Applied Physics Letters, **86** (2005) 112114.

[4-23] Q.D. Yang, T-W. Ng, M-F. Lo, F. Wang, N.B. Wong, C-S. Lee. Effect of Water and Oxygen on the Electronic Structure of the Organic Photovoltaic. The Journal of Physical Chemistry C, **116** (2012) 10982.

[4-24] W. Shockley, W. Read Jr. Statistics of the Recombinations of Holes and Electrons. Physical Review, **87** (1952) 835.

[4-25] V. Gupta, A.K.K. Kyaw, D.H. Wang, S. Chand, G.C. Bazan, A.J. Heeger. Barium: An Efficient Cathode Layer for Bulk-Heterojunction Solar Cells. Scientific Reports, **3** (2013).

[4-26] S.R. Cowan, A. Roy, A.J. Heeger. Recombination in Polymer-Fullerene Bulk Heterojunction Solar Cells. Physical Review B, **82** (2010) 245207.

[4-27] C.R. McNeill, I. Hwang, N.C. Greenham. Photocurrent Transients in All-Polymer Solar Cells: Trapping and Detrapping Effects. Journal of Applied Physics, **106** (2009) 024507.

Chapter 5 Study on Open Circuit Voltage of Small Molecule Bulk Devices

5.1 Introduction

Among the typically used donor organic semiconductor materials MPcs, the SubPc shows the highest V_{OC} while being used in OSCs, which makes it quite potential materials in the photovoltaic applications.[5-1,5-2] In the last 2 chapters, we mainly discussed the stability and interfacial modification of SubPc/C_{60} based small molecule OSCs with layered configuration. The J_{SC} was improved when an inverted device was constructed with BCP buffer from 3.8 to 4.7 mA/cm^2 while with an efficiency of merely 1.9 %. Basic research and device development on SubPc/C_{60} photovoltaic still have a long way to go to compete with the best researched OSCs, not to mention the inorganic solar cells. The limited J_{SC} for the bilayer devices is mainly due to the insufficient efficiency of exciton dissociation. Fortunately, one feasible approach to improve the J_{SC} is to construct a bulk device in which the donor and acceptor is well mixed to realize the efficient exciton dissociation and harvisting.[5-3~5-5]

The donor/acceptor interface is of great importance in a bulk device and in polymer devices, there have been focused studies involving polymer OSCs on the bulk layer morphology. The polymer based bulk devices are mainly fabricated by the most favored methodology of solution processing due to its advantages of simple process, cost-effective and also timesaving. In this case, the morphology can be affected by: the condition of solvents,[5-6,5-7] the effects caused by the annealing,[5-8~5-10] the selection of additives[5-11,5-12] and so on. On the contrary, for the small molecule devices, which were mainly fabricated by vacuum deposition, such morphological researches on the promising bulk device based on SubPc/C_{60} is still rare. In this chapter, we mainly studied the effects of the morphology on the V_{OC} of the bulk devices based on SubPc/C_{60}.

5.2 Experiment

The bulk devices with conventional and inverted architectures were fabricated by evaporating C_{60} and SubPc sources at certain rates simultaneously, and the composition of the bulk active layer was controlled by varying the deposition rates. The structure of the conventional device is ITO/MoO_3(30 nm)/SubPc:C_{60}(*wt.*% of SubPc=0.2, 70 nm)/BCP(10 nm)/Ag(100 nm) and the inverted device was achieve by depositing the active layers in a reversed sequence: BCP, SubPc:C_{60} and MoO_3, as shown in Fig. 5-1.The ITO substrates with different work function were utilized in this chapter to investigate the effect of electrodes work function on the device performance. The work function of ITO was varied by different chemical treatments, as introduced in the following part.

5.2.1 The work function modification of ITO

The work function of ITO is critical in affecting the related organic devices' performances by means of affecting the energy barrier height at the interface, the interaction with the organic materials and so on. The approaches of varying the work function of ITO is mainly on the surface treatment because the change of the composition of In, Sn, O and surface carbon will lead to the variation of surface electronic structure of ITO.[5-13,5-14] There are various treatments subjected to changing the work function of ITO, plasma treatment, surface etching, chemical modification and so on. In this work, ITO substrates were first

immersed sequentially in ultrasonic baths of acetone, ethanol and deionized water and then treated by O_2 plasma and ethoxylated polyethylenimine (known as PEIE) coating, in which the O_2 plasma treating will increase the work function and the latter will result in a decrease in the work function.

- O_2 plasma treating

The plasma cleaner used in this work was a 35×35 cm^2 in planar size and 25 cm tall stainless steel chamber connected with a rotary pump to exhaust air from the chamber. The inductive source was a planar copper coil which was connected to a rf generator. O_2 was fed into the chamber through a stainless-still shower ring positioned at the bottom. Firstly we put the cleaned ITO substrates into the plasma chamber and evacuated for 20 mins to reach a vacuum of 0.5 Pa. The O_2 was then fed at a flow rate of 10 mL/min and "cleaned" the chamber for another 20 mins. The rf generator was then started-up and the ITO substrates was treated for 10 mins each. The O_2 plasma treated ITO has a work function of 5.1 eV, as reported by Yu *et al.* [5-13,5-14]

- Chemical treating

PEIE (M_W=70,000 g/mol) and 2-methoxyethanol were purchased from Sigma-Aldrich. PEIE was diluted using 2-methoxyethanol to a weight concentration of 0.4%. The solution was then spin coated on top of ITO at a speed of 5000 r/min for 1 min. The ITO substrates coated with PEIE films were then annealed at 100 ℃ for 10 min in the ambient air. The thickness of the PEIE was determined approximately to be 10 nm. The work function of PEIE coated ITO was measured to be 3.1 eV.[5-15,5-16]

5.2.2 Device fabrication and characterization

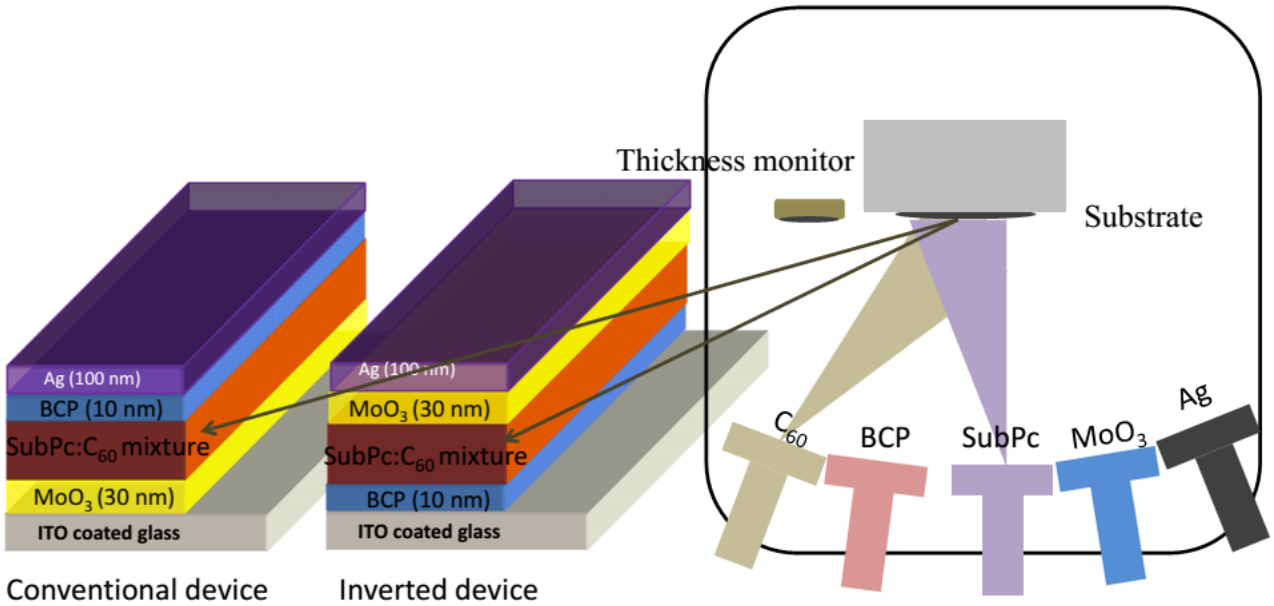

Fig. 5-1. Device structure of bulk OSC and the schematic of the bulk active preparation process.

All of the functional layers of both the conventional and inverted devices were deposited in the MBE vacuum chamber by thermal evaporation. The bulk active layer was prepared by evaporating the SubPc and C_{60} source materials simultaneously (Fig. 5-1). The composition of the active bulk layer was controlled by varying the deposition rate of the source materials by means of adjusting the heating temperature of the K-cell. The weight concentration of SubPc is given by: $wt\%\ SubPc = \frac{\rho_{SubPc} V_{SubPc}}{\rho_{SubPc} V_{SubPc} + \rho_{C60} V_{C60}}$, in which ρ_{SubPc}

and ρ_{C60} are the densities of SubPc and C_{60} while *V* stands for the volume, which is direct proportional to the deposition rate. The preparing parameters are summarized in Table 5-1. It should be noted that the parameters listed in this table are for the SubPc concentration of 20 *wt.*%, which has been confirmed to be the optimized composition in achieving the best performance in the conventional device. The optimization of the device performance will be discussed in details in 5.3.1.

Table 5-1 parameters for bulk device fabrication (20 *wt.*% SubPc)

	BCP	C_{60}	SubPc	MoO_3	Ag
Deposition rage (Å/s)	0.3	0.5	0.12	0.5	1.5
Thickness (nm)	10	70		30	100

After preparation, the devices were immediately moved out from the vacuum chamber and characterized under ambient condition without further encapsulation. The *J-V* curves, the *EQE*, GIXRD, AFM and TPC characteristics were then carried out. The setup of the characterization was described in Chapter 2.

5.3 Results and discussion

5.3.1 Performances optimization of conventional bulk device

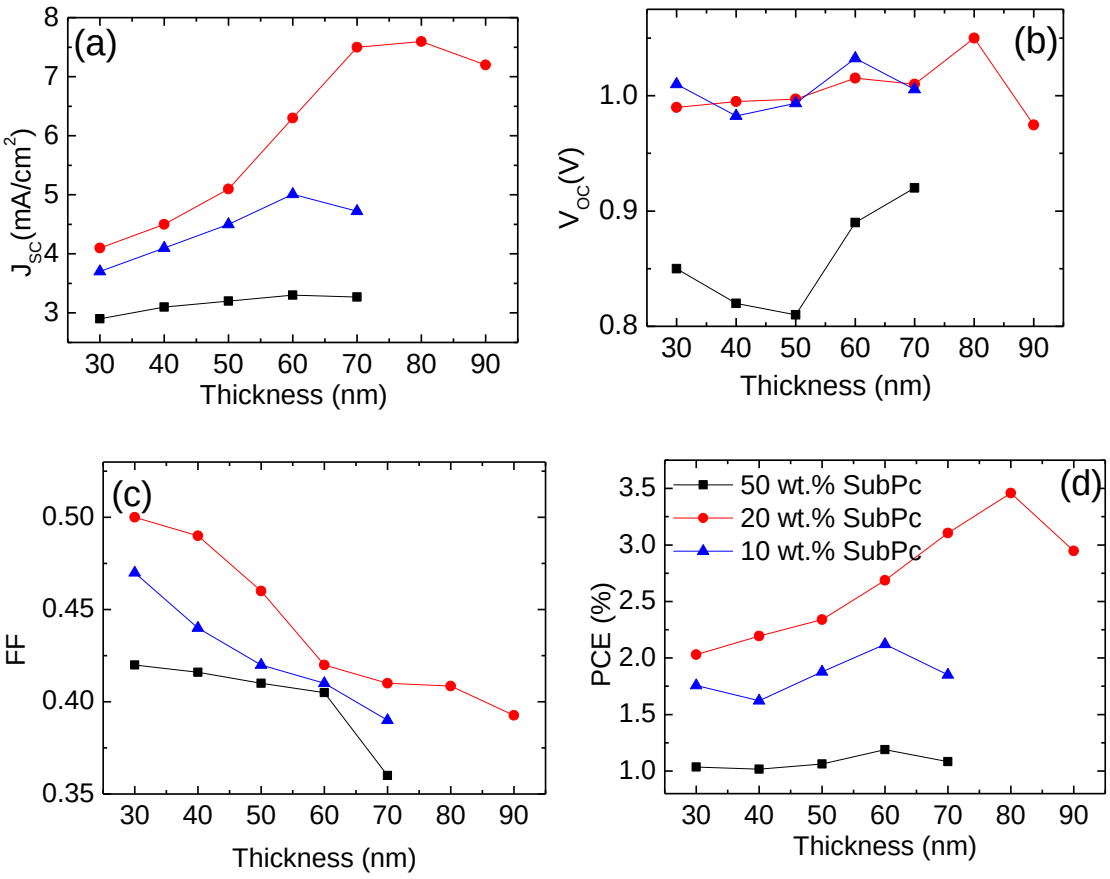

Fig. 5-2. Photovoltaic operating parameters for bulk devices containing 50 *wt.*% SubPc, 20 *wt.*% SubPc and

10 *wt.*% SubPc at 100 mW/cm^2 with respect to active layer thickness. (a) for the J_{SC}, (b) for the V_{OC}, (c) for the *FF* and (d) for the *PCE*.

The operating parameters for bulk devices containing 50 *wt.*%, 20 *wt.*% and 10 *wt.*% SubPc with conventional structure (see Fig. 5-1) as a function of the thickness of the active layer was shown in Fig. 5-2. The photovoltaic parameters of the device with as a function of concentration of SubPc in the active layer were compared in Fig. 5-2. The *FF* for all the devices decreases with the increased active layer thickness due to a reduction in the charge collection efficiency.[5-17] The C_{60} rich device shows a larger *FF* than that of the others. 20 *wt.*% SubPc device shows highest *FF* over all thickness, evidencing an improved charge transportation. With the increased thickness, J_{SC} increased to a peak and then decreased. For a device with certain thickness of the active layer, take the 70 nm thick active layer device as an example, as shown in Fig. 5-3, the absorbance indeed increased with the concentration of SubPc, while the charge transportation was limited by this concentration. The decrease is therefore due to the reduction in the charge collection efficiency and a saturation of the absorption efficiency.[5-18] V_{OC} does not show strong dependence on the concentrations of the concentration or the thickness of the active layer. That is because the utilization of BCP and MoO_3 layer to block the holes and electron from leakage so that ensure a low dark current for all the devices. The higher *FF* and J_{SC} for 20 *wt.*% SubPc device leads to a maximum *PCE* of 3.2% at the active layer thickness of 70 nm.

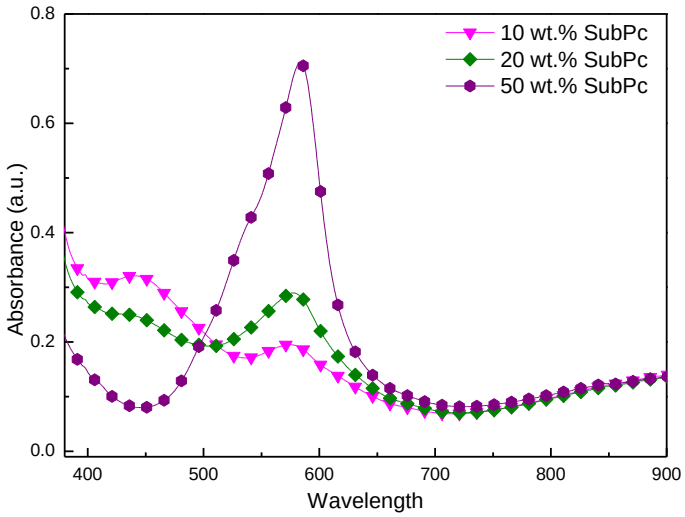

Fig. 5-3. The absorption spectra for 70 nm active layers with different concentrations.

The performance of the optimized bulk device and the bilayer device was compared in Fig. 5-4 with the parameters summarized in Table 5-2. The construction of a bulk device leads to a significant increase of J_{SC} by over 95%, which can be clearly observed in the *EQE* spectra shown in Fig. 5-5. In contrast, the bilayer device exhibits a higher *FF* as compared with the bilayer device. This is attributed to the reduced charge collection efficiency in the bulk device. Nevertheless, the overall efficiency was improved greatly by constructing a bulk device by using small molecules of SubPc and C_{60}.

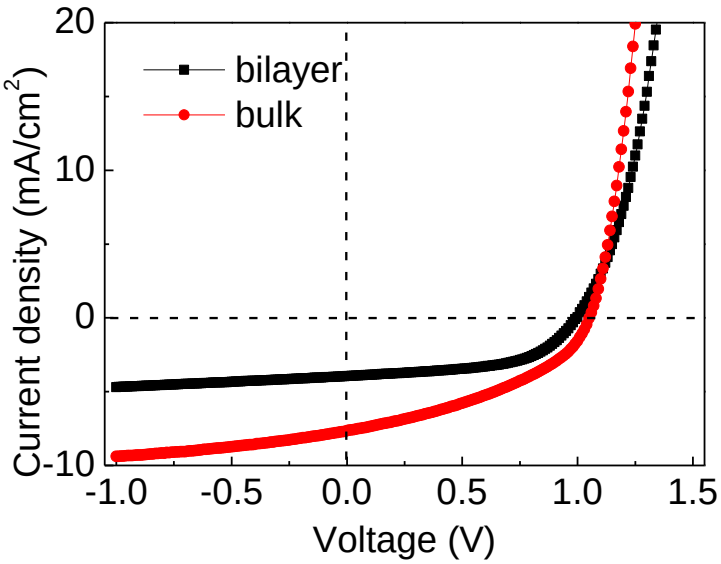

Fig. 5-4. Comparison of the *J-V* characteristics for bilayer and bulk devices with conventional architecture.

Table 5-2 Photovoltaic parameters of conventional devices with bilayer and bulk absorbers.

	J_{SC} (mA/cm^2)	V_{OC} (V)	*FF*	*PCE* (%)
Bilayer	3.8	1.02	0.49	1.9
Bulk	7.5	1.05	0.44	3.2

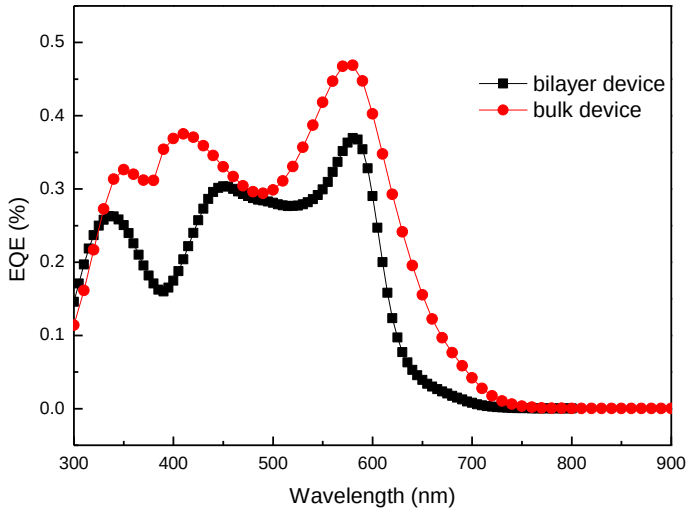

Fig. 5-5. The *EQE* spectra of device with bilayer and bulk architectures.

5.3.2 The performance of inverted bulk device

As discussed in the last chapter, due to the instability of C_{60}, after confirming the optimized preparation

parameters in the conventional device, we fabricated the inverted device to improve the device stability. The inverted device was fabricated by merely exchange the deposition sequence of MoO_3 and BCP and as a result, the functional layers of the devices are exactly the same (see Fig. 5-1). The *J-V* curve of inverted device shows a greatly decreased V_{OC} of merely 0.64 V while with comparative J_{SC} and *FF* as displayed in Table 5-3. The decrease of V_{OC} results in a significant reduction in the *PCE* by 60%.

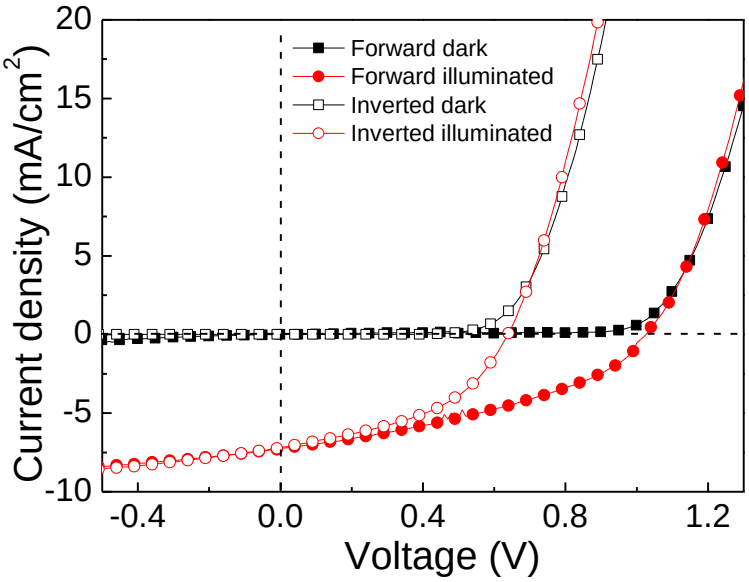

Fig. 5-6. The *J-V* curves of conventional and inverted bulk devices.

Table 5-3 Photovoltaic parameters of conventional devices with bilayer and bulk absorbers.

	J_{SC} (mA/cm^2)	V_{OC} (V)	*FF*	*PCE*(%)
Inverted device	7.2	0.64	0.40	2.0
Conventional device	7.5	1.05	0.44	3.2

5.3.3 The effect of work function of the electrode

It is generally accepted that the V_{OC} was determined by the energy difference between the HOMO energy of donor and LUMO energy of acceptor and affected by the difference of the work functions between the cathode and anode. [5-4,5-19~5-21] In our case, the decrased V_{OC} for inverted device may be affected by the work function variation in the cathode and anode. To verify the effect of work function of the electrodes on the V_{OC} of the small molecule devices, the conventional and inverted bulk devices with ITO electrodes by varying the work function.

The original ITO without any treatment has a work function of 4.6 eV. First of all, we fabricated inverted device with PEIE treated ITO as cathode. As shown in the level alignment in Fig. 5-7 (e), the decrease of the work function in ITO is expected to be beneficial for the charge extraction at the cathode domain while surprisingly we got a *J-V* curve (Fig. 5-8 and Table 5-4) that almost not affected by the change in the work function. Just for comparison, we then fabricate an inverted device by using the O_2 plasma treated ITO as cathode. Due to the increased work function of ITO, an electron barrier as high as 1.6 eV was

established. The result turned out to be, the same as that of the PEIE treated ITO device, not affected by the greatly increased work function of the cathode, that is, the energy difference between the cathode and anode.

The fabrication and characterization of conventional devices by using ITO with varied work functions were then carried out as controls. Not just for V_{OC}, the photovoltaic parameters, the J_{SC} and FF, of the conventional devices also were demonstrated to be independent on the work function of the anode. This phenomenon is quite interesting while we cannot explain at present and one subject of the future work.

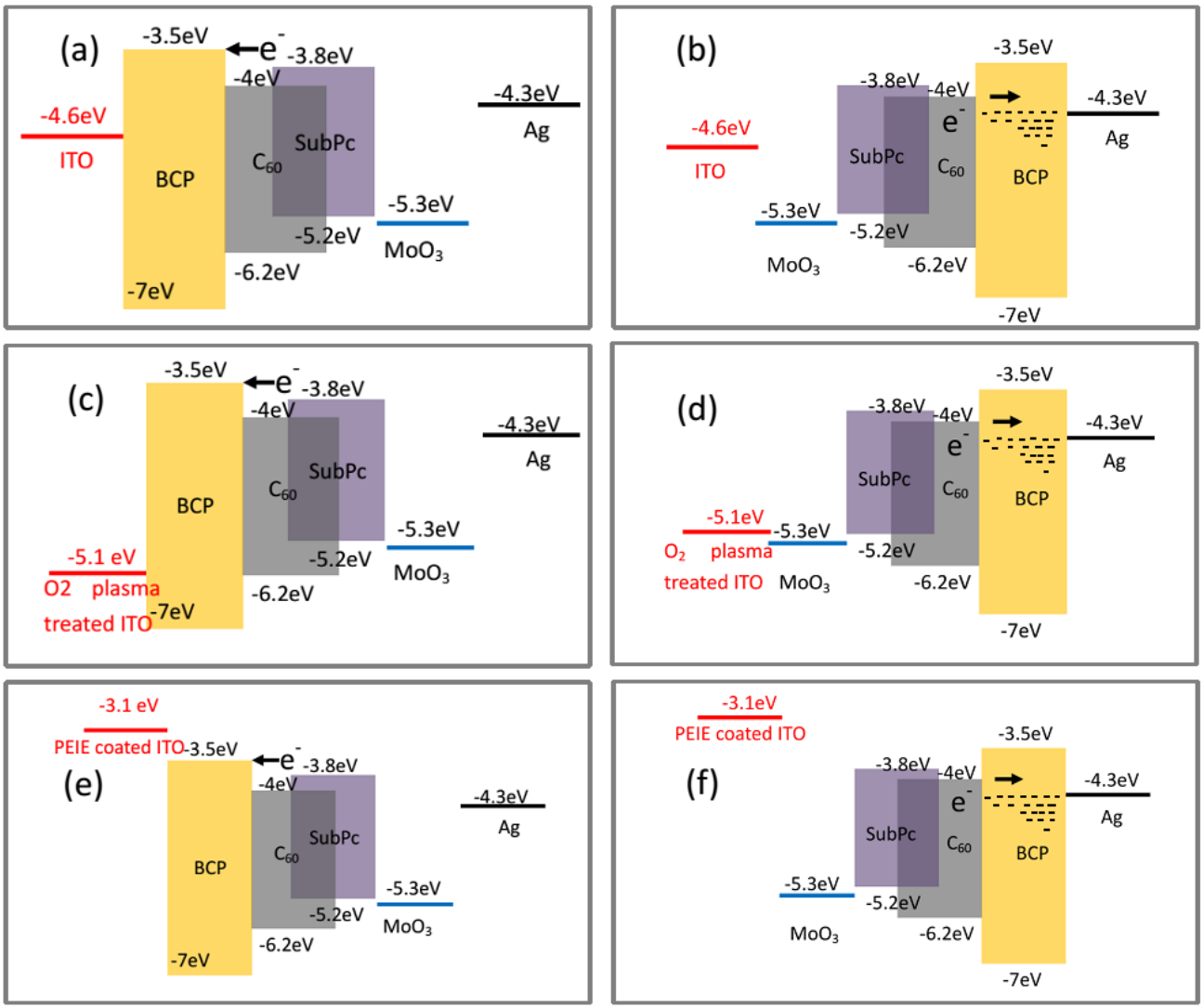

Fig. 5-7. Schematics of level alignment for bulk devices fabricated by using ITO treated by plasma and PEIE. (a), (c) and (e) are for inverted device and (b), (d) and (e) are for the conventional devices; Inverted and conventional devices with original ITO ((a) and (b)), plasma treated ITO ((c) and (d)) and PEIE treated ITO ((e) and (f))as cathodes and anodes, respectively.

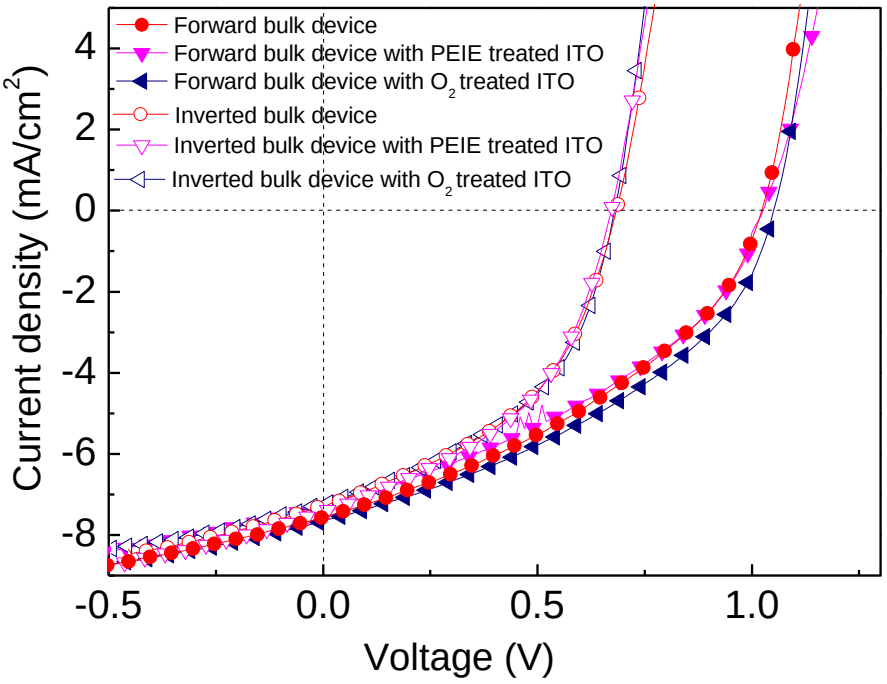

Fig. 5-8. The *J-V* characteristics with modified ITO as electrodes.

Table 5-4 The operating parameters of the devices shown in Fig. 5-8.

	Work function of ITO (eV)	J_{SC} (mA/cm^2)	V_{OC} (V)	*FF*	*PCE* (%)
Inverted device	4.6	7.2	0.64	0.40	2.0
	3.1	7.3	0.64	0.42	1.9
	5.1	7.2	0.63	0.41	1.8
Conventional device	4.6	7.5	1.03	0.44	3.2
	3.1	7.3	1.02	0.45	3.3
	5.1	7.7	1.05	0.44	3.2

*The work function of ITO treated by PEIE comes from *Refs.*[5-15,5-16] and that of O_2 plasma treated ITO from refs [5-14,5-22]

5.3.4 The effect of dark current

Since the V_{OC} was not affect by the work function variation, we then consider the influence of the dark current (J_S) since it correlated with the V_{OC} by : [5-23]

$$V_{OC} = \frac{nkT}{q}\ln\left[\frac{J_{ph}(V_{OC})}{J_s} + 1 - \frac{V_{OC}}{R_P J_s}\right] \quad (5\text{-}1)$$

The dark *J*-*V* of inverted and conventional bulk devices was illustrated in Fig. 5-9. The dark *J*-*V* curves yield 7.47×10^{-7} and 3.92×10^{-9} A/cm^2 of J_S for inverted and conventional bulk devices, respectively. The increased dark current by over two orders in the magnitude, in inverted device, as compared with that of the conventional one, was then speculated to be the main cause of the decreased V_{OC}. As aforementioned, the current leakage has been ruled out due to the use of MoO_3 and BCP blocking layers.

The V_{OC} of organic bulk device also correlates with the charge densities by:[5-24~5-26]

$$V_{OC} = \frac{E_g}{q} - \frac{kT}{q}\ln\left(\frac{N_{eff}^2}{np}\right), \quad (5\text{-}2)$$

where E_g is the energy difference of the HOMO energy level of donor and LUMO energy level of acceptor, q is the elementary charge, k is the Boltzmann constant, n and p are hole and electron densities. The charge densities are directly proportional to the recombination, and Eq. 5-2 suggested that the V_{OC} correlate with the recombination and the decreased n (p) means decreased V_{OC}.

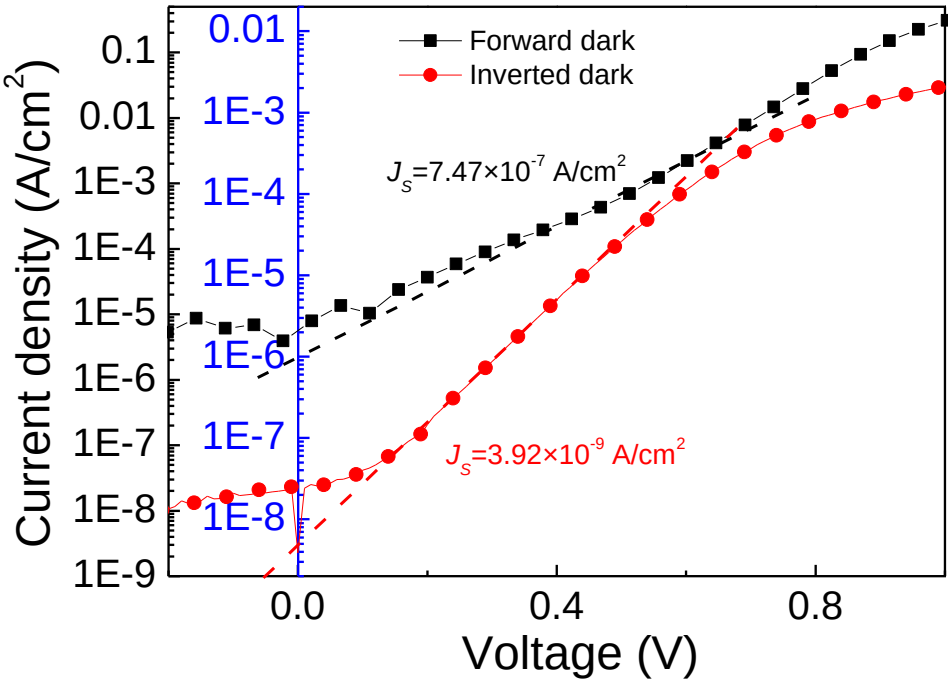

Fig. 5-9. Dark characteristics for the conventional and inverted bulk devices.

5.3.4 Morphologies of the active layers

For polymer bulk OSCs, the performance is strongly dependent on the morphology of the active layer.[5-7,5-8,5-11,5-27~5-29] While in case of the small molecule devices, the molecular orientation is of

great importance in affecting the electronic states of organic material, charge transport and as a result the performance of the related devices.[5-28~5-31] Although it has been verified that the decreased V_{OC} in inverted bulk device was originated from the aggravation of the recombination in, we are not aware of the mechanism. To get further insight into the origination of the decreased V_{OC} in inverted device, the molecular orientation and morphology of the active layer was examined.

The molecular orientation was investigated by measuring the GIXRD of 70 nm SubPc:C_{60} (20 wt.% SubPc) deposited on 30 nm MoO_3 and 10 nm BCP coated ITO substrates, which represent the conventional and inverted device, respectively. As shown in Fig. 5-10, the GIXRD patterns for SubPc and C_{60} deposited on ITO bare substrate were also shown for comparison. The C_{60} shows 3 diffraction peaks approximately around 10.9 °, 17.2 ° and 19.3 °. When the single SubPc shows 4 peaks located at 9.5 °, 19.2 °, 20.3 ° and 2.52 °. The diffraction patterns for nano-crystal thin layer of SubPc:C_{60} overlapped with each other exactly. This suggests that the altering of the underneath buffer does not change the orientation of the active layer.[5-32] The diffraction pattern with higher intensities for mixed active layer is mainly due to the larger thickness. The diffraction peaks of the bulk active layer reflecting the nano-crystal of C_{60} suggests that the "main body" of the active layer is composed of the ordered arranged C_{60} molecules with SubPc molecules dispersedly piled into the intervals between the C_{60} particles.

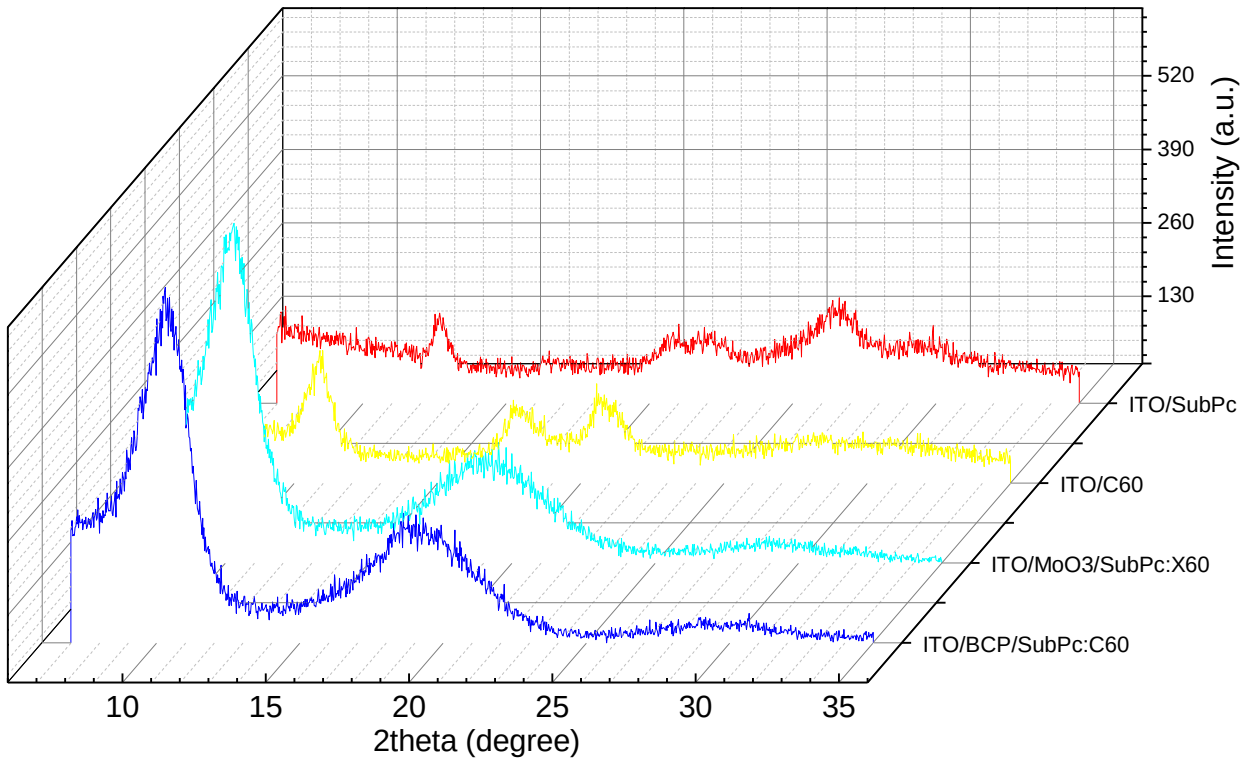

Fig. 5-10. GIXRD of ITO/SubPc (30 nm), ITO/C_{60} (30 nm), ITO/MoO_3 (30 nm)/SubPc:C_{60} (70 nm) and ITO/BCP (10 nm)/SubPc:C_{60} (70 nm).

We then measured the surface morphology of BCP and MoO_3 buffers as well as the active materials deposited on top of them. Fig. 5-11 presents the topographies of these thin films. The root mean square

(RMS) roughness values of BCP (Fig. 5-11 (a)) MoO_3 (Fig. 5-11(b)) on ITO substrate and of blended SubPc:C_{60} on 10 nm BCP (Fig. 5-11(c)) and 30 nm MoO_3 (Fig. 5-11(d)) coated ITO are 1.26, 1.47, 4.75 and 1.18 nm, respectively. Although the topographies for BCP and MoO_3 show similar morphologies, their effect on the subsequent deposited bulk layer is huge. The blend film deposited on MoO_3 shows a compact and uniform surface, which is composed of grains with ~200 nm grain size, while that on BCP is not so uniform, composed of larger grains with clear grain boundaries. The larger RMS value for film deposited on BCP also suggested the rough surface and interfaces of the grains.

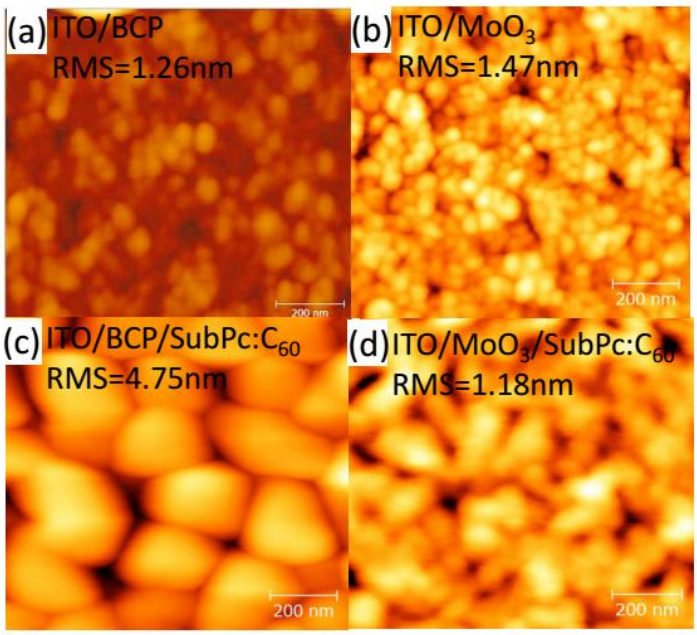

Fig. 5-11. The surface morphologies of different films on the scan range of 5×5 μm^2: (a) ITO/BCP (10 nm), (b) ITO/MoO_3 (30 nm), (c)ITO/BCP (10 nm)/SubPc:C_{60} (70 nm)and (d) ITO/MoO_3 (30 nm)/SubPc:C_{60} (70 nm).

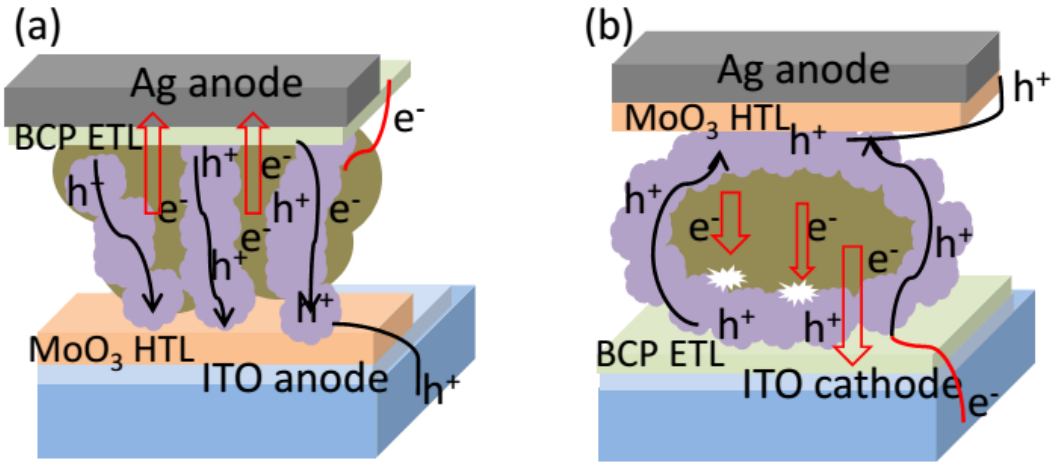

Fig. 5-12. Possible stacking models for (a) conventional device and (b) inverted device.

Fig. 5-12 illustrates the possible stacking patterns of the SubPc and C_{60} molecules in active layer in the conventional and inverted devices, based on the results of the GIXRD and AFM. The aggravation of the

recombination in the inverted device is very likely to be resulted from the extensive phase segregation, as shown in Fig. 5-12(b). Every separated particle of the SubPc and C_{60} molecules mixture directly contact with buffers and transport charges towards the electrodes acts as a small cell. The almost closed system of the single cells provides extra recombination paths for the electrons and holes in this particle. In contrast, for the conventional devices, an interpenetrating net work as well as moderated phase segregation was accomplished, as shown in Fig. 5-12(a). Such morphology and grain stacking may facilitate the charge excitons dissociation as well as the sweep out of photogenerated charges and as a result, leads to a reasonable V_{OC}.

5.3.6 Recombination mechanism

The recombination mechanisms of inverted devices were investigated by measuring the TPC characteristics, as shown in Fig. 5-13. The TPC traces for conventional and inverted bulk devices as a function of incident pulse intensity was illustrated. The TPC for inverted device is shown in Figs. 5-13(c) and 5-13(d), from which we can tell that not like the TPC of heavily degraded bilayer device discussed in Chapter 4, the TPC for inverted bulk device shows an intrinsic threshold in turn-on dynamic, evidenced by the appearance of a peak after turn-on, even at the lowest incident light intensity.

The TPC curve for the inverted bulk device composed of a slow rise after turn-n which gradually increases to the peak value and decreases slowly until reaching the equilibrium and a slow decay after turn-off with a long positive tail. The shape of the TPC for inverted bulk device was quite similar with that of the heavily degraded conventional bilayer device with three slightly differences:

1) Slower primary rise after turn-on: the TPC signal rises to its peak value at time range of ~50 μs, this is an evidence of decreased conductivity of the active materials;

2) Larger peak width: larger peak width means the slower rise and decay (~ 100-120μs) in the TPC traces in the turn-on behavior, which suggested slower transport of the mobile charges in the device;

3) Stronger dependence on the incident light intensity: the threshold in the turn-on behavior becomes prominent and the relative altitude increases with the increase of the light intensity.

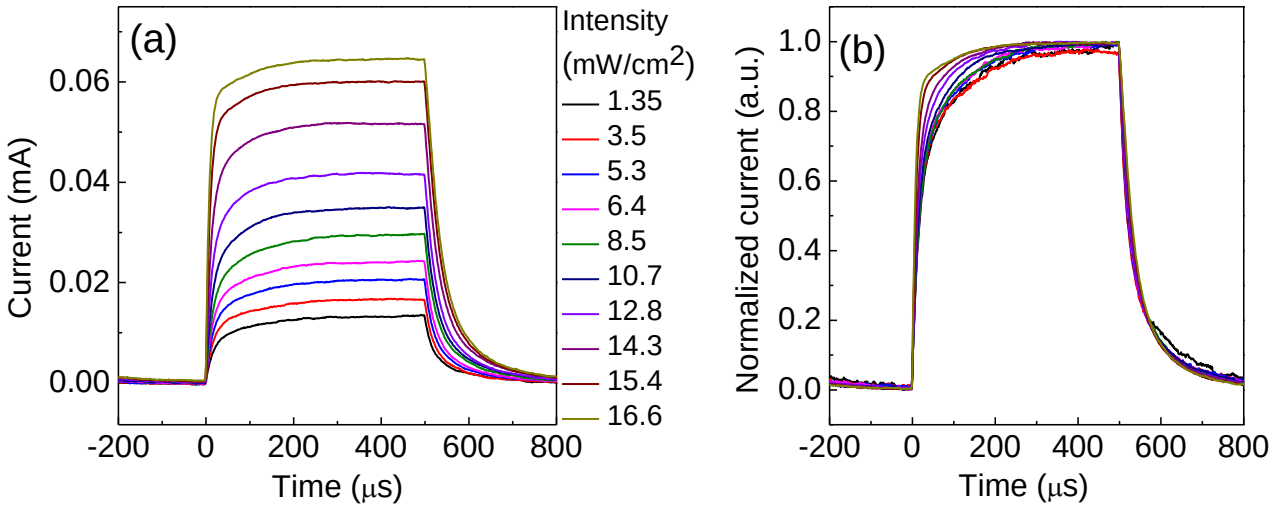

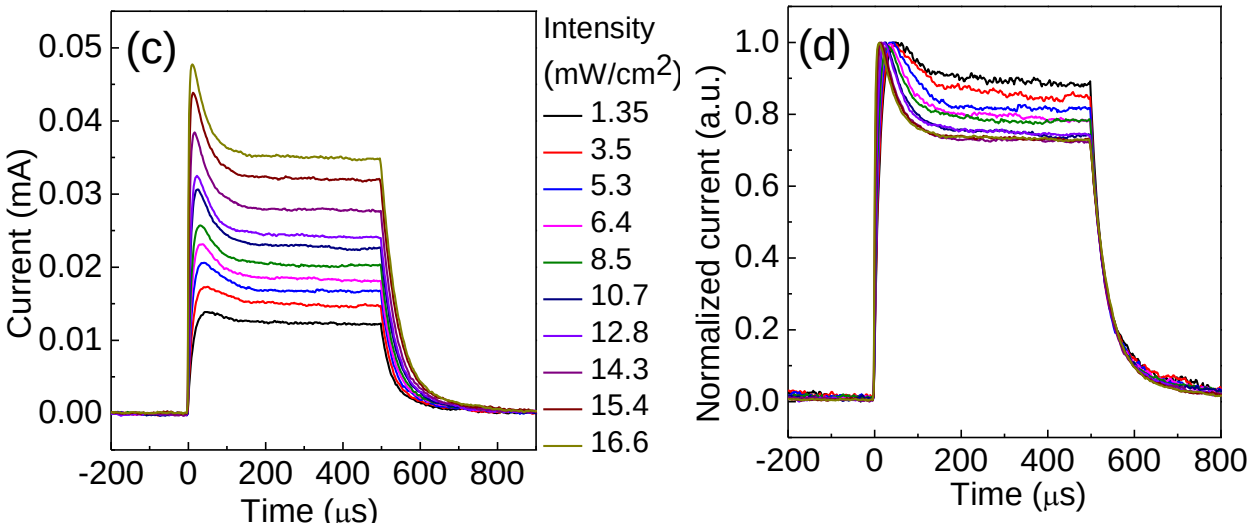

Fig. 5-13. TPC for conventional and inverted bulk devices: (a) and (b) are for conventional device while (b) and (d) are for inverted device; (a) and (c) stand for the absolute traces when (b) and (d) represent the normalized traces.

As for the conventional devices, the TPC was composed of a slow rise that gradually increased to a stable value after turn-on and a monotonically decrease to the 0 after turn-off, with a long-live positive tail. The TPC of conventional device shows obvious incident pulse intensity dependence, especially for the turn-on behavior. The incident pulse intensity dependent turn-on behaviors for both the devices reflect the presence of the inactivated triplet states in the bulk layer. The inactivated triplet states will then act as traps and involve in the recombination. The charge densities were eventually decreased and the lower V_{OC} was then observed in the inverted device. And the strong incident pulse intensity dependent TPC is also consistent with the larger intrinsic trap density in the bulk devices. The light intensity dependent turn-on behavior combined with a light intensity independent turn-off dynamic suggests a combination of charge trapping and recombination in inverted device.

Further insight into the recombination mechanism was obtained by measuring the light intensity dependent J_{SC} and calculating the amount of the extracted charges. The charge recombination kinetics at short circuit for devices with conventional and inverted architectures can be investigated by the J_{SC} vs light intensity (I). The J_{SC} correlated to I by the following formula:

$$J_{SC} \propto I^{\alpha}(\alpha \leq 1), \tag{5-3}$$

where I is the incident light intensity and α is the fitting value.

The bimolecular recombination should be minimum (α≈1) for the maximum carrier sweep-out. Therefore, any deviation from α≈1 implies the bimolecular recombination.[5-27,5-33,5-34] J_{SC} *vs.* I on log-log scale is shown in Fig. 5-14. It was fitted by the power law described above. The fitting of the data yield α=0.94 for conventional device, which can be attributed to bimolecular recombination. In the case of transient peak J_{SC} (red circles) device, after exponential power law fitting, α is 0.89, which implies an aggravation of bimolecular recombination. When the stable J_{SC} for the inverted device with an exponential fitting value of α=0.8, suggests a further aggravation of recombination.

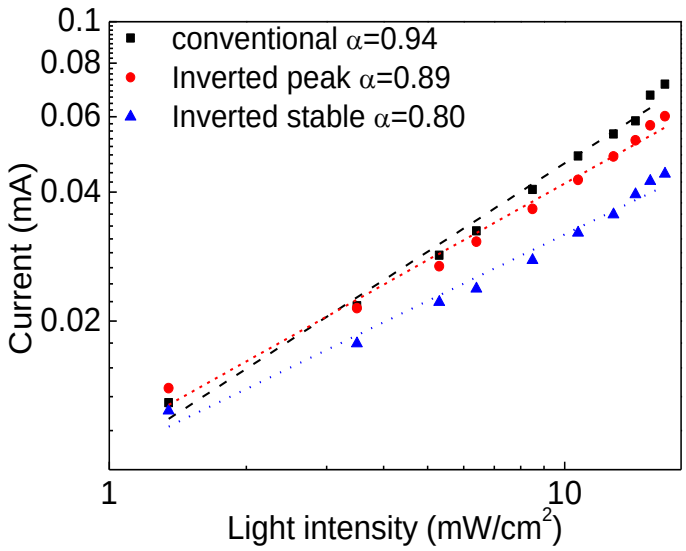

Fig. 5-14. J_{SC} of devices of bulk conventional and inverted devices plotted against light intensity (symbol) on the logarithmic scale. The fitted power law (line) yields α.

The amount of extracted charges was calculated by integrating the TPC after turn-off and the results are shown in Fig. 5-15. It is easy to understand that if the J_{SC} and light intensity linearly correlated with each other on a log-log scale, their integration on the time will show the similar correlations without extra loss in J_{SC}. That it:

$$Q \propto I^{\alpha} \ (\alpha \leq 1). \tag{5-4}$$

Here I is the incident light intensity and α is the fitting value.

The amount of the extracted charges in conventional and inverted bulk devices as a function of incident pulse intensity was shown in Fig. 5-15. The linear fitting for the conventional device shows a fitting value α=0.83. In contrast, the extracted charge quantity shows a more complex nonlinear dependence on the incident pulse intensity, which verified the aggravation of recombination in the inverted device.

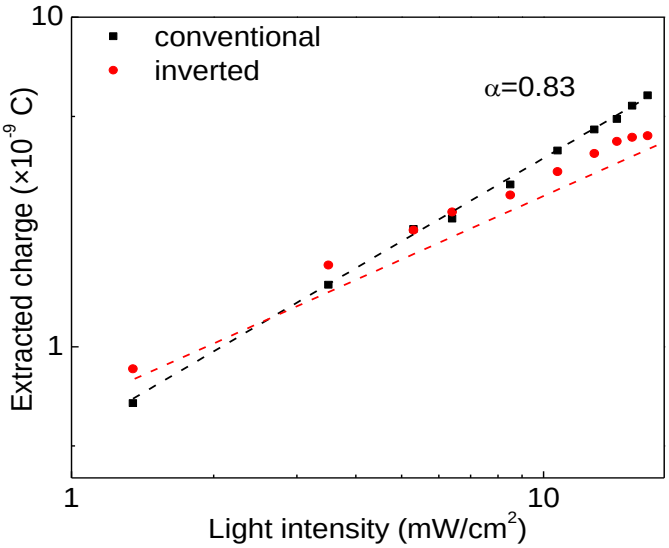

Fig. 5-15. The amount of extracted charges as a function of light intensity. The conventional device was well

fitted by Eq. 5-4 while the inverted one shows more complex dependence.

5.4 Summary

This chapter mainly studied the factors that affect the V_{OC} of the small molecule bulk devices. The result suggested that the morphology of the blend active layer is of great importance in influencing V_{OC}. To get higher V_{OC}, a finer morphology of active layer with interpenetrating interface of donor and acceptor molecules as well as the moderate phase segregation is required. The decreased V_{OC} of the inverted device was ascribed to due to the aggravation of recombination via extra recombination paths that originates from the extensive phase segregation.

References

[5-1] K.L. Mutolo, E.I. Mayo, B.P. Rand, S.R. Forrest, M.E. Thompson. Enhanced Open-Circuit Voltage in Subphthalocyanine/C_{60} Organic Photovoltaic Cells. Journal of the American Chemical Society, **128** (2006) 8108.

[5-2] H. Frohne, S.E. Shaheen, C.J. Brabec, D.C. Müller, N.S. Sariciftci, K. Meerholz. Influence of the Anodic Work Function on the Performance of Organic Solar Cells. ChemPhysChem, **3** (2002) 795.

[5-3] C.J. Brabec, G. Zerza, G. Cerullo, S. De Silvestri, S. Luzzati, J.C. Hummelen, S. Sariciftci. Tracing Photoinduced Electron Transfer Process in Conjugated Polymer/Fullerene Bulk Heterojunctions in Real Time. Chemical Physics Letters, **340** (2001) 232.

[5-4] M.C. Scharber, D. Mühlbacher, M. Koppe, P. Denk, C. Waldauf, A.J. Heeger, C.J. Brabec. Design Rules for Donors in Bulk-Heterojunction Solar Cells-Towards 10% Energy-Conversion Efficiency. Advanced Materials, **18** (2006) 789.

[5-5] S.H. Park, A. Roy, S. Beaupre, S. Cho, N. Coates, J.S. Moon, D. Moses, M. Leclerc, K. Lee, A.J. Heeger. Bulk Heterojunction Solar Cells with Internal Quantum Efficiency Approaching 100%. Nature Photonics, **3** (2009) 297.

[5-6] C.N. Hoth, P. Schilinsky, S.A. Choulis, C.J. Brabec. Printing Highly Efficient Organic Solar Cells. Nano Letters, **8** (2008) 2806.

[5-7] J. Liu, Y. Shi, Y. Yang. Solvation-Induced Morphology Effects on the Performance of Polymer-Based Photovoltaic Devices. Advanced Functional Materials, **11** (2001) 420.

[5-8] W. Ma, C. Yang, X. Gong, K. Lee, A.J. Heeger. Thermally Stable, Efficient Polymer Solar Cells with Nanoscale Control of the Interpenetrating Network Morphology. Advanced Functional Materials, **15** (2005) 1617.

[5-9] G. Li, V. Shrotriya, Y. Yao, Y. Yang. Investigation of Annealing Effects and Film Thickness Dependence of Polymer Solar Cells Based on Poly (3-Hexylthiophene). Journal of Applied Physics, **98** (2005) 043704.

[5-10] V.D. Mihailetchi, H. Xie, B. de Boer, L.A. Koster, P.W. Blom. Charge Transport and Photocurrent Generation in Poly (3-Hexylthiophene): Methanofullerene Bulk-Heterojunction Solar Cells. Advanced Functional Materials, **16** (2006) 699.

[5-11] F. Zhang, K.G. Jespersen, C. Bjoerstroem, M. Svensson, M.R. Andersson, V. Sundström, K. Magnusson, E. Moons, A. Yartsev, O. Inganäs. Influence of Solvent Mixing on the Morphology and Performance of Solar Cells Based on Polyfluorene Copolymer/Fullerene Blends. Advanced Functional Materials, **16** (2006) 667.

[5-12] J. Peet, J. Kim, N.E. Coates, W.L. Ma, D. Moses, A.J. Heeger, G.C. Bazan. Efficiency Enhancement in Low-Bandgap Polymer Solar Cells by Processing with Alkane Dithiols. Nature Materials, **6** (2007) 497.

[5-13] Y. Park, V. Choong, Y. Gao, B. Hsieh, C. Tang. Work Function of Indium Tin Oxide Transparent Conductor Measured by Photoelectron Spectroscopy. Applied Physics Letters, **68** (1996) 2699.

[5-14] H. Yu, X. Feng, D. Grozea, Z. Lu, R. Sodhi, A. Hor, H. Aziz. Surface Electronic Structure of Plasma-Treated Indium Tin Oxides. Applied Physics Letters, **78** (2001) 2595.

[5-15] X. Yang, R. Wang, C. Fan, G. Li, Z. Xiong, G.E. Jabbour. Ethoxylated Polyethylenimine as an Efficient Electron Injection Layer for Conventional and Inverted Polymer Light Emitting Diodes. Organic Electronics, **15** (2014) 2387.

[5-16] Y. Zhou, C. Fuentes-Hernandez, J. Shim, J. Meyer, A.J. Giordano, H. Li, P. Winget, T. Papadopoulos,

H. Cheun, J. Kim. A Universal Method to Produce Low-Work Function Electrodes for Organic Electronics. Science, **336** (2012) 327.

[5-17] H. Benten, M. Ogawa, H. Ohkita, S. Ito. Design of Multilayered Nanostructures and Donor-Acceptor Interfaces in Solution-Processed Thin-Film Organic Solar Cells. Advanced Functional Materials, **18** (2008) 1563.

[5-18] R. Pandey, R.J. Holmes. Graded Donor‐Acceptor Heterojunctions for Efficient Organic Photovoltaic Cells. Advanced Materials, **22** (2010) 5301.

[5-19] H-Y. Chen, J. Hou, S. Zhang, Y. Liang, G. Yang, Y. Yang, L. Yu, Y. Wu, G. Li. Polymer Solar Cells with Enhanced Open-Circuit Voltage and Efficiency. Nature Photonics, **3** (2009) 649.

[5-20] V. Mihailetchi, P. Blom, J. Hummelen, M. Rispens. Cathode Dependence of the Open-Circuit Voltage of Polymer: Fullerene Bulk Heterojunction Solar Cells. Journal of Applied Physics, **94** (2003) 6849.

[5-21] K. Kawano, N. Ito, T. Nishimori, J. Sakai. Open Circuit Voltage of Stacked Bulk Heterojunction Organic Solar Cells. Applied Physics Letters, **88** (2006) 073514.

[5-22] K.H. Lee, H.W. Jang, K-B. Kim, Y-H. Tak, J-L. Lee. Mechanism for the Increase of Indium-Tin-Oxide Work Function by O_2 Inductively Coupled Plasma Treatment. Journal of Applied Physics, **95** (2004) 586.

[5-23] N. Li, B.E. Lassiter, R.R. Lunt, G. Wei, S.R. Forrest. Open Circuit Voltage Enhancement Due to Reduced Dark Current in Small Molecule Photovoltaic Cells. Applied Physics Letters, **94** (2009) 023307.

[5-24] D. Cheyns, J. Poortmans, P. Heremans, C. Deibel, S. Verlaak, B. Rand, J. Genoe. Analytical Model for the Open-Circuit Voltage and Its Associated Resistance in Organic Planar Heterojunction Solar Cells. Physical Review B, **77** (2008) 165332.

[5-25] L. Koster, E. Smits, V. Mihailetchi, P. Blom. Device Model for the Operation of Polymer/Fullerene Bulk Heterojunction Solar Cells. Physical Review B, **72** (2005) 085205.

[5-26] L.J.A. Koster, V.D. Mihailetchi, R. Ramaker, P.W. Blom. Light Intensity Dependence of Open-Circuit Voltage of Polymer: Fullerene Solar Cells. Applied Physics Letters, **86** (2005) 123509.

[5-27] J.K. van Duren, X. Yang, J. Loos, C.W. Bulle-Lieuwma, A.B. Sieval, J.C. Hummelen, R.A. Janssen. Relating the Morphology of Poly (P-Phenylene Vinylene)/Methanofullerene Blends to Solar-Cell Performance. Advanced Functional Materials, **14** (2004) 425.

[5-28] C. Mattheus, W. Michaelis, C. Kelting, W. Durfee, D. Wöhrle, D. Schlettwein. Influence of the Molecular Shape on the Film Growth of a Substituted Phthalocyanine. Synthetic Metals, **146** (2004) 335.

[5-29] I.A. Howard, R. Mauer, M. Meister, F. Laquai. Effect of Morphology on Ultrafast Free Carrier Generation in Polythiophene: Fullerene Organic Solar Cells. Journal of the American Chemical Society, **132** (2010) 14866.

[5-30] C.G. Claessens, D. González-Rodríguez, T. Torres. Subphthalocyanines: Singular Nonplanar Aromatic Compounds Synthesis, Reactivity, and Physical Properties. Chemical Reviews, **102** (2002) 835.

[5-31] J. Kim, S. Yim. Influence of Surface Morphology Evolution of SubPc Layers on the Performance of SubPc/C_{60} Organic Photovoltaic Cells. Applied Physics Letters, **99** (2011) 193303.

[5-32] K. Miyazawa, Y. Kuwasaki, A. Obayashi, M. Kuwabara. C_{60} Nanowhiskers Formed by the Liquid–Liquid Interfacial Precipitation Method. Journal of Materials Research, **17** (2002) 83.

[5-33] I. Riedel, J. Parisi, V. Dyakonov, L. Lutsen, D. Vanderzande, J.C. Hummelen. Effect of Temperature and Illumination on the Electrical Characteristics of Polymer-Fullerene Bulk-Heterojunction Solar Cells. Advanced Functional Materials, **14** (2004) 38.

[5-34] P. Schilinsky, C. Waldauf, C.J. Brabec. Recombination and Loss Analysis in Polythiophene Based Bulk Heterojunction Photodetectors. Applied Physics Letters, **81** (2002) 3885.

Chapter 6 Main Results and Further Tasks

- **Main results**

The effect of charge trapping and recombination in small molecule organic solar cells was systematically studied in inverted bilayer devices, in aged devices as well as in small molecule bulk devices.

To optimize the performance of inverted device, a BCP cathode buffer layer was inserted between the ITO cathode and the C_{60} active layer. An improvement of ~60% in the *PCE* of the inverted device was witnessed. The significant improvement in *PCE* of BCP device and the roles of the BCP buffer layer in inverted OSCs were clarified. The obvious quench in the PL spectrum for ITO/C_{60} suggests that the excitons generated in C_{60} layer dissociated and recombined at the ITO/C_{60} interface. The insertion of BCP prevents the direct contact of ITO and C_{60} so that eliminate the excitons quenching and resulted in an obvious increase in the J_{SC}. The charge behavior of both the devices was examined by TPV and TPC. The faster rise time in the TPV for BCP device suggests less trapping while the loss in the amount of extracted charge in device free of BCP suggests an aggravation of the trap-assisted recombination. Also the measurements of light intensity dependent J_{SC} and V_{OC} are consistent with the results of the transient measurements. The effects of the BCP in an inverted small molecule OSC is: blocking the excitons, eliminating the generation of trap states by prohibiting the direct contact of ITO/C_{60} and suppressing trap-assisted recombination.

Besides the performance limitation, the short lifetime is another obstacle that hinders the development of OSCs. The degradation mechanism of C_{60}-based small molecule OSCs of conventional and inverted structure with identical cathode and anode buffer layers was investigated by using TPC measurement. For the conventional device, it only takes 20 hours for the *PCE* to decay to 50% of its initial value. The appearance of a peak in after turn-on behavior and the pulse intensity independence of turn-off dynamics in the TPC for the heavily degraded conventional device are ascribed to the aggravation of the trap mediated recombination after exposure to the air ambient. In contrast, the stability of the inverted device was improved greatly, with a half-lifetime of over 480 hours. The absent of a threshold in the turn-on dynamics and a pulse intensity dependent turn-off trace in the TPC implies that the trap mediated recombination was significantly suppressed in the inverted structure. This study demonstrates fast degradation mechanism of the conventional device, and provides directions in improving the device stability.

In the last part, we discussed the factors that affect the V_{OC} in the small molecule bulk devices. The results suggested that the morphology of the blend active layer is of great importance in influencing V_{OC}. To get high V_{OC}, a finer morphology of active layer with interpenetrating interface of donor and acceptor molecules as well as the moderate phase segregation is required. The decreased V_{OC} of the inverted device was ascribed to due to the aggravation of recombination via extra recombination paths that originates from the extensive phase segregation.

In conclusion, the device performance is strongly related to the charge trapping and recombination. Charge trapping is a common phenomenon in organic solar cells. On the one hand, in case of bilayer devices, other than charge trapping, the presence of trap states is very likely to be involved in recombination process and cause energy loss in devices. Improving the fabrication technique to eliminate generation of traps and charge trapping is effective in optimizing the performance of bilayer devices. On the other hand, for small molecule bulk devices, the effect of charge trapping is not so evident. The critical factor that determines the device performance is the morphology of the active layer, which directly related to the recombination procedure. This study is beneficial for the optimization of small molecule OSCs and has significant

implications for improving the long term stability of OSCs.

- **Further tasks**

Although the inverted planar device shows an improved stability of more than 10 times than that of the conventional one, the t_{50} for the inverted device is still below 1000 hours. This suggests that other than the energy loss that induced by the recombination, there must be other issues that exist in the donor/acceptor region to affect the charge injection, transportation, dissociation and so on. We may induce from the aging time dependent photovoltaic performance of the inverted device that, with the increased aging time, aggravated recombination can also be also observed in the inverted device. Therefore, one of the subjects for the future work is to clarify the nature of the short lifetime of the OSC, which may lie in the deterioration of the organic materials themselves or the degradation of the interfaces (organic/organic, organic/transport material, buffer/electrode).

The results of small molecule bulk devices in our work suggest that in the bulk devices with reversed cell structure, the V_{OC} is determined by the morphology of the active materials. Another subject for the future work is to figure out the influencing factor of the morphology of active layer beyond the morphology of the underneath layer in order to controlling the morphology of the organic layer and further optimizing the device performance as well as the stability.

Acknowledgements

Though this dissertation is an individual work, I could never have reached the heights or explored the depths without the help, support, guidance and efforts of a lot of people.

First and foremost, I would like to express the deepest appreciation to my academic supervisor, Professor Katsuhiro Akimoto, who has the attitude and the wisdom of a real scientist: he continually and convincingly conveyed a spirit of adventure in regard to scientific research, and an excitement in regard to supervising. During the past three years, he has offered me constructive advices and suggestions in research work, many great opportunities to participate academic conferences to communicate with other researchers and kind-hearted encouragement in pursuing little something that really matters to me. He gave me freedom, tolerance and consideration in research work as well as in daily life. His attitude to science, enthusiasm for truth and kind nature will always inspire me. Getting this opportunity to work here in Tsukuba under my respected supervisor's supervision is one of the best things that ever happened to me.

I would like to thank committee members, Professor Hidemi Shigekawa, Professor Takashi Suemasu and Professor Shigeru Masuda for reviewing my thesis, whose suggestions and opinions demonstrated to me that concern for fully working to support a standpoint should always be emphasized.

I would also like to thank Associate Professor Takeaki Sakurai in Akimoto & Sakurai Lab for his technical support, encouragement and valuable discussions and Professor Masahiro Sasaki, my vice-supervisor, for the orientations the first day I registered and for the kind help in the following days since when.

And many thanks to all of the members from Akimoto & Sakurai Lab, especially Fujieda san, Hu san, Fu san, Luo san, Monirul san and Halim san , who helped me out when I was in trouble with experiments. The happy time we spent together is a precious gift they have ever presented to me.

In addition, a big thank you to Dr. Shenghao Wang, a senior in Akimoto & Sakurai Lab. In the past three years, he is a tutor, a friend, an elder brother and a buddy of mine. He taught me how to operate the equipments in our lab., showed me how to present the research result, offered me many constructive suggestions and encouraged me to preserve in the research work.

A special thank you to Professor Lili Wu, from Sichuan University and Dr. Xue Bai, from National University of Singapore, who provided me many treasured discussions and support.

Finally, I am most grateful to my family, my deceased mother, my father, elder brother, Ms. Zhifang Wei and Mr. Xipei Chen for all their support and love.

Publication List and Conference Contributions

1. **X. Hao,** S. Wang, T. Sakurai and K. Akimoto. Effect of bathocuproine buffer layer in small molecule organic solar cells with inverted structure. Japanese Journal of Applied Physics, **54**, 04DK06 (2015).
2. **X. Hao,** S. Wang, T. Sakurai, S. Masuda and K. Akimoto. Novel cathode buffer layer of Ag-doped bathocuproine for small molecule organic solar cell with inverted structure. Organic Electronics, **15,** 1773 (2014).
3. **X. Hao,** S. Wang, T. Sakurai, S. Masuda and K. Akimoto. Improvement of Stability for Small Molecule Organic Solar Cells by Suppressing the Trap Mediated Recombination, **submitted to ACS Applied Materials & Interfaces, under review.**
4. S. Wang, T. Sakurai, **X. Hao,** W. Fu S. Masuda and K. Akimoto. Favorable electronic structure for organic solar cells induced by strong interaction at interface. Journal of Applied Physics, **114**, 183707 (2013).

Conference contributions

1. **X. Hao**, S. Wang, T. Sakurai and K. Akimoto. Morphological influences on the open circuit voltage in small molecule bulk solar cells. The 8th International Symposium on Flexible Organic Electronics (ISFOE15), July 6th-9th, 2015, Thessaloniki, Greece. (Poster presentation)
2. **X. Hao**, S. Wang, T. Sakurai and K. Akimoto. Morphology of active layer: effect on the open circuit voltage of small molecule bulk solar cells. The 5th Asia-Africa Sustainable Energy Forum (5thAASEF), May 10th-13rd, Tsukuba, Japan. (Poster presentation)
3. **X. Hao**, S. Wang, T. Sakurai and K. Akimoto. Efficiency enhancement of organic solar cells by suppressing recombination at cathode interface. The 62nd JSAP Spring Meeting, March 11th-14th, 2015, Hiratsuka, Japan. (Poster presentation)
4. **X. Hao**, S. Wang, T. Sakurai and K. Akimoto. Performance improvement of small molecular organic solar cells with inverted structure by using an ITO cathode coated by ultrathin calcium layer. The 6th world conference on Photovoltaic Energy Conference (WCPEC-6), November 23rd-27th, 2014, Kyoto, Japan. (Poster presentation)
5. **X. Hao**, S. Wang, T. Sakurai and K. Akimoto. The Effect of bathocuproine (BCP) buffer layer in boron subphthalocyanine chloride (SubPc)/fullerene (C_{60}) organic solar cells with inverted structure. Solid State Devices and Materials (SSDM2014), September 8th-11th, 2014, Tsukuba, Japan. (oral presentation)
6. **X. Hao**, S. Wang, T. Sakurai and K. Akimoto. Improvement of stability of small molecular organic solar cells by suppression of trap assisted recombination. The 3rd Tsukuba Organic Photovoltaic Workshop, June 3rd, 2014, Tsukuba, Japan. (Poster presentation)
7. **X. Hao**, S. Wang, T. Sakurai and K. Akimoto. Ag doped bathocuproine (BCP): an effective buffer layer for SubPc based inverted structure organic solar cells. 2014 MRS Spring Meeting & Exihibit, April 21st-25th, 2014, San Francisco, USA. (Poster

presentation)

8. **<u>X. Hao</u>**, S. Wang, T. Sakurai and K. Akimoto. Device stability of inverted and conventional small organic solar cells with MoO_3 and BCP as charge transport layers. The 61st JSAP Spring Meeting, March, 17^{th}-20^{th}, 2014, Sagamihara, Japan. (Oral presentation)